OrtogOnLineMag

ISSN: 2764-9466, Vol. 7, nº 2

Cicero Moraes   Everton da Rosa   Rodrigo Dornelles

OrtogOnLineMag

Volume 7, número 1
Julho de 2026
Semestral

EXPEDIENTE

Idioma da Publicação
Português

www.ortogonline.com/doc/pt_br/OrtogOnLineMag/index/Publicacoes.html
cogitas3d@gmail.com
ortogonline@ortogonline.com

Cicero André da Costa Moraes
Sinop-MT

Contents

Chapter 1

Forensic Facial Approximation of Kennewick Man (~8,370 BP)

Cicero Moraes

3D Designer, Arc-Team Brazil, Sinop-MT, Brazil - Bachelor's degree in Marketing, Dr. h. c. FATELL/FUNCAR (Brazil) and CEGECIS (Mexico) - Member of Sigma Xi, Mensa Brazil, Poetic Genius Society, and International Society for the Study of Creativity and Innovation (ISSCI) - Invited reviewer: Elsevier, Springer Nature, PLoS, and LWW - Guinness World Records 2022: First 3D-printed tortoise shell.

Google Scholar[1], ResearchGate[2], ORCID[3], Homepage.[4]

Publication date: January 02, 2026

ISSN: **2764-9466** (Vol. 7, No. 2, 2026)

DOI: 10.6084/m9.figshare.31016587

Abstract

This study presents a digital forensic facial approximation of the individual known as Kennewick Man (~8,370 BP), using exclusively publicly available data for didactic and methodological purposes. The reconstruction was carried out from three-dimensional models of the skull and mandible, scaled according to published osteometric measurements and processed in a free and open-source software environment using the OrtogOnBlender add-on for Blender. The method integrates craniofacial anatomical projections, soft tissue depth markers derived from modern Asian samples, nasal projection estimates, and anatomical deformation of a virtual donor based on computed tomography data. Three sets of results were produced: a statistically grounded basic facial structure, a grayscale forensic approximation following classical forensic standards, and a colored artistic version, the latter explicitly identified as speculative. Additionally, endocranial volume was estimated from the digital endocast, yielding values consistent with modern male variation. The study demonstrates the feasibility of producing reproducible, transparent, and educational forensic facial approximations even in the absence of direct access to physical human remains.

Keywords: Forensic facial approximation, Kennewick Man, 3D facial reconstruction, Digital forensic anthropology, Open-source software.

[1] https://scholar.google.com.br/citations?user=u33uvHUAAAAJ
[2] https://www.researchgate.net/profile/Cicero-Moraes
[3] https://orcid.org/0000-0002-9479-0028
[4] http://www.ciceromoraes.com.br

Warning: This work is independent and has no affiliation with the institution that studied the remains of Kennewick Man. The motivating factor of this chapter is the creation of educational material for teaching facial approximation techniques, by testing the possibility of reconstructing a face using data originally available online, ranging from 3D scans to academic articles.

1.1 Introduction

A nearly complete skeleton, composed of 350 fragments representing 143 elements [Chatters_2017_a], was discovered on the banks of the Columbia River[5] in Kennewick, Washington state (USA), in July 1996 [Chatters_2000_a], by two university students who were walking in the area. They called the police, who, given the characteristics of the find, contacted the local archaeologist, Dr. James Chatters [Preston_2014_a].

They did not know it, but they were facing what the Smithsonian considered the most important human skeleton ever found in North America (Preston, 2014).

Over many years of studies and legal twists and turns—which even involved the FBI—it became possible to determine various characteristics of the bones. It was a male individual, aged between 35 and 45 years, with a height of 173.1 cm (± 3.4 cm), an estimated weight of 70

[5] https://maps.app.goo.gl/qGVRyv25jPskhQCm9

to 75 kg, and moderate robusticity [Chatters_2000_a]. He was right-handed and died around 8,368 ± 21 BP [Chatters_2017_a].

In the initial analyses, Chatters observed that, although the bone structure indicated an Asian or Pacific coast origin, it differed from modern United States Indigenous peoples, presenting features compatible with Polynesian populations, particularly Eastern Pacific islanders and Jōmon/Ainu peoples [Chatters_2000_a]. These observations were complemented by a 2015 mitochondrial DNA study, which confirmed the Asian origin and indicated statistical proximity to the Colville people and individual proximity to the Anzick-1 sample [Rasmussen_et_al_2015_a].

Regarding diet, isotopic analyses of the bones revealed that the diet of the Kennewick Man, as he became known, was predominantly based on marine-derived proteins [Chatters_2000_a], in addition to consumption of potable water from glacial sources [Chatters_2017_a]. He presented minor anomalies in the feet, mild osteoarthritis in the knee and right shoulder joints, as well as evidence of injuries sustained throughout life, such as a small cranial depression, rib fractures, a fracture in the right scapula, and most notably, a spear projectile wound with part of the point still lodged in the right ilium. According to the research, there is consensus that the fractures in the ribs and ilium occurred in early adulthood, while the injuries to the skull and shoulder were close to the time of death (Chatters, 2017). Severe exostosis was also observed in the bones of the external auditory canal, with both nearly obstructed [Chatters_2000_a], a condition compatible with the known "surfer's ear," typically caused by frequent immersion in cold water [Preston_2014_a].

Since its discovery, the Kennewick remains became involved in intense legal disputes, particularly related to the Native American Graves Protection and Repatriation Act (NAGPRA), which sought the repatriation of the mortal remains. The case mobilized 93 lawyers and included an FBI investigation involving Drs. James Chatters and Floyd Johnson, in the initial context of forensic osteology. In 2002, the court ruled that the bones did not belong to any modern tribe, rendering NAGPRA inapplicable. An appeal attempt was rejected in 2004, consolidating the scientists' victory. Following the final verdict, an extensive analysis project was carried out, including detailed documentation, external and internal 3D scanning via computed tomography, 3D printing of the pieces (including the projectile in the ilium), and a forensic facial reconstruction. Initially modeled in clay by a technical team, the face was later refined by StudioEIS, which aged the features, modeled hair and beard, and applied pigmentation for museum exhibition. The chosen appearance was compatible with the Jōmon people, who emerged in Japan approximately 12,000 years ago, based on photographic documentation and possible links to the Ainu—consistent with the craniometric analyses [Preston_2014_a].

Important: An initial facial approximation had been created for the documentary "Mystery of the First Americans," carried out by Thomas McClelland under the guidance of Dr. James Chatters. This version featured a monochromatic head with a significantly pronounced nose and was presented as early as 2000 [Chatters_2000b_a]. In contrast, the second approximation, mentioned earlier, displayed a less pronounced nose and was presented in 2014 [Preston_2014_a].

However, the 2015 genetic study changed the scenario: by confirming affinity with modern Native American populations, it prompted political action that reclassified the remains as Native American, resulting in the application of NAGPRA and the repatriation of the skeleton. The reburial took place on February 18, 2017, at an undisclosed location [Mabbutt_2017_a].

1.2 Materials and Methods

The work presented in this manuscript was conducted using open-source software. The primary tool employed is OrtogOnBlender (https://www.ciceromoraes.com.br/doc/pt_br/OrtogOnBlender/index.html), an add-on for Blender[6] that enables this software to acquire capabilities absent in the original program, such as reconstructing computed tomography scans, performing photogrammetry, utilizing forensic facial reconstruction tools, and others, including enhancing facial details through artificial intelligence. Although this work was executed on Linux Ubuntu 24.04, since all the software is open-source and multi-platform, it can also be performed on Windows and macOS.

Note: Additionally, this document was created using only open-source software. The images were edited in GIMP[7], the graphics were produced in Inkscape[8], and the text was written in reStructuredText for Sphinx, with adaptations to the source files (LaTeX and HTML/JavaScript) to enable compilation into both online and printable versions. Thus, the entire project was developed using open-source solutions.

Initially, two models were downloaded: the skull[9] and the mandible[10], both provided by the user **nicamarvin2005** on *Sketchfab*. These models are released under the Creative Commons Attribution license. The scale was adjusted using the measurements reported in [Chatters_2000b_a]. The imported model was then aligned in the Frankfurt horizontal plane and subjected to structural projections in OrtogOnBlender, based on

[6] https://www.blender.org/
[7] https://www.gimp.org
[8] https://inkscape.org/
[9] https://skfb.ly/pDUrz
[10] https://skfb.ly/pDXT9

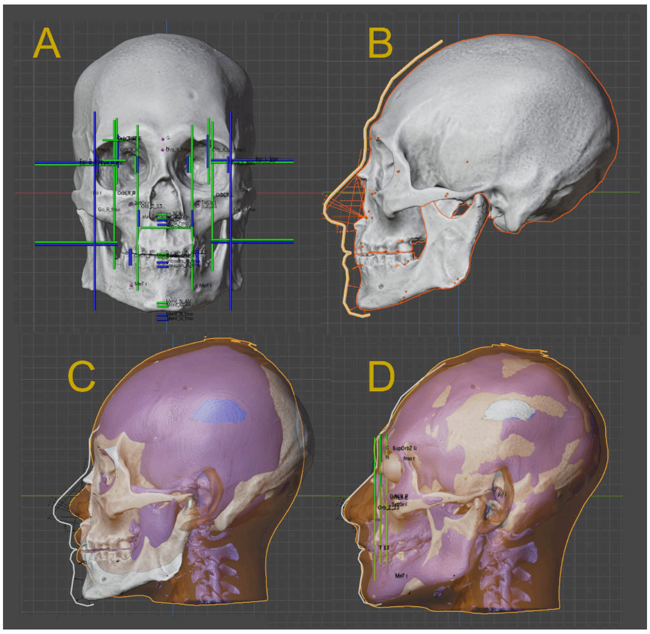

Figure1.1: A) Skull alignet in the Frankfurt plane with projection lines. B) Profile view with soft tissue markers and nose projection. C and D) Facial deformation using a virtual donor.

data derived from CT scans of living individuals available in [Moraes_and_Suharschi_2022_a]. The teeth of Kennewick Man (hereafter referred to as KM) exhibit considerable wear, resulting in a more closed bite without overbite. This condition causes the facial height to appear slightly reduced along the Z-axis, which is observable in the menton projection: the green lines represent population averages, while the blue lines indicate proportions scaled from the frontomalare orbitale (fmo–fmo) distance. Although the incisor projections align closely with the green (average) lines, suggesting apparent concordance, the correct proportional position corresponds to the lower blue lines. This discrepancy arises because the average fmo–fmo distance is approximately 97 mm, whereas in KM it measures 103 mm—roughly one standard deviation above the mean (https://bit.ly/3NRw2KW). Consequently, the lower limit of the menton falls between the green (average) and blue (proportional) lines. Dental wear of this nature typically produces a modest reduction in facial height along the Z-axis and confers a somewhat prognathic facial appearance (Fig. 1.1, A).

The line projections indicate the expected positions of key anatomical structures, such as the ocular globes, ears, and mouth, among others. However, to achieve a more accurate facial approximation, additional data are required, including nose projection (derived from the templates in [Moraes_and_Suharschi_2022_a]) and soft-tissue depth markers obtained from a sample of modern Asian individuals [Chan_et_al_2011_a]. By integrating these two datasets, it becomes possible to delineate the facial profile (Fig. 1.1, B).

It is worth noting that, in the projection model employed here, the Asian reference sample yields a somewhat shorter nasal projection along the Y-axis compared to European samples (see Base AV: https://bit.ly/3NRw2KW). Although these data suffice for a reasonable facial approximation, a further step is undertaken to enhance anatomical detail. This process, known as *anatomical deformation* [Quatrehomme_et_al_1997_a], involves deforming a virtual donor head—reconstructed from a CT scan of a living individual—until the donor's skull aligns precisely with that of KM. The resulting deformation is propagated to the soft tissues, producing a final facial approximation that remains consistent with the established projections and profile view (Fig. 1.1, D and E).

Hint: Didactic materials, in the form of recorded tutorials for OrtogOnBlender, are available as follows: two covering line projections (class 1[11], class 2[12]), one dedicated to nose projection (here[13]), and one focused on anatomical deformation (here[14]).

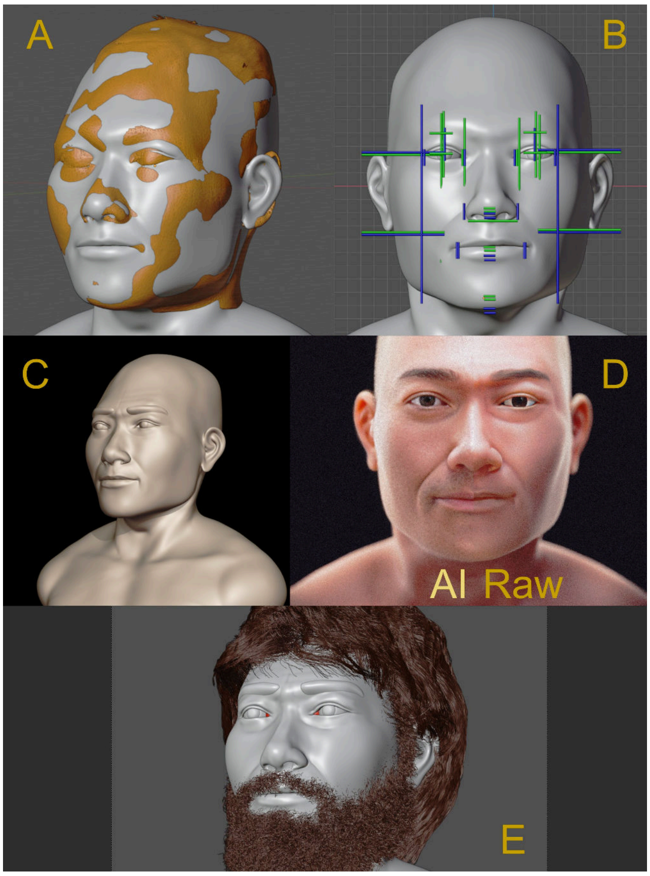

Figure1.2: A) Basic facial structure compatible with the anatomical deformation. B) Frontal view of the basic facial structure with projection lines. C) Basic Bust. D) Facial details enhanced using artificial intelligence.

By integrating data from skull projections, soft-tissue depth markers, and anatomical deformation, a basic facial approximation is generated through interpolation of these sources (Fig. 1.2, A). The frontal view facilitates verification of compatibility with the projection lines,

[11] https://youtu.be/U6oYkEmfyWo
[12] https://youtu.be/Vcz2e5uSFX8
[13] https://youtu.be/F205kLQ--Oo
[14] https://youtu.be/xig5_EcIFWA

confirming that the positions of the ocular globes, the limits of the eyes and mouth, and the contours of the nose and ears align appropriately (Fig. 1.2, A).

An additional noteworthy observation concerns cranial breadth: in most individuals, the bigonial breadth (go–go) is approximately equal to the frontomalare orbitale distance (fmo–fmo). However, in KM, the fmo–fmo measures approximately 103 mm, while the go–go reaches ~120 mm—representing 3.8 standard deviations above the mean. This pronounced bizygomatic and bigonial breadth contributes to the characteristically square facial appearance, which is further accentuated by the reduced facial height along the Z-axis.

The basic facial structure subsequently undergoes refinement through digital sculpting and carving, representing the most objective phase of the approximation process (Fig. 1.2, C). The final stage involves texturing, coloring, lighting, and fine detailing enhanced by artificial intelligence (Fig. 1.2, D), employing the Codeformer library [Zhou_et_al_2022_a] running inside OrtogOnBlender. For the artistic implementation, elements of a more conjectural nature, notably fur and hair, were modeled with the intention of producing a distribution characterized by greater naturalness and increased randomness (Fig. 1.2, E).

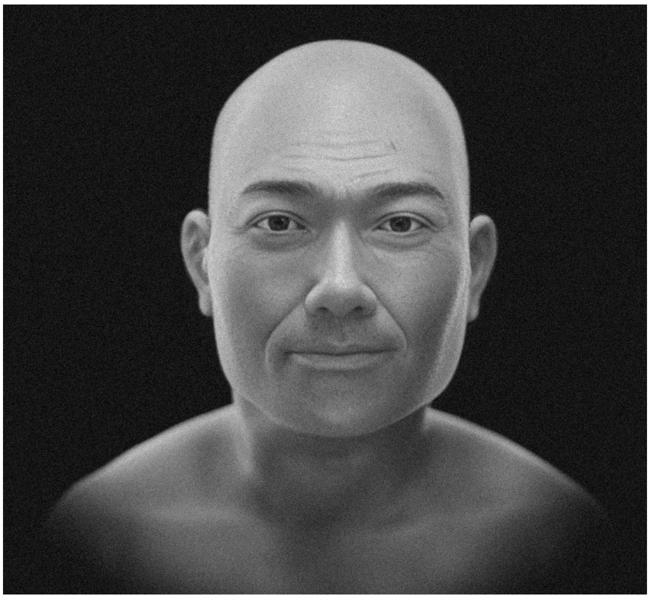

Figure1.4: Simple facial approximation - front

1.3 Results and Discussion

Three distinct groups of images were produced. The first group depicts the most objective and statistically grounded approximation: a basic facial structure in grayscale (Fig. 1.3). The second group presents rendered faces in grayscale without hair, aligning with conventional forensic imaging standards (Fig. 1.4, Fig. 1.5). Finally, the third group features fully colored renderings that incorporate artistic and speculative elements—such as hair and skin tone—informed by the facial approximation published in 2014 (Fig. 1.6, Fig. 1.7).

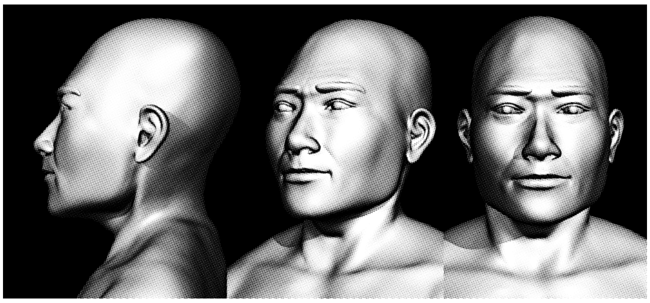

Figure1.3: Basic facial approximation

During the anatomical deformation process, the endocast was segmented, yielding an approximate volume of 1450 cm³. When converted to brain volume [Moraes_et_al_2023_a], this corresponds to approximately 1308 cm³—slightly above the modern male average of 1234 cm³ [Ritchie_2018_a]. These measurements should be interpreted with caution. Although they are broadly consistent with the original cranial

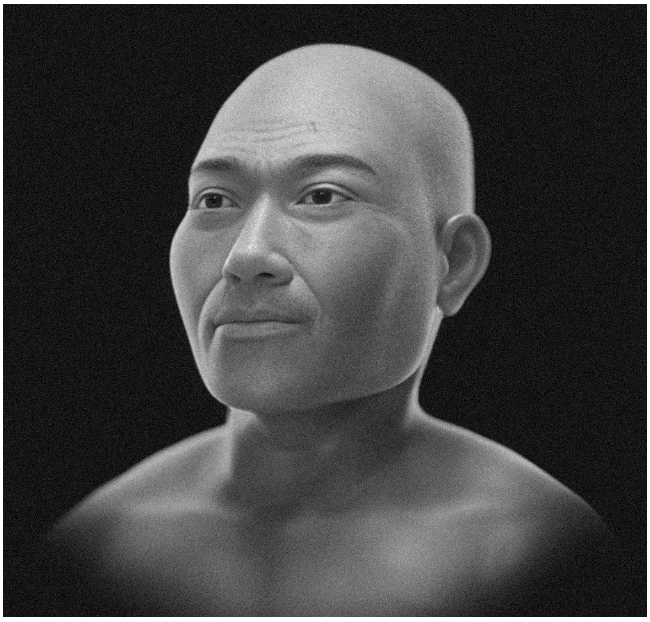

Figure1.5: Simple facial approximation - portrait

structure, minor discrepancies may arise between the original publication data and the digitized model, as the mesh reconstruction process can introduce subtle deformations or artifacts.

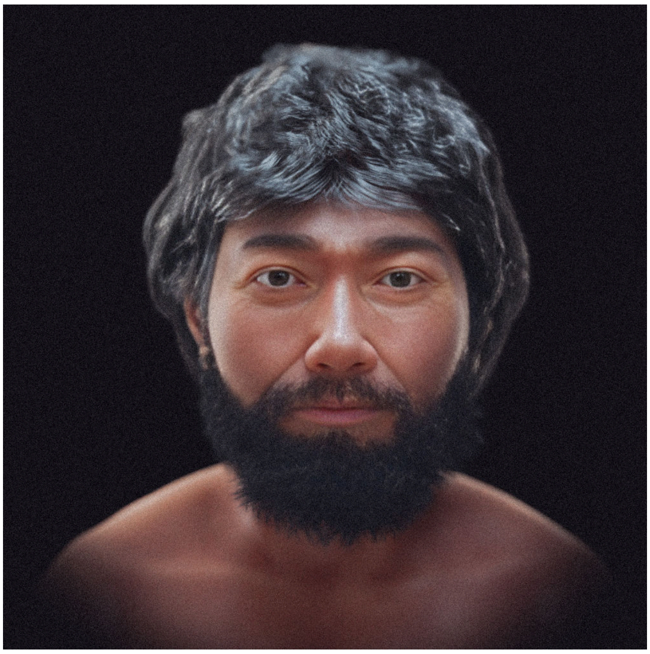
Figure1.6: Artistic facial approximation - front

1.4 Conclusion

The facial approximation presented here demonstrates that it is possible to produce technically grounded, reproducible, and transparent forensic reconstructions using open-access data, by integrating anatomical projections, soft tissue markers, and virtual anatomical deformation. By clearly distinguishing between objective results and artistic elements, the study reinforces the scientific and educational value of the methodology without exceeding its inferential limits. This work contributes a didactic model for teaching and research in digital forensic anthropology.

1.5 Acknowledgements

To Dr. Dong Quang for providing the tomography of the virtual donor. To nicamarvin2005[15] (Sketchup user), for share this model and allow this work be done.


Figure1.7: Artistic facial approximation - portrait

1.6 References

[Chan_et_al_2011_a] Chan, W. N. J., Listi, G. A., & Manhein, M. H. (2011). In VivoFacial Tissue Depth Study of Chinese□American Adults in New York City*. Journal of Forensic Sciences, 56(2), 350–358. https://doi.org/10.1111/j.1556-4029.2010.01640.x

[Chatters_2000_a] Chatters, J. C. (2000). The Recovery and First Analysis of an Early Holocene Human Skeleton from Kennewick, Washington. American Antiquity, 65(2), 291–316. https://doi.org/10.2307/2694060

[Chatters_2000b_a] Chatters, J. (2000). Meet Kennewick Man. NOVA - PBS. https://www.pbs.org/wgbh/nova/article/meet-kennewick-man/

[Chatters_2017_a] Chatters, J. C. (2017). Making archaeological sense of Kennewick Man. Quaternary International, 444, 83–97. https://doi.org/10.1016/j.quaint.2017.01.045

[Mabbutt_2017_a] Mabbutt, L. (2017). Tribes bury remains of ancient ancestor, also called Kennewick Man. The Seattle Times. https://www.seattletimes.com/seattle-news/tribes-bury-r

[15] https://sketchfab.com/nicamarvin2005

emains-of-ancient-ancestor-also-called-kennewick-man/

[Moraes_and_Suharschi_2022_a] Moraes, C., & Suharschi, I. (2022). Mensuração de Dados Faciais Ortográficos em Moldavos e Comparação com Outras Populações. figshare. https://doi.org/10.6084/M9.FIGSHARE.20089754

[Moraes_et_al_2023_a] Moraes, C., Habicht, M. E., Galassi, F. M., Varotto, E., & Beaini, T. (2023). Pharaoh Tutankhamun: a novel 3D digital facial approximation. Italian Journal of Anatomy and Embryology, 127(1), 13–22. https://doi.org/10.36253/ijae-14514

[Preston_2014_a] Preston, D. (2014). Kennewick Man finally freed to share his secrets. Smithsonian Magazine. https://www.smithsonianmag.com/history/kennewick-man-finally-freed-share-his-secrets-180952462/

[Quatrehomme_et_al_1997_a] Quatrehomme G, Cotin S, Subsol G, Delingette H, Garidel Y, Grévin G, Fidrich M, Bailet P, Ollier A. A fully three-dimensional method for facial reconstruction based on deformable models. J Forensic Sci. 1997 Jul;42(4):649-52. PMID: 9243826.

[Rasmussen_et_al_2015_a] Rasmussen, M., Sikora, M., Albrechtsen, A., Korneliussen, T. S., Moreno-Mayar, J. V., Poznik, G. D., Zollikofer, C. P. E., Ponce de León, M. S., Allentoft, M. E., Moltke, I., Jónsson, H., Valdiosera, C., Malhi, R. S., Orlando, L., Bustamante, C. D., Stafford, T. W., Jr, Meltzer, D. J., Nielsen, R., & Willerslev, E. (2015). The ancestry and affiliations of Kennewick Man. Nature, 523(7561), 455–458. https://doi.org/10.1038/nature14625

[Ritchie_2018_a] Ritchie, S. J., Cox, S. R., Shen, X., Lombardo, M. V., Reus, L. M., Alloza, C., Harris, M. A., Alderson, H. L., Hunter, S., Neilson, E., Liewald, D. C. M., Auyeung, B., Whalley, H. C., Lawrie, S. M., Gale, C. R., Bastin, M. E., McIntosh, A. M., & Deary, I. J. (2018). Sex Differences in the Adult Human Brain: Evidence from 5216 UK Biobank Participants. In Cerebral Cortex (Vol. 28, Issue 8, pp. 2959–2975). Oxford University Press (OUP). https://doi.org/10.1093/cercor/bhy109

[Zhou_et_al_2022_a] Zhou, S., Chan, K. C. K., Li, C., & Loy, C. C. (2022). Towards Robust Blind Face Restoration with Codebook Lookup Transformer (Version 2). arXiv. https://doi.org/10.48550/ARXIV.2206.11253

Chapter 2

Rest in Face: The Forensic Approximation of Individual 157 from the Račeša Necropolis (13th–14th Century)

Cicero Moraes
3D Designer, Arc-Team Brazil, Sinop-MT, Brazil - Bachelor's degree in Marketing, Dr. h. c. FATELL/FUNCAR (Brazil) and CEGECIS (Mexico)
Google Scholar[16], ResearchGate[17], ORCID[18], Homepage.[19]

Nataša Šarkić
Aita Bioarchaeology, Malgrat de Mar, ES-08380 Barcelona, Spain - PhD in Physical Anthropology, Founder CEO of Aita Bioarchaeology
ORCID[20], ResearchGate[21], Google Scholar[22]

Roberto Cighetti
Aita Bioarchaeology, Malgrat de Mar, ES-08380 Barcelona, Spain - Osteoarc, IT-21040 Gornate Olona VA, Italy
ORCID[23], ResearchGate[24], Google Scholar[25]

Sofie-Kristin Schendzielorz
University of Dundee, Nathergate, UK-DD1 4HN Dundee, UK
ORCID[26]

Marija Mihaljević
Municipal Museum Nova Gradiška, Trg kralja Tomislava 7, HR-35400 Nova Gradiška, Croatia

Publication date: February 9, 2026
ISSN: **2764-9466** (Vol. 7, No. 2, 2026)
DOI: 10.6084/m9.figshare.31301575

Abstract

The Račeša necropolis in Croatia is a complex archaeological site dated from the 13th to 16th centuries, initially associated with the Templars and later with the Order of the Knights Hospitaller of Saint John of Jerusalem. Excavations between 2012 and 2023 revealed an extensive architectural structure and 181 inhumations, most following the traditional Christian rite. However, grave 157 stood out for its atypical nature: a middle-aged man (40-50 years), stature of 164 cm, with evidence of occupational stress and intense physical violence, including old lesions on the maxilla and ribs, and perimortem traumas on the cranium caused by a sharp object. The burial deviated from the standard, with the thorax in a prone position (face down) and the cranium removed and repositioned 30 cm from the neck, suggesting postmortem manipulation motivated by beliefs in revenants (vampires) according to Slavic traditions. Given this singular profile, this study applied forensic facial approximation to the fragmented cranium, reconstructed via computed tomography and open-source digital tools such as OrtogOnBlender. The cranium, segmented into 21 parts, underwent anatomical repositioning, with soft tissue projections based on European population averages, soft tissue thickness markers, and anatomical deformation using a virtual donor. Three images were generated: two objective ones in grayscale without facial hair and one artistic with speculative coloration. Additionally, the brain volume of 1488 cm³ indicated mild megalencephaly (+2.59 standard deviations relative to the modern male average).

Keywords: Forensic facial approximation, free software, open source, anthropology, vampire.

[16] https://scholar.google.com.br/citations?user=u33uvHUAAAAJ
[17] https://www.researchgate.net/profile/Cicero-Moraes
[18] https://orcid.org/0000-0002-9479-0028
[19] http://www.ciceromoraes.com.br
[20] https://orcid.org/0000-0003-3286-5538
[21] https://www.researchgate.net/profile/Natasa-Sarkic
[22] https://scholar.google.com/citations?user=EmnWf2QAAAAJ&hl=es
[23] https://orcid.org/0000-0001-6116-1316
[24] https://www.researchgate.net/profile/Roberto-Cighetti
[25] https://scholar.google.com/citations?user=fS5npXoAAAAJ&hl=en
[26] https://orcid.org/0009-0007-2033-631X

Attention: Should you encounter any errors in the text, kindly report them to the author; he may be contacted through the academic social media platforms mentioned at the beginning of the chapter.

2.1 Introduction

The necropolis of Račeša, Croatia, is a complex archaeological site whose excavations have revealed a remarkable occupational sequence. Initially associated with a Templar property, and subsequently under the dominion of the Order of the Knights Hospitaller of Saint John of Jerusalem, the site has an established chronology between the 13th and 16th centuries. The research, which took place between 2012 and 2023, brought to light an extensive architectural complex and 181 inhumations, the majority following the traditional Christian rite, positioned in a west-east direction [Sarkic_et_al_2024_b].

However, one finding in particular deviated drastically from the standard: grave number 157. This grave was discovered in a layer beneath the church floor, positioned in a less favored spot next to the southern wall of the nave. Osteological analysis of the skeleton revealed it to be a middle-aged man, with an estimated age between 40 and 50 years. His stature was calculated at 164.03 cm. The individual's biological profile is marked by prominent markers of occupational stress and a history of intense physical violence.

The evidence of trauma is multiple and dates from different moments in his life, including an old sharp-force injury on the maxillary bone and rib fractures that were still in the process of healing at the time of death. The fatal injury, however, resulted from acute interpersonal violence, attested by two perimortem traumatic lesions on the back of the skull, caused by a sharp object, with no signs of healing. In addition to the violent death, the old injuries suggest that this man may have lived with a partially disfigured face.

The positioning of the body in the tomb is the most intriguing characteristic. Grave 157 presented an atypical burial, notably by the inversion of the thorax to a prone position (face-down) and the removal and repositioning of the skull approximately 30 cm from the neck. The absence of cut marks suggests that this postmortem manipulation occurred early on, while the soft tissues were already putrefying, but before the complete degradation of the ligaments. Such deviant burial practices, associated with individuals with violent deaths or a history of conflict, suggest an intervention motivated by beliefs in revenants (vampires), according to Slavic tradition.

Given the singular profile of the individual from grave 157—a man marked by violence in life and manipulated in death—it becomes imperative to reestablish his visual identity. The objective of this work is, therefore, to determine the probable facial appearance of this individual, providing a new perspective for the understanding of his potential social exclusion and the community's reaction to his death. To this end, the team reconvened to apply the forensic facial approximation technique to the skull, transforming the skeletal data into a face that transcends the archaeological record.

2.2 Materials and Methods

The skull from tomb 157 was found fragmented [Sarkic_et_al_2024_b] and subsequently manually reconstructed by specialists, undergoing a computed tomography scan that digitized it in 3D. A video in RGB color format (8 bits) served as the basis for the three-dimensional recovery of the structure. Initially, the file in Audio Video Interleave (AVI) format, compressed via the Microsoft Video 1 codec and with dimensions of 1040 x 1532, was converted into a sequence of grayscale images and, subsequently, into a DICOM sequence (voxel dimensions: 0.23364, 0.23364, 0.6), using specific tools for this purpose [Moraes_et_al_2021_b] from the OrtogOnBlender add-on (http://www.ciceromoraes.com.br/doc/pt_br/OrtogOnBlender/index.html).

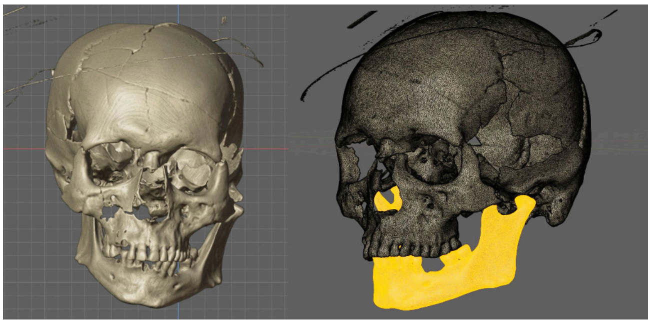

Figure2.1: On the left, the DICOM file reconstructed in 3D. On the right, the mesh being edited for mandible segmentation.

Once converted to DICOM, it was possible to reconstruct the 3D mesh using a segmentation threshold (Hounsfield-equivalent factor) of 53 [Moraes_et_al_2021b_b], due to the RGB origin of the material (Fig. 2.1, left). The resulting 3D mesh enabled the segmentation of the anatomical pieces for the subsequent adjustments that were performed thereafter (Fig. 2.1, right).

The skull was segmented into 21 parts (Fig. 2.2, left) and repositioned according to criteria of structural and anatomical coherence (Fig. 2.2, right). A comparative animation showing two states — the original fragmented condition and the reorganized one — facilitated the dynamic observation of the fragment positioning. This analysis, combined with the operator's experience

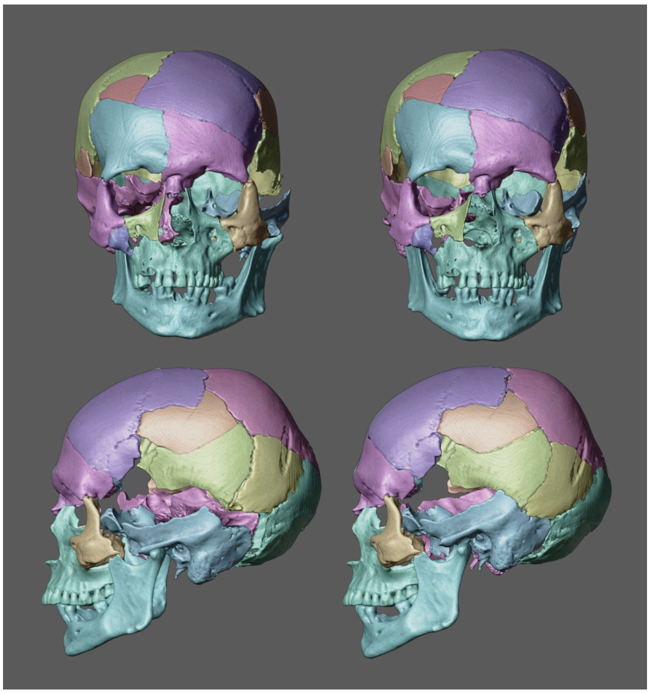

Figure2.2: The left side (top and bottom) presents the original 3D reconstructed mesh segmented. The right side (top and bottom) shows the reassembled segments with anatomical coherence.

and structural comparison with a reference skull (virtual donor), enabled the definitive fixation of the cranial configuration that served as the basis for the subsequent facial approximation.

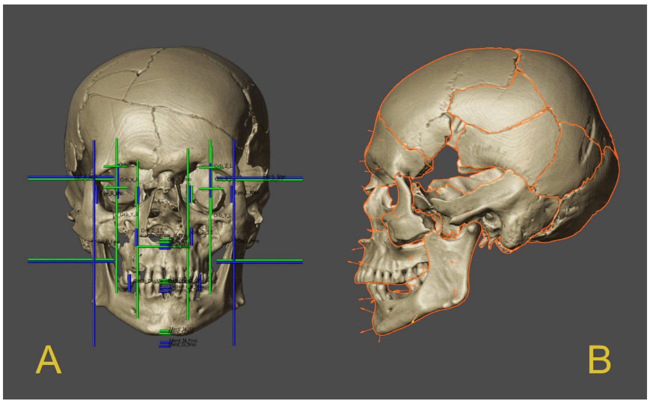

Figure2.3: A) Projections based on average anatomy. B) Soft-tissue depth markers.

Once the definitive cranial configuration was established, anatomical landmarks were placed to allow anthropometrically-based projections to indicate the expected averages and proportions for both the existing structures and those to be reconstructed (video tutorials available here: class 1[27], class 2[28]). The resulting guidelines delineate the anticipated anatomical spaces, indicating, for example, the position of the eyeballs, the limits of the nasal wings and nasal base, the horizontal boundaries of the lips, and others. Additionally, these projections also reveal the expected dimensions for present bony structures, such as the mandibular contours [Moraes_and_Suharschi_2022_b].

In the present case, the mandible slightly exceeded the average value along the X-axis at the gonion region, remained within the expected average for height, and displayed a proportional dimension (in blue) below the reference mean (in green). This configuration is explained by the frontomalare orbitale measurement of 101.5 mm, which is above the general average of 96.6 mm (https://bit.ly/3NRw2KW), indicating that the skull is slightly larger than average in the transverse axis (X) while preserving the expected dimensions in the vertical axis (Y) (Fig. 2.3, A).

For the projection of facial boundaries, soft-tissue depth markers derived from population averages of living European males aged 40–49 years [De_Greef_et_al_2006_b] were distributed across the cranial surface. These data are consistent with the forensic anthropological findings reported by [Sarkic_et_al_2024_b] (Fig. 2.3, B).

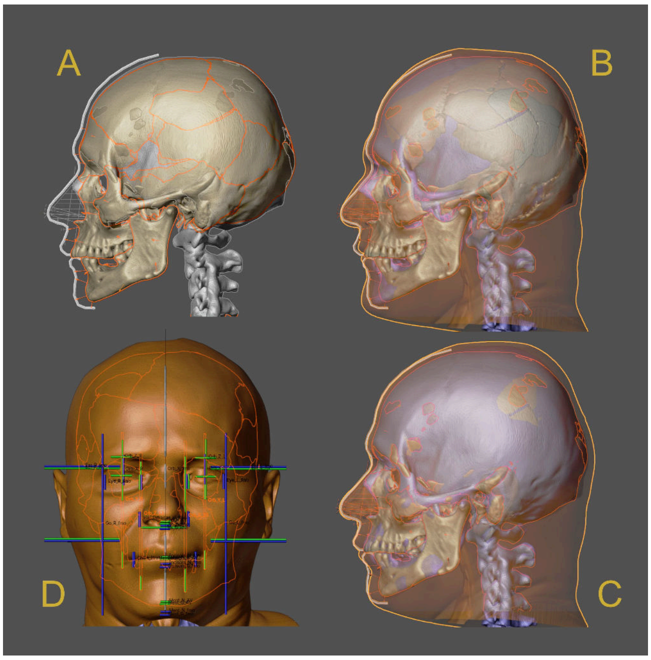

Figure2.4: A) Soft-tissue depth markers, nasal projection, and facial profile tracing. B) Original composite head of the virtual donor. C) Composite head adjusted to the skull of individual 157 – Anatomical deformation. D) Frontal view of the anatomical deformation with limit lines, demonstrating structural coherence between the two sources.

Although reassembled and anatomically coherent, the skull of individual 157 exhibited some structural absences that were filled using the skull of a virtual donor, which then enabled nasal projection according to data obtained from computed tomography scans of living individuals [Moraes_and_Suharschi_2022_b]. The soft-tissue depth markers, together with the nasal projection data, allowed the tracing of the facial profile (Fig. 2.4, A).

To further supplement the facial projection data, the anatomical deformation approach was employed [Quatrehomme_et_al_1997_b], which involves im-

[27] https://youtu.be/U6oYkEmfyWo
[28] https://youtu.be/Vcz2e5uSFX8

porting a complete head from a virtual donor—composed of meshes of soft tissue, cranium, and endocranium—and adapting it until the donor's skull matches that of individual 157, thereby reflecting the corresponding adjustment in the soft tissue and, consequently, in the face (Fig. 2.4, B and C).

Laterally, the results of the anatomical deformation proved compatible with the previously established profile projection (Fig. 2.4, C), and this coherence also extended to the frontal view of the face in relation to the limit lines based on soft-tissue measurements, correctly corresponding to the mid-orbital points, the nasal limits, the lip boundaries, and the ear positions (Fig. 2.4, D).

Tip: For replication purposes, classes on nasal projection (https://youtu.be/F205kLQ–Oo[29]) and anatomical deformation (https://youtu.be/xig5_EcIFWA).

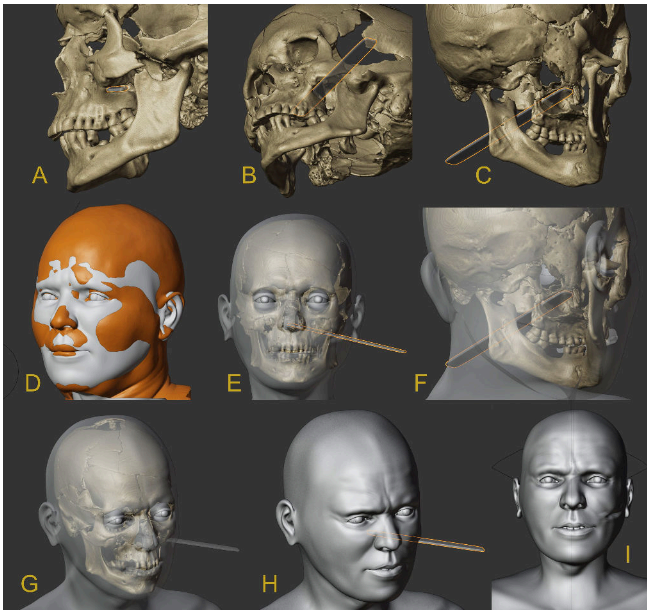

Figure2.5: A, B, C) Structure of the penetrating-cutting trajectory. D) Anatomical deformation/projections with the final basic face (in gray). E, F, G) Visualization of the transparent face with the volumetric trajectory of the lesion. H, I) Face with digital sculpture details and scar in the lesion region.

A structure was positioned in the lesion caused by, probably, a penetrating-cutting object that affected the zygomatic process from the external aspect, penetrating through it and exiting slightly above the palatine process of the maxilla (Fig. 2.5, A, B, C). Following the creation of the final basic face (Fig. 2.5, D), it was possible to identify the location of the lesion in the soft tissue (Fig. 2.5, E, F, G) and, from there, finalize the details of the facial sculpture with the resulting scar (Fig. 2.5, H, I).

Subsequently, details related to more speculative elements were configured, such as facial hair and attire

[29] https://youtu.be/F205kLQ--Oo

Figure2.6: On the right) Solid composition of the face with facial hair and attire. On the left) Comparison between the original version (Raw) and adjustments controlled by artificial intelligence (AI).

(Fig. 2.6, on the left). To finalize, the scene was illuminated, colors adjusted, opting for eyes with gray-bluish coloration and reddish-brown hair. Finally, small details were adjusted using artificial intelligence through the Codeformer library [Zhou_et_al_2022_b], directly via OrtogOnBlender XP, in an assisted manner and using a weight of 0.99, that is, very close to the original image (1.00), which can be perceived by the small variation between the original (Raw) and the adjusted version (AI) (Fig. 2.6, on the right).

2.3 Results and Discussion

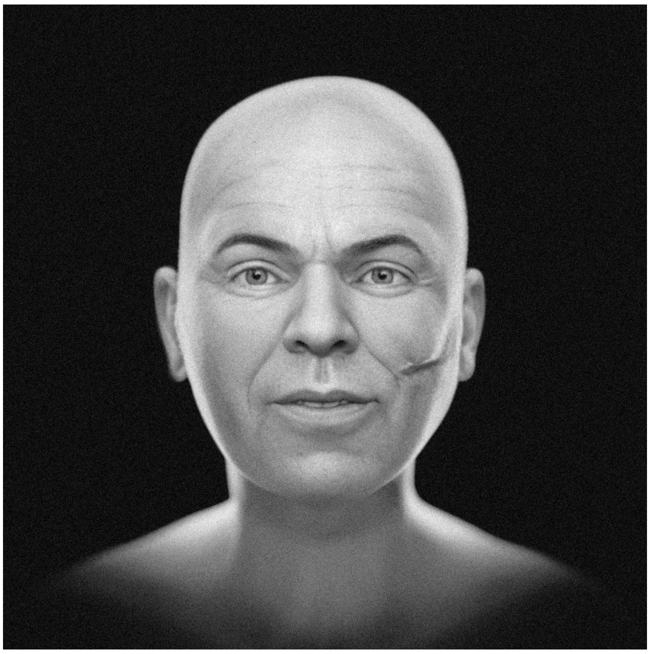

Figure2.7: Grayscale face without hair and beard - frontal.

Three images were generated at the end of the process, two related to a more objective version, in grayscale and without facial hair (Fig. 2.7, Fig. 2.8) and one with more artistic and therefore speculative elements, with coloration of the skin, eyes, and hair (Fig. 2.9).

It should be noted that forensic facial approximation contains some limitations related to the precision of fine details, such as expression marks, eye shape, etc. However, regarding the position of the eyes, lip dimensions, and nose shape, in general terms, the structures

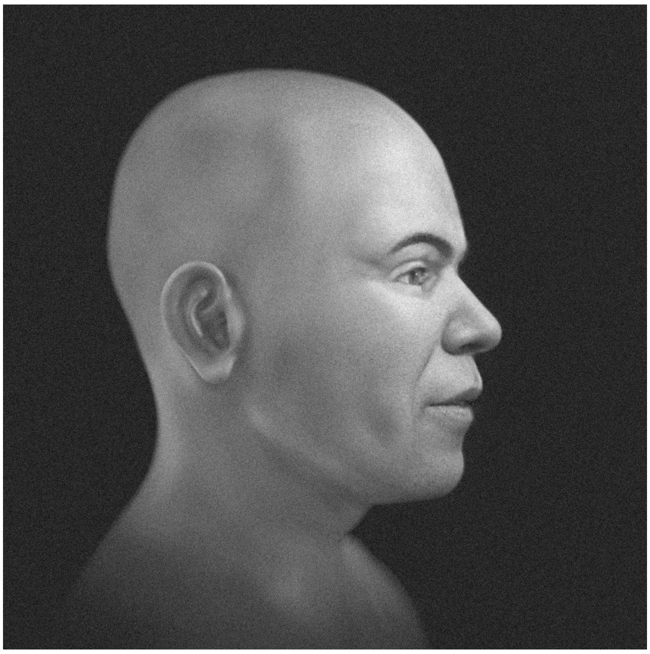

Figure2.8: Grayscale face without hair and beard - profile.

are significantly compatible with the individual in life, to the point of providing data for the recognition of crime victims and subsequent identification, as illustrated in a forensic case involving one of the authors (C.M.) [Baldasso_et_al_2020_b].

Figure2.9: Colored version with more subjective/artistic elements.

In addition to the facial approximation, the endocranium of Individual 157 was also segmented, resulting in ~1650 cm^3. When converted to brain volume (-9.81%) [Moraes_et_al_2023_b], it resulted in 1488 cm^3, which compared to the modern male average of 1234 cm^3 (± 98) [Ritchie_et_al_2018_b] is at +2.59 standard deviations, indicating mild megalencephaly. This finding is reported as a morphological observation and should not be interpreted as indicative of cognitive or behavioral traits.

2.4 Conclusion

This study demonstrates the effectiveness of forensic facial approximation in reconstructing the visual identity of archaeological individuals, such as Individual 157 from the Račeša necropolis, marked by violence in life and postmortem manipulation. The integration of digital techniques, such as 3D segmentation and anatomical deformation, allowed for the generation of facial representations compatible with anthropological data, highlighting lesions and scars that suggest a conflictual existence and possible social stigmatization. Despite the inherent limitations in the precision of speculative details, the results provide valuable insights into deviant funerary practices linked to beliefs in revenants, enriching the historical and cultural understanding of the Croatian medieval period.

2.5 Acknowledgements

To Dr. Richard Gravalos for providing the tomography of the virtual donor. To Michael Havis for proposing the idea of the project and putting the authors in contact.

2.6 References

[Baldasso_et_al_2020_b] Baldasso, R. P., Moraes, C., Gallardo, E., Stumvoll, M. B., Crespo, K. C., Strapasson, R. A. P., & de Oliveira, R. N. (2020). 3D forensic facial approximation: Implementation protocol in a forensic activity. In Journal of Forensic Sciences (Vol. 66, Issue 1, pp. 383–388). Wiley. https://doi.org/10.1111/1556-4029.14587

[De_Greef_et_al_2006_b] De Greef, S., Claes, P., Vandermeulen, D., Mollemans, W., Suetens, P., & Willems, G. (2006). Large-scale in-vivo Caucasian facial soft tissue thickness database for craniofacial reconstruction. In Forensic Science International (Vol. 159, pp. S126–S146). Elsevier BV. https://doi.org/10.1016/j.forsciint.2006.02.034

[Quatrehomme_et_al_1997_b] Quatrehomme G, Cotin S, Subsol G, Delingette H, Garidel Y, Grévin G, Fidrich M, Bailet P, Ollier A. A fully three-dimensional method for facial reconstruction based on deformable models. J Forensic Sci. 1997 Jul;42(4):649-52. PMID: 9243826.

[Moraes_et_al_2021_b] Moraes, C., Dallazen, E., Dornelles, R., & Da Rosa, E. (2021). Conversão de Imagens em Arquivos DICOM com o OrtogOnBlender. figshare. https://doi.org/10.6084/M9.FIGSHARE.14445366.

https://ortogonline.com/doc/pt_br/OrtogOnLineMag/3/ImagemDICOM.html

[Moraes_et_al_2021b_b] Moraes, C., Dornelles, R., & Rosa, E. D. (2021). Sistema de Reconstrução de Tomografia Computadorizada Baseado no Slicer 3D e no DicomToMesh. figshare. https://doi.org/10.6084/M9.FIGSHARE.13513890. https://ortogonline.com/doc/pt_br/OrtogOnLineMag/2/Slicer.html

[Moraes_et_al_2023_b] Moraes , C., Habicht , M. E., Galassi, F. M., Varotto, E., & Beaini , T. (2023). Pharaoh Tutankhamun: a novel 3D digital facial approximation. Italian Journal of Anatomy and Embryology, 127(1), 13–22. https://doi.org/10.36253/ijae-14514

[Moraes_and_Suharschi_2022_b] Moraes, C., & Suharschi, I. (2022). Mensuração de Dados Faciais Ortográficos em Moldavos e Comparação com Outras Populações. figshare. https://doi.org/10.6084/M9.FIGSHARE.20089754. https://ortogonline.com/doc/pt_br/OrtogOnLineMag/4/Moldavos.html

[Ritchie_et_al_2018_b] Ritchie, S. J., Cox, S. R., Shen, X., Lombardo, M. V., Reus, L. M., Alloza, C., Harris, M. A., Alderson, H. L., Hunter, S., Neilson, E., Liewald, D. C. M., Auyeung, B., Whalley, H. C., Lawrie, S. M., Gale, C. R., Bastin, M. E., McIntosh, A. M., & Deary, I. J. (2018). Sex Differences in the Adult Human Brain: Evidence from 5216 UK Biobank Participants. In Cerebral Cortex (Vol. 28, Issue 8, pp. 2959–2975). Oxford University Press (OUP). https://doi.org/10.1093/cercor/bhy109

[Sarkic_et_al_2024_b] Šarkić, N., Cighetti, R., Schendzielorz, S.-K., & Mihaljević, M. (2024). REST IN PIECES: AN ATYPICAL BURIAL FROM THE NECROPOLIS IN RAČEŠA (CROATIA), 13TH–16TH CENTURY. In J. Belaj, Z. Hunyadi, T. Tkalčec, S. Krznar, T. S. Ivančan, T. Karavidović, T. Kokotović, & S. Stingl (Eds.), MILITARY ORDERS AND THEIR HERITAGE (pp. 233–244). Institute of Archaeology.

[Zhou_et_al_2022_b] Zhou, S., Chan, K. C. K., Li, C., & Loy, C. C. (2022). Towards Robust Blind Face Restoration with Codebook Lookup Transformer (Version 2). arXiv. https://doi.org/10.48550/ARXIV.2206.11253

Chapter 3

Feminização e Masculinização no OrtogOnBlender: Proposta de Protocolo para Estudos de Casos

Pablo Huber

Cirurgião Plástico - Hospital Union e Perito Oficial Médico Legista – Polícia Científica do Paraná.

Lattes[30], ORCID[31]

Richard Gravalos

Cirurgião Dentista, Especialista em Cirurgia e Traumatologia Buco-Maxilo-Facial, Especialista em Ortodontia, Especialista em Saúde Pública/Saúde da Família, São Paulo - SP.

Lattes[32]

Arturo Frick Carpes

Otorrinolaringologista, Cirurgião Crânio Maxilo Facial, Médico do Sono, Doutor em Ciências pelo Departamento de Cirurgia Plástica da FM-USP.

Lattes[33], Homepage.[34]

Rodrigo Dornelles

Cirurgião Plástico, Núcleo de Plástica Avançada - NPA, São Paulo-SP

Google Scholar[35], ResearchGate[36]

Cicero Moraes

3D Designer, Arc-Team Brazil, Sinop-MT, Brazil - Bachelor's degree in Marketing, Dr. h. c. FATELL/FUNCAR (Brazil) and CEGECIS (Mexico) - Member of Sigma Xi, Mensa Brazil, Poetic Genius Society, and International Society for the Study of Creativity and Innovation (ISSCI) - Invited reviewer: Elsevier, Springer Nature, PLoS, and LWW - Guinness World Records 2022: First 3D-printed tortoise shell.

Google Scholar[37], ResearchGate[38], ORCID[39], Homepage.[40]

[30] http://lattes.cnpq.br/8366660140529282
[31] https://orcid.org/0000-0003-2351-0153
[32] http://lattes.cnpq.br/5580397716843783
[33] http://lattes.cnpq.br/1809446535828892
[34] https://www.arturocarpes.com.br/
[35] https://scholar.google.com/citations?user=ZNqVhQYAAAAJ&hl=pt-BR
[36] https://www.researchgate.net/profile/Rodrigo-Dornelles
[37] https://scholar.google.com.br/citations?user=u33uvHUAAAAJ
[38] https://www.researchgate.net/profile/Cicero-Moraes
[39] https://orcid.org/0000-0002-9479-0028
[40] http://www.ciceromoraes.com.br

Data da publicação: 24 de abril de 2026
ISSN: **2764-9466** (Vol. 7, nº 2, 2026)
DOI: 10.6084/m9.figshare.32089966

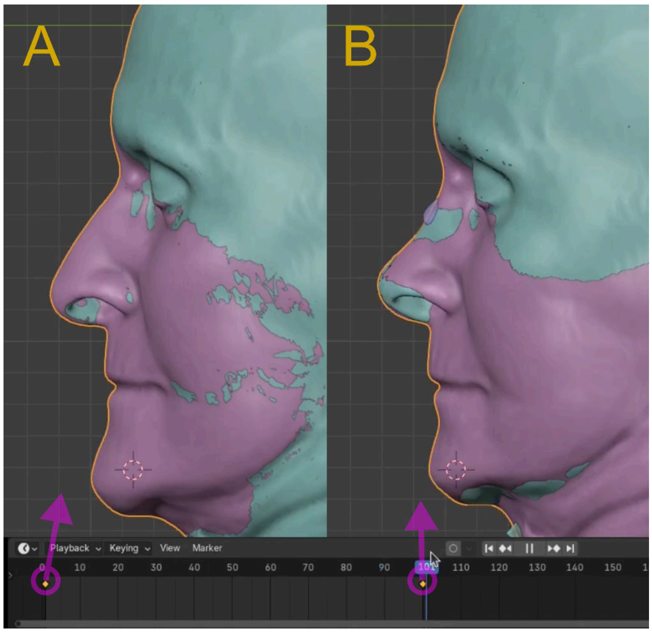

Resumo

Este estudo apresenta um protocolo digital voltado ao planejamento de intervenções de feminização e masculinização facial, utilizando o ecossistema do OrtogOnBlender. A metodologia integra duas abordagens complementares: a manipulação estrutural por meio de osteotomias digitais e a técnica de deformação anatômica. A utilização do fluxo de planejamento ortognático torna o processo mais prático e fundamentado, aproveitando protocolos já validados para otimizar a visualização volumétrica das estruturas. Enquanto a primeira foca no realinhamento das peças ósseas para estabelecer as bases do perfil facial, a segunda permite uma simulação volumétrica altamente precisa do tecido mole e o ajuste fino de regiões específicas, como a glabela e a proeminência laríngea. Os resultados demonstram uma convergência significativa entre os métodos, com variações estruturais mínimas, o que valida a previsibilidade estética do fluxo de trabalho. O protocolo permite transitar entre o planejamento ósseo e o refinamento de partes moles de forma interativa, facilitando a confecção de guias cirúrgicos e a simulação de próteses ou inserção capilar.

Palavras-chave: Planejamento Virtual, Deformação Anatômica, Feminização, Masculinização.

Attention: O presente texto configura um fragmento da atividade[41] intitulada 'Mesa Redonda 7: Face: Vídeo, Volume e Vitalidade', apresentada no âmbito da 41ª Jornada Sul-Brasileira de Cirurgia Plástica, sediada em Porto Alegre (RS), de 23 a 25 de abril de 2026.

3.1 Introdução

O OrtogOnBlender (OOB) é um add-on originalmente desenvolvido para o planejamento de cirurgia ortognática [Cunha_et_al_2020_c] [Lobo_et_al_2022_c], mas que progressivamente foi adaptado a outras finalidades, correção de fraturas mandibulares [Facanha_et_al_2021_c], como retalhos microcirúrgicos, cranioplastias, rinoplastias [Sobral_et_al_2021_c], correções mandibulares em neonatos [Duarte_et_al_2023_c], ducumentação urológica, próteses faciais [Salazar_et_al_2022_c], próteses veterinárias [Taub_2024_c] e reconstrução facial forense [Moraes_et_al_2024_c], além da masculinização e feminização no âmbito da cirurgia plástica.

A aplicação em abordagens tão distintas é viabilizada pela flexibilidade de sua interface abrangente que, embora demande uma curva de aprendizado mais acentuada, confere aos usuários significativa liberdade para adaptá-lo às suas necessidades técnicas, independentemente do escopo original ou das documentações disponíveis.

O presente manuscrito aborda a utilização de soluções integradas ao OOB que podem ser adaptadas ao estudo de casos de feminilização e masculinização, constituindo uma ferramenta robusta não apenas para a previsibilidade da unidade estética cervicofacial, mas também para a confecção de guias a serem utilizados no transcirúrgico.

3.2 Proposta Prática de Protocolo Baseada em Segmentação Ortognática

Important: A demonstração prática deste item possui caráter estritamente didático, não se configurando como uma simulação efetiva. A tomografia utilizada integra a coleção de exemplos[42] do software OsiriX; o arquivo foi baixado em 2012 e está sendo empregado neste exemplo para fins puramente acadêmicos e não comerciais. A escolha por esta abordagem fundamenta-se na praticidade operacional, uma vez que utiliza ferramentas com protocolos de planejamento e execução já estabelecidos e amplamente publicados na literatura científica.

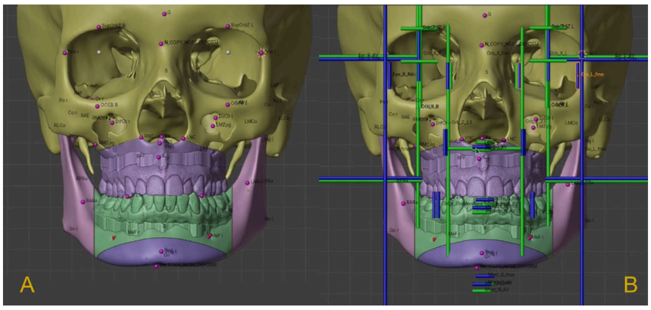

Figura3.1: A) Crânio composto com osteotomias. B) Projeções das estruturas anatômicas.

Primeiramente, o usuário procede com o planejamento da cirurgia ortognática até a configuração das osteotomias (Fig. 3.1, A) e do tecido mole (ver [Moraes_et_al_2020_c]). Embora o objetivo final possa não contemplar a realização de uma cirurgia ortognática propriamente dita, a aplicação desta metodologia facilita significativamente a visualização volumétrica das mudanças estruturais, servindo como um guia paramétrico para o restante da harmonização. Em seguida, são adicionados os marcadores de médias e proporções anatômicas (Fig. 3.1, B). Estes funcionam como uma referência estrutural tanto para a anatomia do crânio, demarcando, entre outros, os limites horizontais dos gônios e os limites verticais do ponto nasolabial, incisivos e mento; quanto para o tecido mole, abrangendo a medida horizontal das asas nasais, olhos e lábios, além das medidas verticais das orelhas [Moraes_et_al_2024_c]. No contexto didático, duas aulas sobre a metodologia de projeção estão disponíveis on-line em: aula 1[43] e aula 2[44].

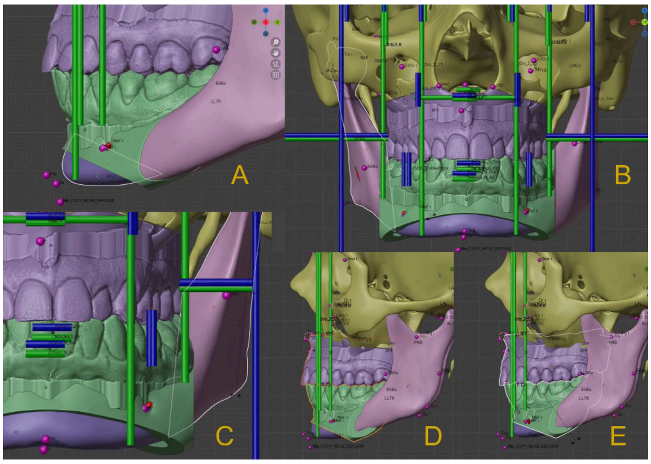

Figura3.2: Ajuste das osteotomias.

[41] https://sbcpsulbrasileira.com.br/evento/jornadasbcp2026/programacao/palestrante/61222
[42] https://www.osirix-viewer.com/resources/dicom-image-library/
[43] https://www.youtube.com/watch?v=U6oYkEmfyWo
[44] https://www.youtube.com/watch?v=Vcz2e5uSFX8

A utilização das ferramentas já disponíveis no OOB permite que o usuário proceda com o ajuste estrutural das osteotomias, buscando uma harmonia anatômica que compatibilize e evidencie aspectos gráceis à face. No presente caso, o mento foi retraído (Fig. 3.2, A), a região dos gônios foi reduzida no eixo horizontal X (Fig. 3.2, B e C) e o prognatismo mandibular foi abrandado (Fig. 3.2, D e E).

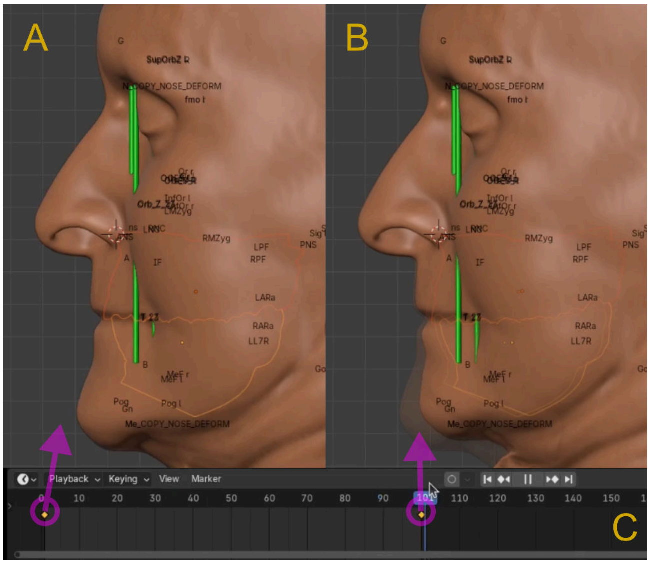

Figura3.3: Pré e pós prévio - visualização interativa. A imagem B contém sobreposição de imagens para evidenciar o ajuste estrutural.

Durante o processo de ajuste das osteotomias, o usuário pode visualizar os estados anterior (Fig. 3.3, A) e posterior (Fig. 3.3, B) por meio do deslocamento do cursor na Timeline, que anima a transição entre as configurações original e ajustada (Fig. 3.3, C).

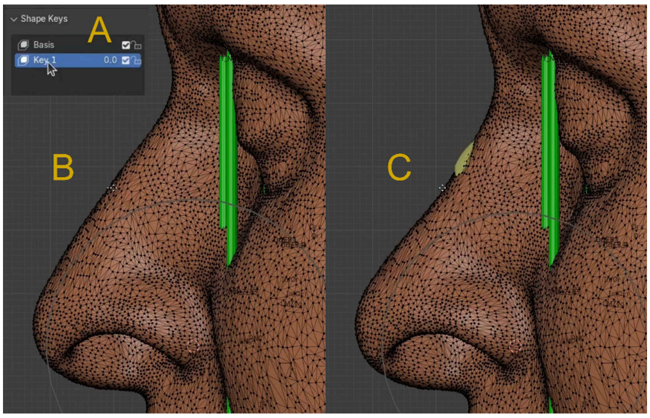

Figura3.4: Rinoplastia utilizando os Shape Keys do Blender.

O OOB fornece ao usuário a possibilidade de trabalhar com rinoplastia utilizando elementos de projeção estrutural. Esta abordagem pode ser adaptada para funcionar em conjunto com as ferramentas de ortognática por meio dos Shape Keys, pois estes permitem a criação de estados da malha 3D que podem ser aplicados integralmente ou em regiões distintas, com diferentes intensidades. Neste caso, foi configurado um estado original da malha e outro representando a rinoplastia (Fig. 3.4, A). Para que o ajuste seja efetuado, é necessário trabalhar no Edit Mode (Fig. 3.4, B), adequando a estrutura ao formato desejado (Fig. 3.4, C).

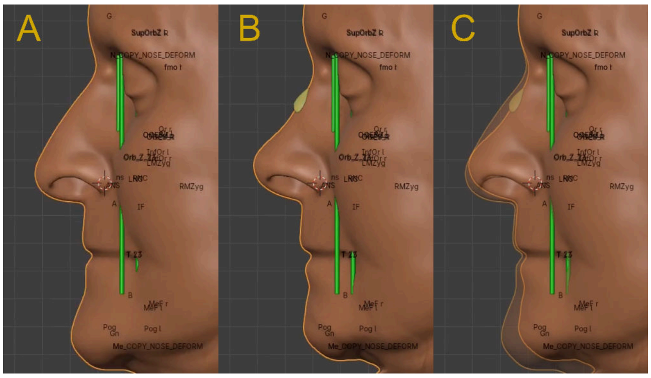

Figura3.5: Visualização do pré (A) e pós (B), com sobreposição (C).

Os estados do Shape Key podem ser animados, unificando os cenários pré e pós-operatórios na Timeline do Blender (Fig. 3.5). É possível, ainda, adicionar configurações complementares à face, como a suavização da região da glabela e da proeminência laríngea, além de outras implementações, como a capilar e afins.

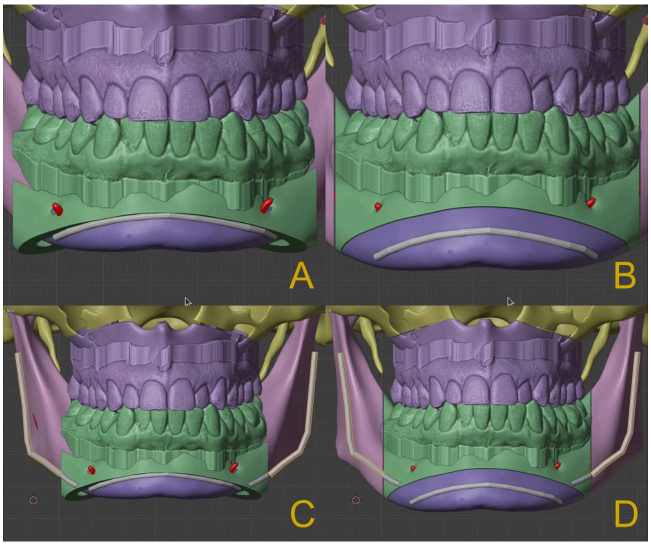

Figura3.6: Projeções dos cortes a partir dos pós digital.

Uma vez que o usuário estipula o volume da estrutura a ser subtraído, torna-se possível demarcar os limites futuros do pós-cirúrgico (Fig. 3.6, A e C) e retornar ao estado original da estrutura para identificar onde as osteotomias devem ser efetuadas (Fig. 3.6, B e D). No caso do mento, como este foi ajustado aos novos limites e perderá volume em função dessa restrição, a linha de corte é parentada ao objeto; assim, ao retornar ao ponto original, ela demarca com precisão a área de ressecção. No caso dos ramos direito e esquerdo, a abordagem é distinta, pois estes serviram apenas para o ajuste dos limites marginais; logo, a delimitação permanece inalterada, uma vez que o objetivo era determinar o desgaste necessário para alcançar a gracilidade desejada. De qualquer forma, o usuário detém total controle sobre o espaço e o tempo, podendo avançar e retornar na

Timeline, alterar os pontos de corte e ajustar as intensidades das deformações.

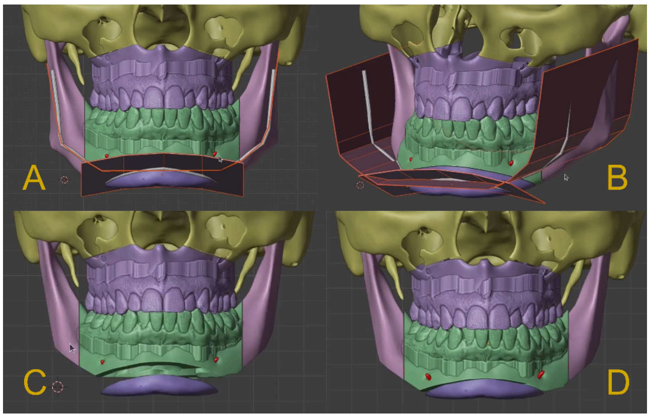

Figura3.7: Planos de corte e osteotomias.

Utilizando as ferramentas de planos de corte, o usuário ajusta os mesmos às projeções estipuladas. Esses planos são fundamentais no momento de criar os guias de corte, pois sua estrutura servirá como base para as operações booleanas que os gerarão (Fig. 3.7, A e B). Devido às diferentes abordagens, o mento remanescente fica inicialmente afastado da mandíbula, enquanto os ramos já se encontram em sua posição final (Fig. 3.7, C). Em seguida, a posição final do mento também é ajustada e a mandíbula pretendida é finalizada (Fig. 3.7, D).

Important: É importante ressaltar que, embora o exemplo prático foque em um caso de feminização, a técnica é plenamente adaptável para a masculinização. Nesse cenário, o efeito masculinizador seria evidenciado pelo maior distanciamento dos gônios e pela expansão projetiva do mento, seguindo a mesma lógica metodológica de ajuste estrutural. Além disso, o uso de recursos complementares para o refinamento estético, como a simulação de próteses, será abordado detalhadamente no decorrer deste texto.

3.3 Protocolo Baseado em Deformação Anatômica

A deformação anatômica é uma abordagem que consiste em converter um indivíduo em outro (humano [Moraes_et_al_2024_c] ou não [Moraes_et_al_2022_c]) ou uma espécie em outra [Bezzi_and_Moraes_2015_c], por meio da deformação do crânio com influência no tecido mole. Tal técnica é bastante flexível e permite o ajuste de um adulto em uma criança [Moraes_et_al_2024b_c], bem como a transição de um indivíduo saudável para outro com algum quadro sindrômico, como, por exemplo, a acondroplasia [Moraes_et_al_2024c_c]. Dadas estas possibilidades, a técnica evidencia-se como uma ferramenta apta para o uso no contexto de feminização e masculinização. No entanto, este caso, diferentemente dos demais supracitados que envolviam indivíduos distintos, trata-se do mesmo paciente, de modo que o doador virtual será ele próprio.

Uma videoaula explicativa sobre a técnica pode ser assistida on-line[45].

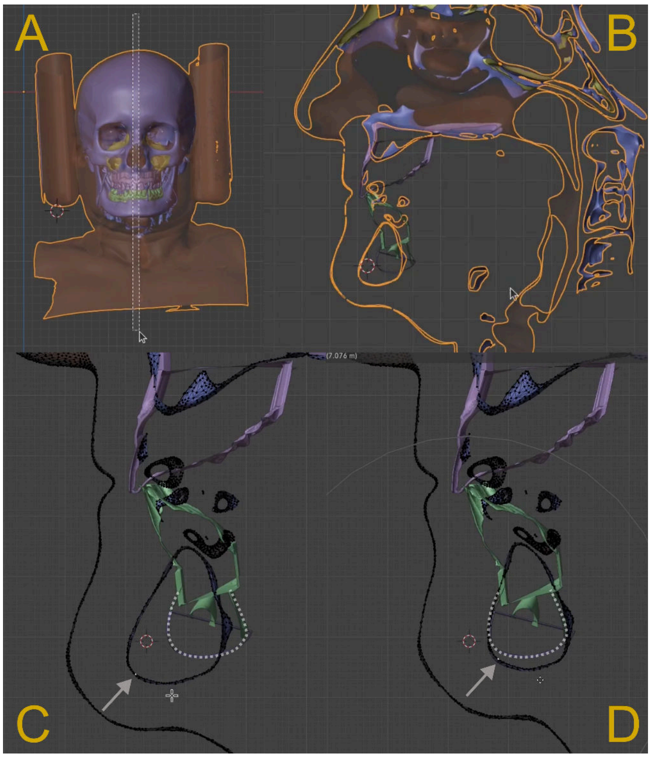

Figura3.8: Deformação anatômica.

Uma malha única, composta pelo crânio completo e pelo tecido mole do indivíduo, é configurada (Fig. 3.8, A) e o ajuste é efetuado regionalmente, por meio de um corte ou Clipping Border (Fig. 3.8, B). O primeiro ajuste é realizado na região do mento, utilizando o Edit Mode do Blender, selecionando-se um vértice (Fig. 3.8, C) e deslocando-o com a influência dos vértices vizinhos, de modo que o deslocamento deforme a estrutura apenas regionalmente, adequando-a ao estado pós-operatório digital (Fig. 3.8, D).

Diferente da deformação por osteotomia, que utiliza as peças ósseas como parâmetro de ajuste estrutural e, portanto, já funciona diretamente via Timeline e movimentação interativa na 3D View, a deformação anatômica depende do ajuste no campo Value para animar a transição entre o pré e o pós-operatório em um primeiro momento (Fig. 3.9).

Se o usuário desejar, pode unificar todas as animações na Timeline, de modo que seja possível visualizar a evolução do pré e pós-operatório diretamente por lá. Na imagem de exemplo, os dois modelos da cabeça podem

[45] https://youtu.be/xig5_EcIFWA

ser vistos animados: o por osteotomia e o via deformação anatômica (Fig. 3.10).

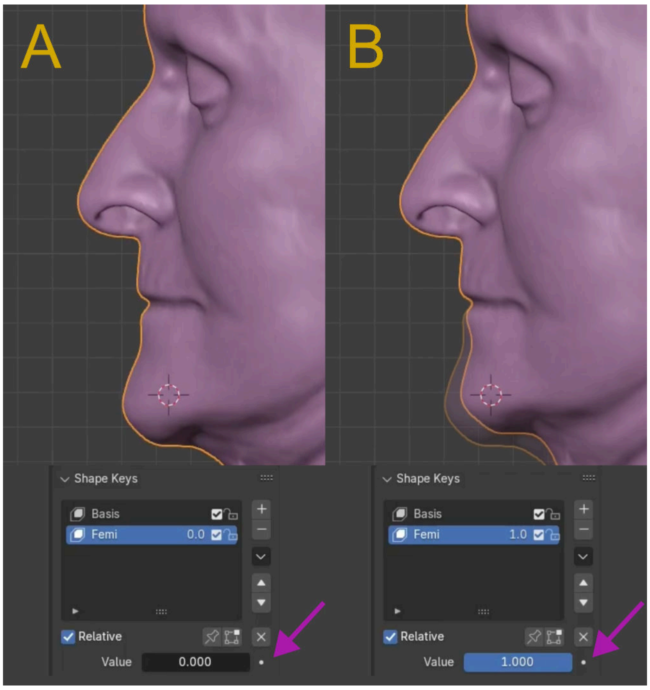

Figura3.9: Animação dos estados via Shape Keys. A) Estado inicial sem ajuste, com o Value em 0. B) Estado final com os ajustes e o Value em 1.

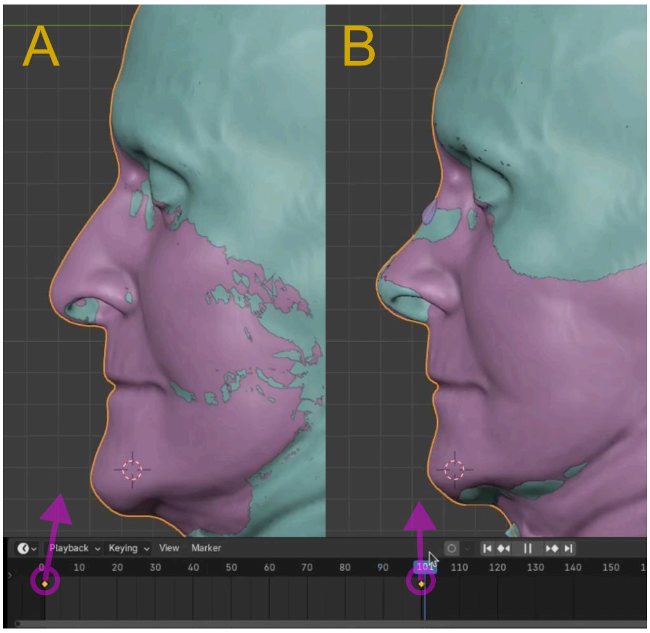

Figura3.10: Deformação anatômica finalizada e animada na Timeline, ambos os modelos estão na cena, sendo o estado inicial no quadro 1 (A) e o estado final, ou seja, o pós cirúrgico no quadro 100 (B).

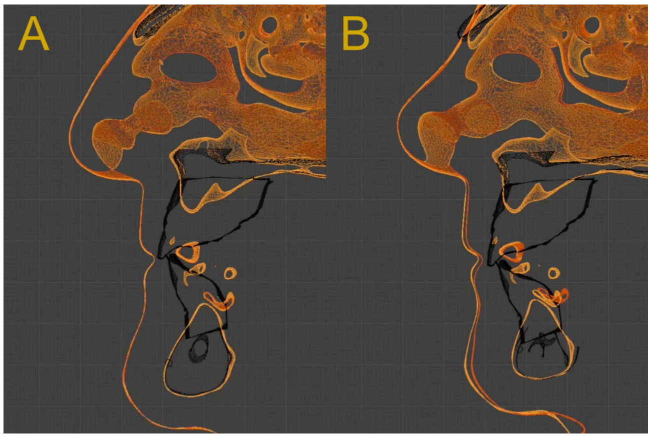

Figura3.11: A) Estado inicial. B) Estado final ou pós ciúrgico.

Embora se trate de duas abordagens diferentes, ao final do processo, a técnica de osteotomia digital e a de deformação anatômica convergiram para um resultado compatível (Fig. 3.11). Esta compatibilidade também foi observada no âmbito da reconstrução facial forense, posto que o traçado do perfil da face a partir de marcadores de espessura de tecido mole e projeção nasal geralmente é muito semelhante ao perfil advindo da deformação anatômica [Moraes_et_al_2024_c].

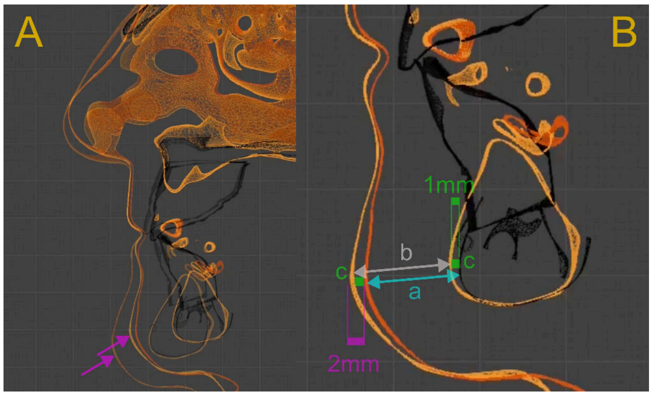

Figura3.12: A) Pré e pós sobrepostos com as setas em pink demonstrando o significativo deslocamento. B) Detalhes estruturais evidenciando o erro mínimo entre os modelos.

Um fato que merece atenção neste trabalho é que, ao se observar detalhadamente o deslocamento estrutural (Fig. 3.12, A), percebe-se que a deformação do mento, via deformação anatômica, não respeitou o espaço exato daquele ajustado via osteotomia, distanciando-se um pouco mais de um milímetro (Fig. 3.12, B-a,b). Mesmo assim, a diferença na parte mais extrema do queixo foi menor do que 2 milímetros (Fig. 3.12, B-c). Em linhas gerais, mesmo com pequenas imprecisões de ajuste, as técnicas geram resultados muito próximos um do outro.

Important: Um vídeo demonstrativo curto das duas técnicas supra abordadas pode ser assistido online[46].

3.4 Possibilidades Complementares

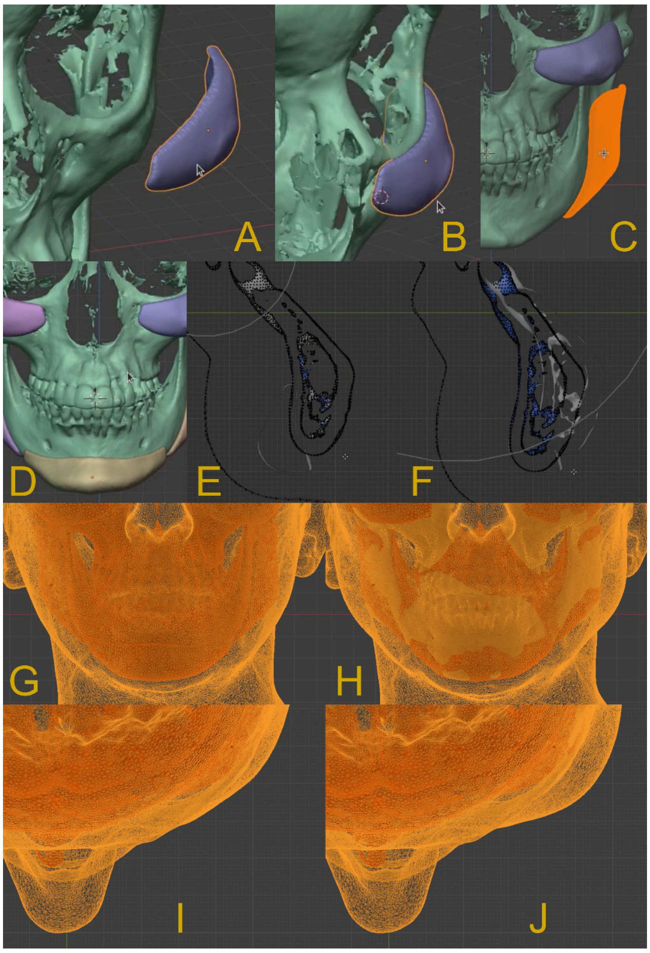

Figura3.13: Colocação de próteses e impacto estrutural com a deformação anatômica.

A deformação anatômica funciona muito bem para a simulação volumétrica de próteses. É necessário apenas que se façam ajustes estruturais para que a peça se encaixe no crânio (Fig. 3.13, A-D); em seguida, é efetuada a deformação para compatibilizá-la com o volume do pós-cirúrgico (Fig. 3.13, E-F). Com essas intervenções e as configurações supramencionadas, torna-se possível visualizar o pré e o pós-operatório de maneira interativa (Fig. 3.13, G-J).

Além das questões já abordadas, é possível ainda ajustar estruturas como a glabela e a proeminência laríngea, deformando a malha com os Shape Keys, mas não apenas isso.

A inserção capilar ou o ajuste do couro cabeludo também podem ser configurados. Para isso é elegida a área

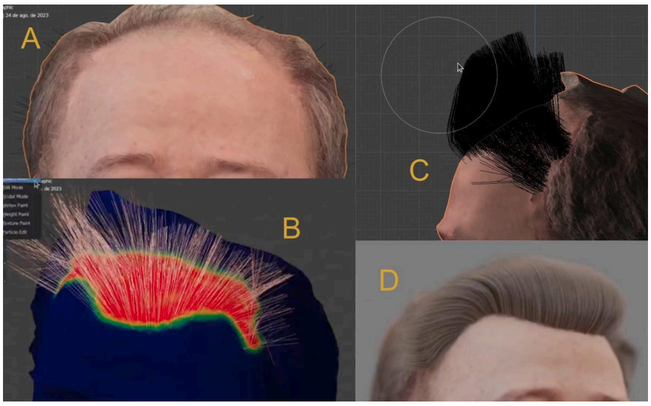

Figura3.14: Inserção capilar digital.

de interesse (Fig. 3.14, B), os fios são penteados digitalmente para se equipararem aos demais (Fig. 3.14, C) e ao final uma renderização é feita para a visualização do resultado (Fig. 3.14, D).

3.5 Conclusão

A implementação do protocolo de feminização e masculinização facial no ambiente do OrtogOnBlender demonstra a maturidade e a versatilidade das ferramentas de código aberto aplicadas à cirurgia plástica e crânio-maxilo-facial. O estudo evidencia que tanto a abordagem baseada em osteotomias digitais quanto a técnica de deformação anatômica são métodos eficazes e complementares para o planejamento cirúrgico moderno.

Um ponto fundamental observado é a alta precisão na convergência de resultados entre as duas técnicas. A variação mínima encontrada, inferior a dois milímetros nas áreas de maior projeção, valida a deformação anatômica como uma ferramenta de alta previsibilidade, sendo especialmente útil quando o objetivo é a simulação volumétrica e a harmonia estética sem a necessidade imediata de segmentação óssea complexa.

Além disso, a integração de recursos como o controle interativo via Timeline, o uso de Shape Keys para ajustes finos e a possibilidade de simulação capilar e de próteses confere ao cirurgião uma visão holística do paciente. Essa capacidade de transitar entre o planejamento estrutural ósseo e o estético de partes moles em um único ambiente digital não apenas amplia a segurança do procedimento, mas também melhora a comunicação com o paciente ao oferecer visualizações realistas do pós-operatório.

[46] https://youtu.be/JoWIuR3QIdA

3.6 Referências Bibliográficas

[Bezzi_and_Moraes_2015_c] Bezzi, L., & Moraes, C. (2015). Archaeological forensic facial reconstruction with FLOSS. In Proceedings of the 43rd Annual Conference on Computer Applications and Quantitative Methods in Archaeology (p. 416). Siena, Italy. https://sites.caa-international.org/caa2015/wp-content/uploads/sites/14/2015/04/Book-of-Abstracts_CAA20151.pdf

[Cunha_et_al_2020_c] Cunha, H. S., da Costa Moraes, C. A., de Faria Valle Dornelles, R., & da Rosa, E. L. S. (2020). Accuracy of three-dimensional virtual simulation of the soft tissues of the face in OrtogOnBlender for correction of class II dentofacial deformities: an uncontrolled experimental case-series study. In Oral and Maxillofacial Surgery (Vol. 25, Issue 3, pp. 319–335). Springer Science and Business Media LLC. https://doi.org/10.1007/s10006-020-00920-0

[Duarte_et_al_2023_c] Duarte, D. W., Fleith, I. J., Pinheiro, R. C., Machado, M. F., Zanin, E. M., & Collares, M. V. M. (2023). Mandibular morphology and distraction osteogenesis vectors in patients with Robin sequence. In International Journal of Oral and Maxillofacial Surgery (Vol. 52, Issue 4, pp. 442–450). Elsevier BV. https://doi.org/10.1016/j.ijom.2022.07.007

[Facanha_et_al_2021_c] Façanha de Carvalho, E., Alkmin Paiva, G. L., Yonezaki, F., & Machado, G. G. (2021). Computer-Aided Surgical Simulation in Severe Atrophic Mandibular Fractures: A New Method for Guided Reduction and Temporary Stabilization Before Fixation. In Journal of Oral and Maxillofacial Surgery (Vol. 79, Issue 4, p. 892.e1-892.e7). Elsevier BV. https://doi.org/10.1016/j.joms.2020.11.011

[Lobo_et_al_2022_c] Lobo, F., Filho, L. I., Sigua-Rodriguez, E. A., da Silva, B. G., Tolentino, E. de S., Borges, Y. M., da Silva, M. C., Tonin, R. H., & Iwaki, L. C. V. (2022). Evaluation of ortogonblender software bone movement tools in bimaxillary orthognatic surgeries performed in dolphin software. In Journal of Stomatology, Oral and Maxillofacial Surgery (Vol. 123, Issue 4, pp. 417–421). Elsevier BV. https://doi.org/10.1016/j.jormas.2021.10.001

[Moraes_et_al_2020_c] Moraes, C., Rosa, E. da, & Dornelles, R. (2020). Protocolo de Planejamento Digital de Cirurgia Ortognática. figshare. https://doi.org/10.6084/M9.FIGSHARE.12923813

[Moraes_et_al_2022_c] Moraes, C., Pereira, H. M., Requicha, J. F., Alves, L., Alexandre-Pires, G., de Jesus, S., Guimarães, S., Ginja, C., Detry, C., Ramalho, M., & Pires, A. E. (2022). The Facial Reconstruction of a Mesolithic Dog, Muge, Portugal. Applied Sciences, 12(10), 4867. https://doi.org/10.3390/app12104867

[Moraes_et_al_2024_c] Moraes, C., Galassi, F. M., Sineo, L., Šindelář, J., Varotto, E., Mietlińska-Sauter, J., Antunes-Ferreira, N., Habicht, M. E., & Beaini, T. (2024). The anatomical bases of the 3D digital facial approximation of the Zlatý kůň 1 woman (ca. 43,000 BP). Anthropological Review, 87(2), 85–97. https://doi.org/10.18778/1898-6773.87.2.04

[Moraes_et_al_2024b_c] Moraes, C., Varotto, E., Artico, M., Galassi, F. M., Forte, F., & Habicht, M. E. (2024). 3D facial approximation and endocast analysis of the Mummy of Minirdis (Ancient Egypt, ca. 2,300 Before Present). Morphologie, 108(362), 100781. https://doi.org/10.1016/j.morpho.2024.100781

[Moraes_et_al_2024c_c] Moraes, C., Krenz-Niedbała, M., Łukasik, S., & Prada, C. S. (2024). Forensic facial approximation of an individual with achondroplasia from medieval cemetery in Central Europe. Digital Applications in Archaeology and Cultural Heritage, 32, e00301. https://doi.org/10.1016/j.daach.2023.e00301

[Salazar_et_al_2022_c] Salazar-Gamarra, R., Cárdenas-Bocanegra, A., Masch, U., Da Costa Moraes, C. A., Seelaus, R., Lopes Da Silva, J. V., & Lauria Dib, L. (2022). Color translation from monoscopic photogrammetry +ID Methodology into a Polyjet final 3D printed facial prosthesis. In F1000Research (Vol. 11, p. 582). F1000 Research Ltd. https://doi.org/10.12688/f1000research.111196.1

[Sobral_et_al_2021_c] Sobral, D. S., Duarte, D. W., Dornelles, R. F. V., & Moraes, C. A. C. (2021). 3D Virtual Planning for Rhinoplasty Using a Free Add-On for Open-Source Software. In Aesthetic Surgery Journal (Vol. 41, Issue 8, pp. NP1024–NP1032). Oxford University Press (OUP). https://doi.org/10.1093/asj/sjab085

[Taub_2024_c] Taub, B. (2024). Injured tortoise zooms around on new wheels thanks to 3D-printed prosthesis. IFLScience. https://bit.ly/4eWxmKN

Chapter 4

Evaluation of Pre- and Post-Surgical Tomography via OrtogOnBlender

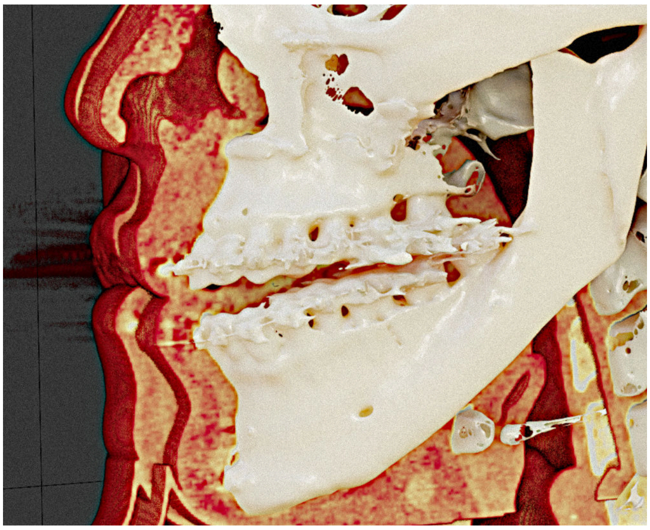

Abstract

This work presents a standardized protocol for the comparative analysis of pre- and post-operative tomographies using the OrtogOnBlender (OOB) add-on, in versions 291 and XP. The methodology focuses on the integration of voxel data and 3D meshes within a single project environment, optimizing the workflow by avoiding the execution of multiple software instances. Detailed procedures include hierarchical parenting, structural alignment via automatic or manual tools, and the adjustment of object constraints for unified boolean visualization. This guide aims to enable advanced users to perform precise clinical measurements and photorealistic overlays.

Keywords: *OrtogOnBlender, Computed Tomography, Surgical Planning, Blender, Open Science.*

Cicero Moraes
3D Designer, Arc-Team Brazil, Sinop-MT, Brazil - Bachelor's degree in Marketing, Dr. h. c. FATELL/FUNCAR (Brazil) and CEGECIS (Mexico) - Member of Sigma Xi, Mensa Brazil, Poetic Genius Society, and International Society for the Study of Creativity and Innovation (ISSCI) - Invited reviewer: Elsevier, Springer Nature, PLoS, Wiley, and LWW - Guinness World Records 2022: First 3D-printed tortoise shell.
Google Scholar[47], ResearchGate[48], ORCID[49], Homepage.[50]

Liat Segal-BenMoyal
Specialist in Oral and Maxillofacial Surgery in Wolfson Medical Center, Holon, Israel
ResearchGate[51], PubMed[52]

Publication date: May 4, 2026
ISSN: **2764-9466** (Vol. 7, No. 2, 2026)
DOI: 10.6084/m9.figshare.32163054

4.1 Introduction

Comparative analysis between pre- and postoperative states constitutes an essential clinical demand for evaluating surgical outcomes and therapeutic monitoring. Although the OrtogOnBlender (OOB) add-on provides tools for this purpose, the scarcity of didactic protocols hinders the learning curve and the practical application of the technology. The present work proposes a standardized methodology for volumetric comparison (voxel data in DICOM slices) and surface comparison (reconstructed 3D meshes), incorporating recent updates to the system's source code to meet the operational demands identified by users.

OOB provides computed tomography import tools for both voxel data and 3D mesh reconstruction based on Hounsfield scale factors. In OOB 291, the most utilized approaches are voxel data reconstruction via slices arranged in the sagittal and coronal planes [Moraes_et_al_2021_d]; regarding 3D meshes, the two most common methods are those based on Slicer [Moraes_et_al_2021b_d] and VTK-ITK [Moraes_et_al_2021c_d]. OOB XP improved the exam tracking and selection experience [Moraes_et_al_2024_d], in addition to implementing AI-based tissue segmentation [Moraes_et_al_2024b_d] and a unified head import system [Moraes_et_al_2025_d]. While the voxel data import interface has been simplified, it still largely follows the structural approach of the previous version.

Since the knowledge regarding the tomography import process—whether via voxel data or 3D mesh—is signifi-

[47] https://scholar.google.com.br/citations?user=u33uvHUAAAAJ
[48] https://www.researchgate.net/profile/Cicero-Moraes
[49] https://orcid.org/0000-0002-9479-0028
[50] http://www.ciceromoraes.com.br
[51] https://www.researchgate.net/profile/Liat-Segal-2
[52] https://pubmed.ncbi.nlm.nih.gov/?term=Benmoyal-Segal+L&cauthor_id=16805780

cantly documented, these parts will not be detailed. The present material will focus on the steps necessary to adjust the models so they occupy the same coordinate space, allowing for the comparison of exams.

Important: The approach described in this material is applicable to both OOB 291 and OOB XP.

4.2 How it Woks

Some structural modifications have been implemented in OOB, both in the 291 and XP versions, to provide support for pre- and post-surgical comparisons, or any other approach involving two or more tomographies and 3D meshes. However, despite these adjustments, it is still necessary for the user to open two instances of Blender—essentially running the program twice—to reconstruct the desired structures (specifically the voxel data and the 3D mesh) in each; subsequently, both models can be copied and pasted into the same file.

A way to circumvent this without opening two instances is simply to reconstruct one structure within the open Blender file and duplicate the entire set. This will generate objects with the ".001" suffix added to the original names (e.g., Bones will become Bones.001, SoftTissue as SoftTissue.001, and so forth). Once this is done, preferably by placing the tomography into a separate Collection named "BEFORE" or "AFTER," the original objects (Bones, SoftTissue, etc.) can be deleted and the second tomography imported. In this manner, the entire process can be conducted within a single file.

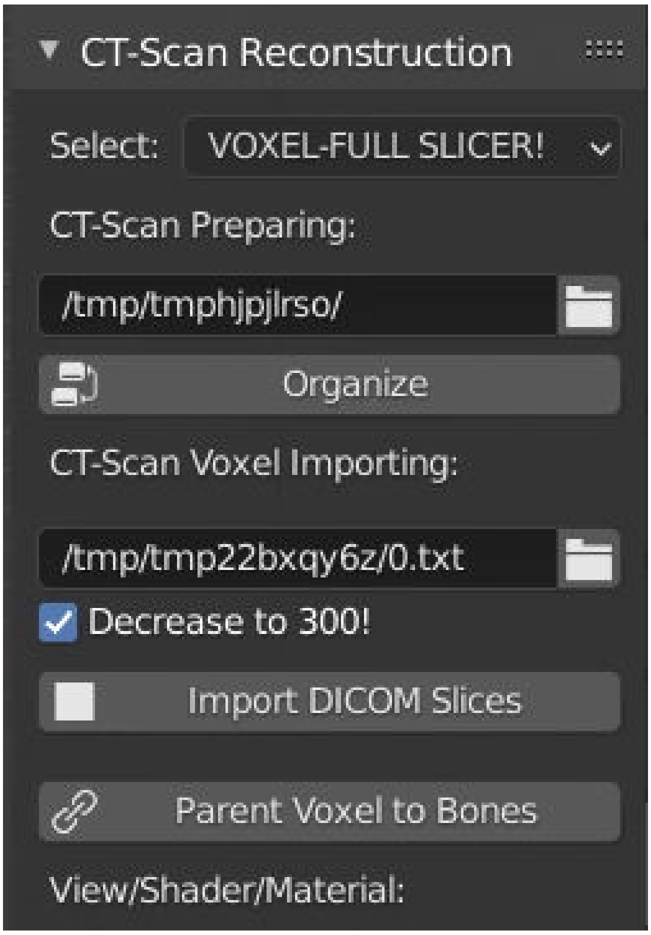

Figure4.1: New button as of version 2026-05-02 in OOB 291: Parent Voxels to Bones.

Attention: This material was developed for advanced OOB and Blender users, focusing exclusively on the technical details of new tools and solutions based on accumulated prior knowledge. Beginner users may find it difficult to follow the documentation and tests presented herein.

There is only one specific adjustment to be made in OOB 291 regarding the parenting of voxel data to the 3D mesh. Unlike OOB XP, where this process is automated and occurs without the need for direct intervention, in OOB 291, the operation must be executed manually via the "Parent Voxels to Bones" button (Fig. 4.1, bottom), located within the VOXEL-FULL SLICER panel.

Since OOB XP remains in the development phase and is currently focused entirely on orthognathic surgery, there is a greater feasibility for automating various functionalities. On the other hand, as OOB 291 is the release version widely utilized by specialists across different healthcare fields, its tools remain more comprehensive and feature a lower level of automation.

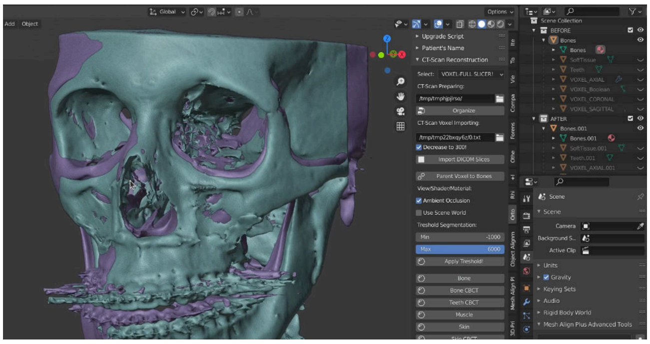

Figure4.2: Scene containing two datasets: BEFORE and AFTER, representing the pre- and post-surgical states. Since the voxel data is properly parented to the Bones object, maintaining the visibility of both meshes (Bones and Bones.001) is sufficient for the rest of the structural elements to follow any transformations.

As the voxel data and the other 3D meshes are linked (via parent/child hierarchy) to the Bones and Bones.001

objects, all spatial transformations applied to the "parent" elements will be replicated across their respective "children." Consequently, the alignment between the pre- and post-operative states can be performed while keeping only these primary meshes visible (Fig. 4.2). While, in theory, parenting the initial state is not mandatory, doing so grants the user the flexibility to perform additional pre-adjustments, such as aligning to the natural head position or the Frankfurt plane.

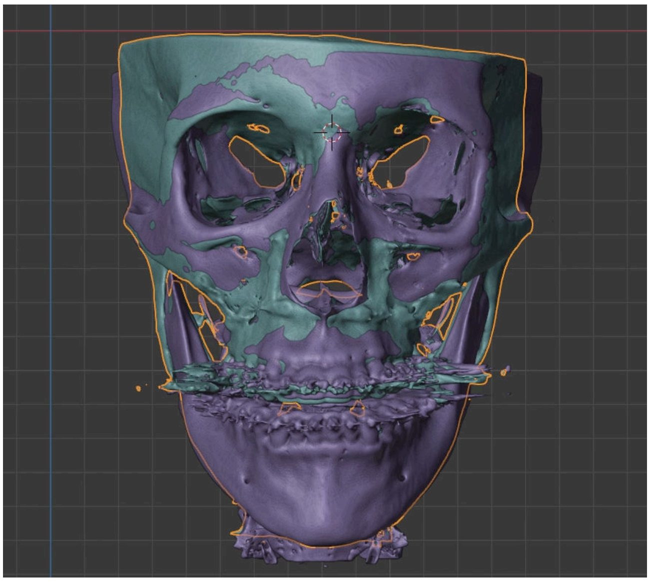

Figure4.3: Aligned skulls and, consequently, all other parented structures properly positioned.

Once the skulls (Bones and Bones.001) are aligned (Fig. 4.3), all dependent structures will be aligned as well. However, it is essential to note that even though they represent the same individual in pre- and post-operative states, minor structural bone discrepancies may occur. Such variations can arise from different tomograph parameterizations between acquisitions or from changes in non-surgical regions, such as dental movements resulting from orthodontic treatment. The user has several methods available for structural alignment, including ICP align (automatic), the OOB 291 Alignment tools (semi-automatic), manual adjustment, or a hybrid approach (automatic and manual).

Each voxel data block possesses its own "boolean cube," a structure utilized for internal visualization through displacements and boolean calculations. Since one of the datasets had to be realigned—undergoing translation and rotation to match the other—the respective visualization cube will be misaligned relative to the target. To correct this discrepancy, the displaced cube should be selected and assigned a Copy Transforms type Object Constraint. In this manner, the cube will mimic the behavior of the reference object, unifying the boolean visualization tool (Fig. 4.4).

When observing the overlap of the models under a more opaque rendering, such as Skin (Fig. 4.5), it is evident that the rotation of the voxel planes and the boolean limitation within the same physical space hinder a full visualization of the details. This issue can be mitigated by toggling the visibility of the Collection to which the voxel belongs or by applying a slight displacement between the voxel groups.

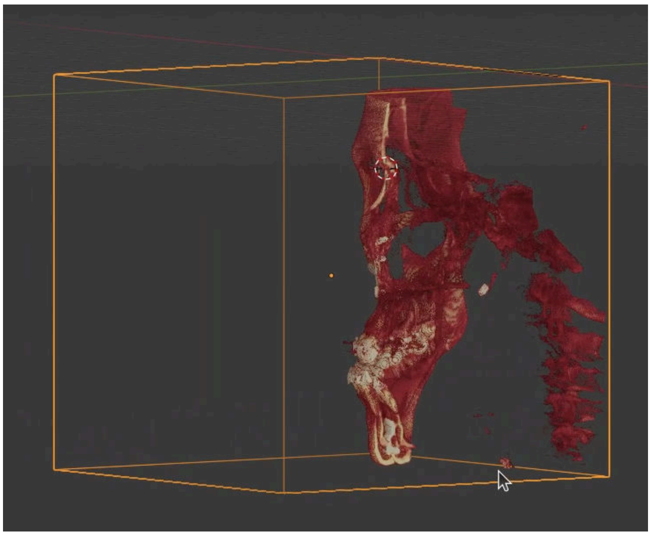

Figure4.4: Unified boolean block via Object Constraint.

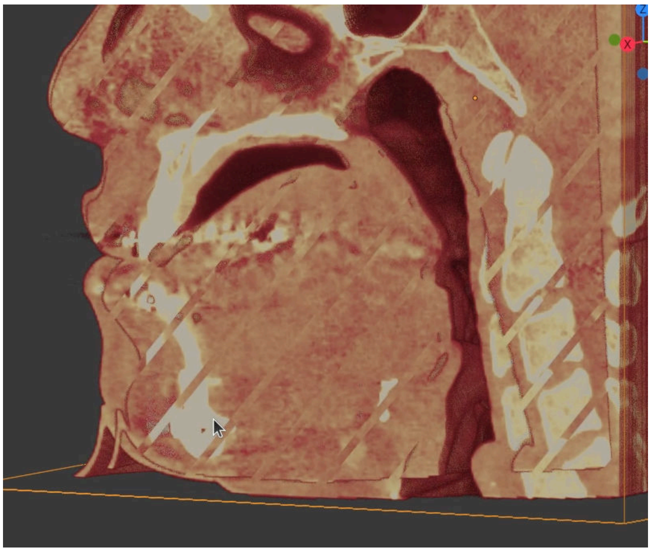

Figure4.5: Raw overlap of the models.

This positional adjustment can be achieved by decreasing the Influence parameter of the Copy Transforms Constraint or, alternatively, by individually manipulating the displacement of the other boolean object (Fig. 4.6).

With the structures properly aligned, the user can perform a series of measurements and clinical observations. In addition to delineating structures of interest for pre- and post-operative comparative analysis—as well as positioning spheres or other primitives to mark cephalometric points—it is possible to render images at the same cross-sectional plane for both states. This approach allows for the composition of visualizations either within the native Blender environment or in external software, such as Gimp (Fig. 4.7).

There is also the possibility of customizing the voxel ma-

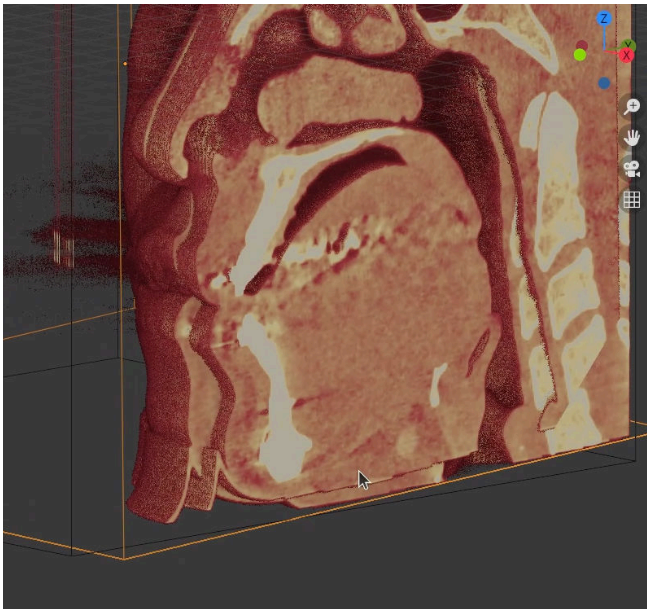

Figure4.6: Controlled displacement of booleans.

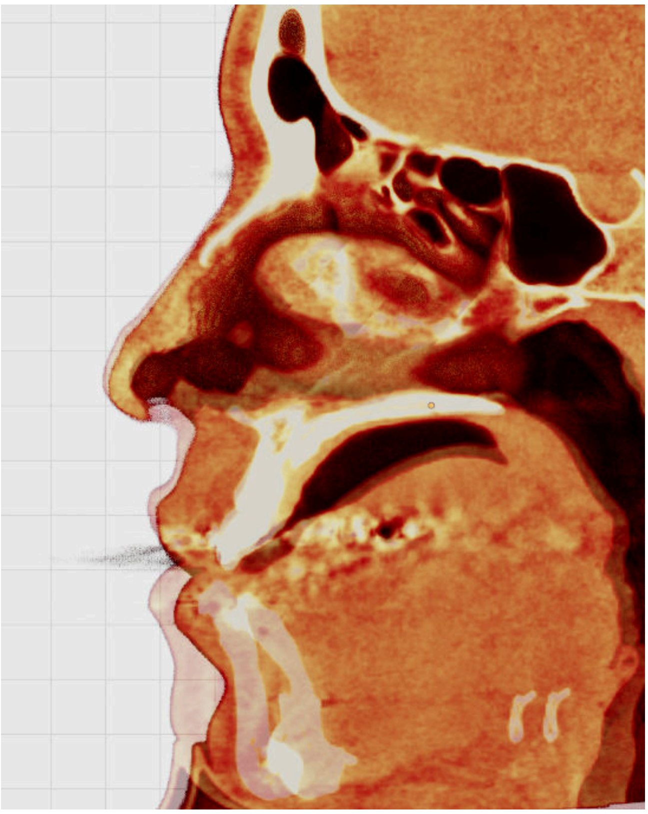

Figure4.7: Overlap of images rendered from an orthographic side view.

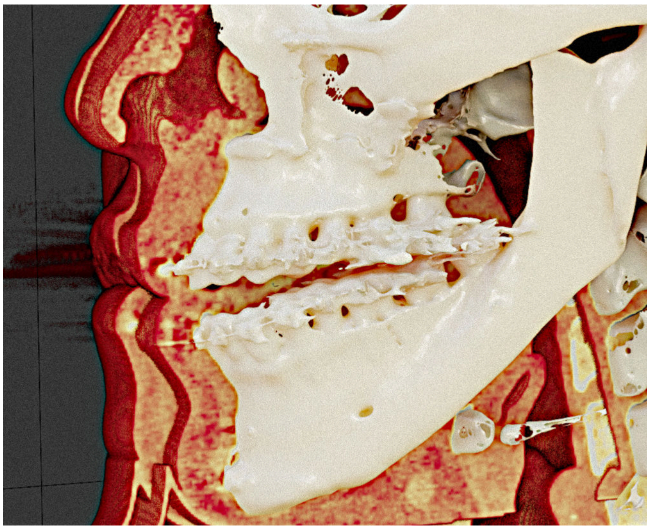

Figure4.8: Voxel data and 3D mesh overlay.

terials to visually distinguish between different datasets in an interactive manner. If the user desires, textured facial photogrammetry can be imported into the scene, enabling the observation of surface alterations with realistic coloration and appearance. By utilizing the techniques described in this manual, the user can generate a composite visualization of the voxel data and the 3D mesh, facilitating spatial and anatomical orientation (Fig. 4.8).

Note: A detailed video lesson has been made available on the official OrtogOnBlender course platform at https://ortogonline.eadplataforma.app/lesson/detail/5/168. However, in alignment with the principles of Open Science and open protocols, this material allows interested parties to replicate the procedure via text, provided they possess the necessary prior technical knowledge. While enrolling in the complete training[53] supports the project's sustainability, this document aims to meet the needs of users who may not be able to acquire it at this time.

4.3 Conclusion

The implementation of this protocol demonstrates that complex comparative analyses can be efficiently performed within the OOB open-source ecosystem. By mastering hierarchy management and alignment tools, the specialist achieves greater precision in therapeutic monitoring and the evaluation of surgical outcomes.

53 https://ortogonline.eadplataforma.app/plano/completo-semestral

4.4 References

[Moraes_et_al_2021_d] Moraes, C., Graf, M., Dornelles, R., & Rosa, E. da. (2021). Reconstrução de Voxel Data no OrtogOnBlender. figshare. https://doi.org/10.6084/M9.FIGSHARE.13670134.https://ortogonline.com/doc/pt_br/OrtogOnLineMag/2/VoxelSlicer.html

[Moraes_et_al_2021b_d] Moraes, C., Dornelles, R., & Rosa, E. da. (2021). Sistema de Reconstrução de Tomografia Computadorizada Baseado no Slicer 3D e no DicomToMesh. figshare. https://doi.org/10.6084/M9.FIGSHARE.13513890. https://ortogonline.com/doc/pt_br/OrtogOnLineMag/2/Slicer.html

[Moraes_et_al_2021c_d] Moraes, C., Dakir, I., Dornelles, R., & Rosa, E. da. (2021). Reconstrução de Tomografias com o VTK Python, o SimpleITK e o Multiprocessing. figshare. https://doi.org/10.6084/M9.FIGSHARE.14370902. https://ortogonline.com/doc/pt_br/OrtogOnLineMag/3/VTK_ITK_multi.html

[Moraes_et_al_2024_d] Moraes, C., Dakir, I., Startek, B., Dornelles, R., & Rosa, E. da. (2024). Ferramenta de Importação de Tomografia Computadorizada no OrtogOnBlender XP. figshare. https://doi.org/10.6084/M9.FIGSHARE.27648876. https://ortogonline.com/doc/pt_br/OrtogOnLineMag/10/CT_Scan.html

[Moraes_et_al_2024b_d] Moraes, C., Dakir, I., Startek, B., Dornelles, R., & Rosa, E. da. (2024). Segmentação de Tomografias Computadorizadas por IA no OrtogOnBlender XP. figshare. https://doi.org/10.6084/M9.FIGSHARE.27761970. https://ortogonline.com/doc/pt_br/OrtogOnLineMag/10/AI.html

[Moraes_et_al_2025_d] Moraes, C., Startek, B., Dakir, I., Schreiner, T., Dornelles, R., & Rosa, E. da. (2025). Sistema Unificado para a Criação de um Crânio Composto no OrtogOnBlender XP. figshare. https://doi.org/10.6084/M9.FIGSHARE.28135760. https://ortogonline.com/doc/pt_br/OrtogOnLineMag/11/Unificado.html

Chapter 5

Digital Facial Approximation and Digital Reconstruction of the Projectile Trajectory in Charles XII of Sweden: A 3D Biomechanical and Craniometric Analysis

Cicero Moraes | ORCID[54]
3D Designer, Arc-Team Brazil, Sinop-MT, Brazil - Bachelor's degree in Marketing, Dr. h. c. FATELL/FUNCAR (Brazil) and CEGECIS (Mexico)

Lis Moura | ORCID[55]
Physiotherapist (UNIC) and Zootechnician (UFMT), Sinop-MT, Brazil.

Thiago L. Beaini | ORCID[56]
Dental Surgeon, Faculdade de São Paulo - USP, Brazil

Luca Bezzi | ORCID[57]
Archaeologist, Arc-Team, Cles-TN, Italy

Alessandro Bezzi | ORCID[58]
Archaeologist, Arc-Team, Cles-TN, Italy

Jiří Šindelář | ORCID[59]
Surveyor, GEO-CZ, Tábor-Czech Republic

Michael Habicht | ORCID[60]
Egyptologist and Archaeologist, College of Humanities, Art and Social Sciences, Flinders University, Adelaide, South Australia, Australia

Elena Varotto | ORCID[61]
Archaeology, College of Humanities, Art and Social Sciences, Flinders University, Adelaide, South Australia, Australia

Francesco Maria Galassi | ORCID[62]
Department of Anthropology, Faculty of Biology and Environmental Protection, University of Lodz, 90-237 Łódź, Poland

Highlights

- *First quantitative cephalometric analysis of Charles XII reveals Class III maxillary retrognathism and mandibular prognathism, providing craniometric validation for features observed in historical portraits and the death mask.*
- *First complete 3D anatomical reconstruction integrating skull, brain voxel data, and intracranial venous system of Charles XII, enabling precise identification of structures damaged by the projectile.*
- *Spatial verification of the tricorn hat against the documented intracranial trajectory — a geometrical check absent from prior literature — confirms geometric compatibility with the left temporal entry point.*
- *Cranial reconstruction achieved exclusively from 1917 autopsy photographs and radiographs via anatomical deformation, demonstrating OrtogOnBlender's applicability to cases with no direct 3D scan available.*
- *Forensic facial approximation of Charles XII produced using open-source tools, converging with portrait evidence and death mask morphology through independent anatomical projections.*

Publication date: May 30, 2026
ISSN: **2764-9466** (Vol. 7, No. 2, 2026)
DOI: 10.6084/m9.figshare.32899616

54 https://orcid.org/0000-0002-9479-0028
55 https://orcid.org/0009-0007-0561-2320
56 https://orcid.org/0000-0003-0034-624X
57 https://orcid.org/0000-0002-4270-3420
58 https://orcid.org/0009-0002-7098-6138
59 https://orcid.org/0009-0009-9771-669X
60 https://orcid.org/0000-0002-0193-9672
61 https://orcid.org/0000-0001-6637-9402
62 https://orcid.org/0000-0001-8902-3142

Abstract

This study presents an unprecedented digital bioarchaeological and forensic analysis of Charles XII of Sweden, whose death in 1718 remains one of Europe's greatest historical mysteries. Utilizing open-source technologies, specifically the OrtogOnBlender ecosystem, the research performed a forensic facial approximation of the monarch and a 3D reconstruction of the fatal projectile's trajectory. In the absence of a direct 3D scan of the skull, the skeletal structure was reconstructed through anatomical deformation by cross-referencing metric data from photographs and radiographs taken during the 1917 exhumation. The results precisely corroborated the historical data from the last autopsy, confirming a nearly rectilinear and horizontal transfixing trajectory, with entry through the left temporal region and exit through the right. Innovatively, the study applied a USP standard cephalometric analysis, revealing a clinical condition of maxillary retrognathism associated with mandibular prognathism, which explains the projected lower lip physiognomy observed in portraits and the death mask. In addition to the face, the brain and vascular structures were modeled, allowing for the identification of the injured encephalic areas. Finally, the integration of the tricorne hat into the digital model demonstrated exact geometric compatibility with the ballistic path, filling gaps in previous studies and consolidating an efficient methodology for the analysis of complex historical cases.

Keywords: *Charles XII of Sweden, Forensic Facial Approximation, 3D Ballistic Trajectory, Cephalometry, Anatomical Reconstruction, OrtogOnBlender XP*

5.1 Introduction

5.1.1 Brief Biography of Charles XII

Charles XII was born in Stockholm on June 17, 1682, the son of Charles XI and Ulrika Eleonora of Denmark. After his mother's death in 1693, he developed a very close relationship with his father, accompanying him on official inspections and travels. Following Charles XI's death in 1697, he was declared of age and crowned at just 15 years old, becoming the last absolute monarch of Sweden. Described as a ruler of the early Enlightenment era, Charles XII was known for his asceticism and radical values. He was deeply committed to duty, possessed a solid education in theology and languages, and demonstrated remarkable shrewdness both as a statesman and as a general. His 21-year reign was defined by the defense of Sweden during the Great Northern War. Initially, he achieved brilliant victories (such as at Narva in 1700) and was regarded as a skilled tactician. However, the invasion of Russia (1707–1709) proved disastrous. He faced a scorched-earth strategy — the same one that would later weaken Napoleon and Hitler — along with the harsh Russian winter, culminating in the defeat at Poltava (1709), which destroyed the Swedish army and ended Sweden's status as a great power. After the defeat, he lived in forced exile for five years in the Ottoman Empire (present-day Moldova/Turkey), from where he continued attempting to influence European politics. He returned to Sweden in 1714, finding the empire in decline, yet still promoted significant domestic reforms and administrative measures that were ahead of their time. His life ended abruptly at the age of 36 on November 30, 1718, during the siege of the Fredrikshald fortress (in present-day Norway). He was struck in the temple by a projectile while inspecting the trenches — an event that marked the end of Swedish hegemony in the Baltic and remains one of history's greatest mysteries, as it is still debated whether the fatal shot was fired by an enemy or came from his own ranks (friendly fire) [Hatton_and_Nordlund_2026_e].

5.1.2 The Autopsies

Three autopsies were performed on the body of Charles XII: one in 1746, another in 1859, and the final one in 1917 [Junno_et_al_2022_e] [Key-Aberg_and_Stille_1918_e].

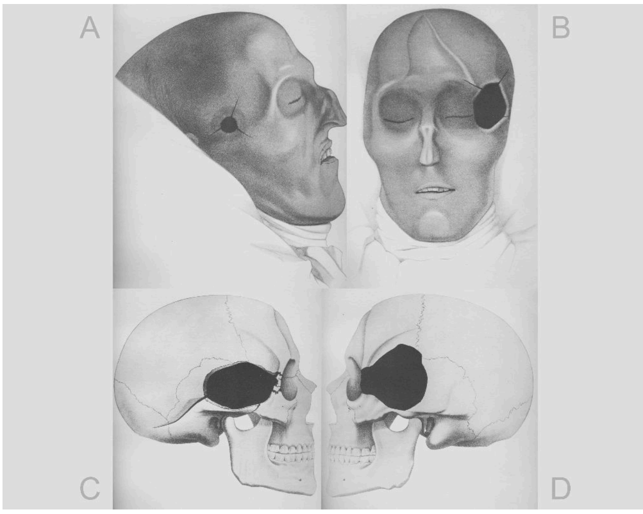

Figure5.1: Engravings from the **1859** autopsy. A) Soft tissue wound on the King's right temple. B) Soft tissue wound on the King's left temple. C) Representation on a surrogate skull (not the King's) of the cranial damage on the right side. D) Representation on a surrogate skull of the cranial damage on the left side. Public domain images. Digitization available at: https://brf-portalen.se/wp-dragoner/album/k12-banesar/index.html

The 1859 results indicated that the head wound was fatal, resulting from a firearm discharge that would have caused instantaneous death. The projectile entered through the left side, at the outer edge of the bony ring of the eye socket, and emerged slightly in front of the right ear in a nearly horizontal trajectory. Although uncertainties remained regarding the projectile type, it was considered more likely to be a musket ball or a canister shot, and less likely to be a piece of scrap metal or a bomb fragment. Based on the distance it traveled after transfixing the King's head, it was estimated that the projectile was already decelerating at the moment of impact. The investigation evidenced that it was a lesion caused by a single projectile, with no residues found inside the skull [Key-Aberg_and_Stille_1918_e]. The examination relied on manual illustrations of the King's head and utilized a surrogate skull as a didactic element to project the damage onto the bone tissue (Fig. 5.1).

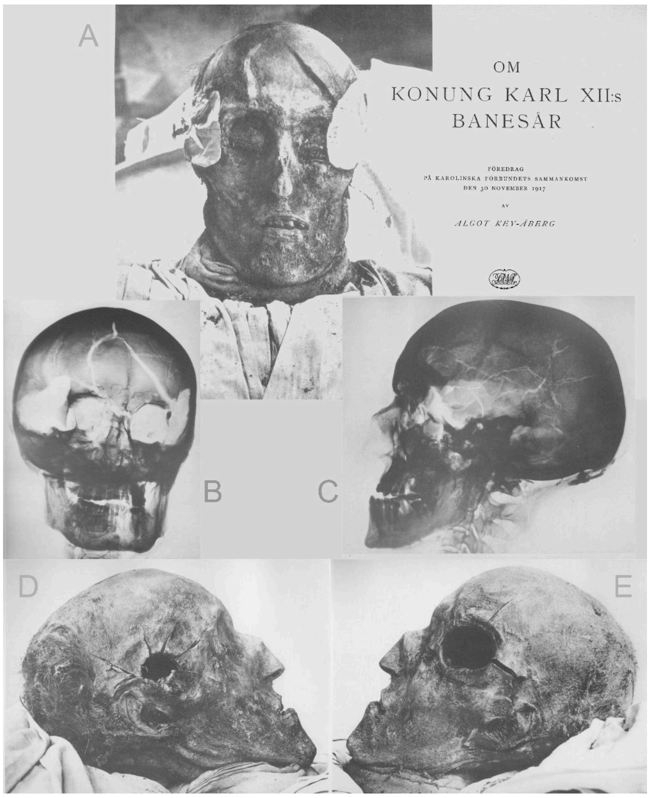

Figure5.2: Photographs and radiographs from the **1917** autopsy. A) Frontal view of the King's head with dressings still applied and the cover of the 1917 autopsy book, published in 1918. B) Radiograph of the King's head (frontal view). C) Radiograph of the left lateral portion of the partially reconstructed skull. D) Photographic image of the soft tissue wound on the right temple. E) Photographic image of the soft tissue wound on the left temple. Public domain images. Digitization available at: https://brf-portalen.se/wp-dragoner/album/k12-banesar/index.html

The 1917 autopsy, unlike the previous one which relied solely on manual illustrations, utilized technologies such as photographs and radiographs. This examination confirmed prior findings and expanded the analysis with additional data. Specialists observed that the King's death was instantaneous, caused by a single projectile. The entry point was located in the anterior part of the left temporal region, with the exit on the right, in the anterior half of the squamous part of the temporal bone. The projectile did not deviate, maintaining a straight trajectory slightly oriented toward the back, with no significant inclination relative to the horizontal plane. The projectile was proven to have a circular cross-section and a spherical shape, with an estimated diameter between 18 and 20 mm, allowing for a variation of one or two millimeters (16 to 22 mm). The examination provided no evidence that the shot was fired at close range. It was emphasized that the current shape of the lesion could not serve as a parameter for the original appearance of the opening, as it had been influenced by subsequent interventions, primarily the King's embalming process. It was concluded that the projectile transfixed the head with high kinetic energy [Key-Aberg_and_Stille_1918_e].

5.1.3 Subsequent Publications

Several books have been written about the case and, currently, two peer-reviewed articles stand out in their approach. One of them, published in *Forensic Science International* [Nordling_1998_e], addresses the general context, presenting a mosaic of research over time. The author, while indicating that the event could be a regicide, also provides data that limits this claim, such as the fact that Charles XII constantly exposed himself to enemy fire and, on the night of his passing, 22 other soldiers were also struck.

Another relevant study was published in 2022 in the journal *PNAS Nexus* [Junno_et_al_2022_e]. In this work, the authors concluded that the projectile could not have been made of lead nor possessed a diameter of 19.5 mm—corresponding to the mark on the felt hat worn by the monarch—but was instead a caliber exceeding 20 mm. The researchers mention that, at the time, iron canister shot measured 21.9 mm, indicating material and structural compatibility. To support these conclusions, ballistic tests were conducted on skulls filled with gelatin and on a folded piece of felt.

Curiously, the 1917 study also performed ballistic tests with a dry skull and another filled with gelatin and, as previously mentioned, already considered a potential diameter of 22 mm [Key-Aberg_and_Stille_1918_e], which accommodates the 21.9 mm cited in the modern study. Complementary information will be explored throughout the text in the Results and Discussion section.

5.1.4 Scope of the Present Study

The objective of the present study is to perform a forensic facial approximation that will provide a cranial structure closest to that of King Charles XII. Based on this, it aims to reconstruct/approximate the brain structure and local veins, thereby defining the trajectory of the projectile and the potentially injured regions.

Note: The analysis presented here adds to a series of other historical approaches related to facial approximation and anatomical analysis, all with a didactic purpose, aiming at the use of the *OrtogOnBlender* add-on and open-source software for technical collaborations that can reinforce previous studies or provide novel assessments.This collection includes the following studies: The Facial Approximation of a Battle of Gotland Victim (1361) [Moraes_et_al_2022_e], The Facial Approximation and Accident Dynamics of Phineas

Gage (1848) [Moraes_2023_e], The Facial Approximation and Structural Analysis of the Piltdown Man Skull - Fraud (1912) [Moraes_Bezzi_and_Bezzi_2024_e], The Facial Approximation of the "Vampire" of Venice (15th-17th Century) [Moraes_2024_e], The Forensic Facial Approximation of Seqenenre Tao II (c. 1558-1553 BC) [Moraes_and_Habicht_2024_e], The Facial Approximation of the Porsmose Man (c. 5500 BP) [Moraes_et_al_2025_e], and 3D Digital Analysis of the Anatoli Bugorski Case (1978) [Moraes_and_Moura_2025].

5.2 Materials and Methods

Forensic facial approximation is a technique that consists of generating a face from the morphological elements present in the skull. The present work followed the protocol described in detail in [Moraes_et_al_2024_e] and, complementarily, in [Moraes_et_al_2023_e]. For the data preparation, free and open-source software was used, such as the *OrtogOnBlender* add-on (https://www.ciceromoraes.com.br/doc/pt_br/OrtogOnBlender/index.html), which enables the Blender software (https://www.blender.org/) as a workstation suite for projects applied to health sciences, as well as Inkscape (https://inkscape.org/) and Gimp (https://www.gimp.org/) for generating graphics, refining, and editing images. All tools were executed on the Linux Ubuntu 24.04 operating system (https://ubuntu.com/). Anatomical terms were consulted in [Tank_and_Gest_2009_e].

As a 3D digitized skull of King Charles XII is unavailable, the solution found to obtain it consisted of cross-referencing data from the photographs and radiographs present in [Key-Aberg_and_Stille_1918_e], grouping all the necessary information—from the general limits of the skull and key measurements to the position of the lesions caused by the projectile (Fig. 5.3, A). This cranial reconstruction technique followed the approach presented in [Moraes_et_al_2024_e]. With the frontal and lateral images, it became possible to model a skull or adjust the anatomy of a virtual donor using the anatomical deformation technique. It was decided to import a donor head composed not only of the skull but also of the soft tissue (face), adjusting it so that the donor's bones were made compatible with the King's bone structure (Fig. 5.3, B). The resulting skull (Fig. 5.3, C) received soft tissue thickness markers based on a sample of modern European males, with an average BMI and an age range of 30–39 years [De_Greef_2006_e]. Complementarily, anatomical points were positioned to generate structural projections based on tomographic measurements of living individuals [Moraes_and_Suharschi_2022_e], which provide anatomical boundaries for lips, eyes, nasal wings, ears, and other structures (Fig. 5.3, D). A lateral projection of the nose was carried out,

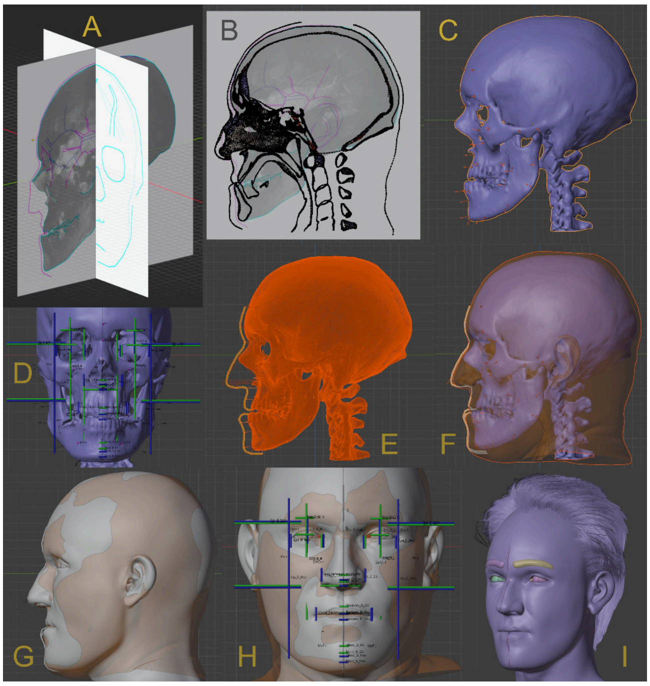

Figure5.3: A) Lateral and frontal projections of the skull. B) Anatomical deformation over the lateral projection. C) Resulting skull. D) Projection of anatomical structures. E) Soft tissue thickness markers and facial profile projection. F) Anatomical deformation and profile projection. G) Final bust mesh interpolating the generated data. H) Confluence of all data into a resulting face. I) Configured facial hair.

also based on tomographic data from living people [Moraes_and_Suharschi_2022_e], which allowed tracing the facial profile in conjunction with the tissue thickness markers (Fig. 5.3, E). A minor adjustment was required on the mandible, which was slightly open; when overlaying the result of the anatomical deformation and the profile projection, the data proved to be confluent (Fig. 5.3, F). A mesh corresponding to the final bust was generated through the interpolation of all facial projections (Fig. 5.3, G). In frontal view, the anatomical limitations of the face proved to be compatible with the statistical projections previously performed (Fig. 5.3, H). The bust was refined via digital sculpting, in addition to the configuration of facial hair, whose references were extracted from portraits of Charles XII (Fig. 5.3, I). The hair was adjusted based on a portrait of the King dating from 1717, in which hair loss is significant compared to portraits from his youth (see Fig. 5.7, E).

The bust received manual modeling of the clothing based on portraits of Charles XII and historical photography (https://commons.wikimedia.org/wiki/File:St%C3%B6vel_-_Livrustkammaren_-_8783.tif). Additionally, a cylinder of variable diameter, representing the potential projectile thicknesses, was modeled and adjusted to the lesions (Fig. 5.4, A). The skull received an overlay of anatomical information, such as the cerebral venous system (https://data.kitware.com/#collection/591086ee8d777f16d01e0724/folder/58a372e38d777f0721a64dc6) and the voxel data of a brain [Edlow_2019_e], properly adjusted to the endocranium (Fig. 5.4, B). A tricorne hat was imported

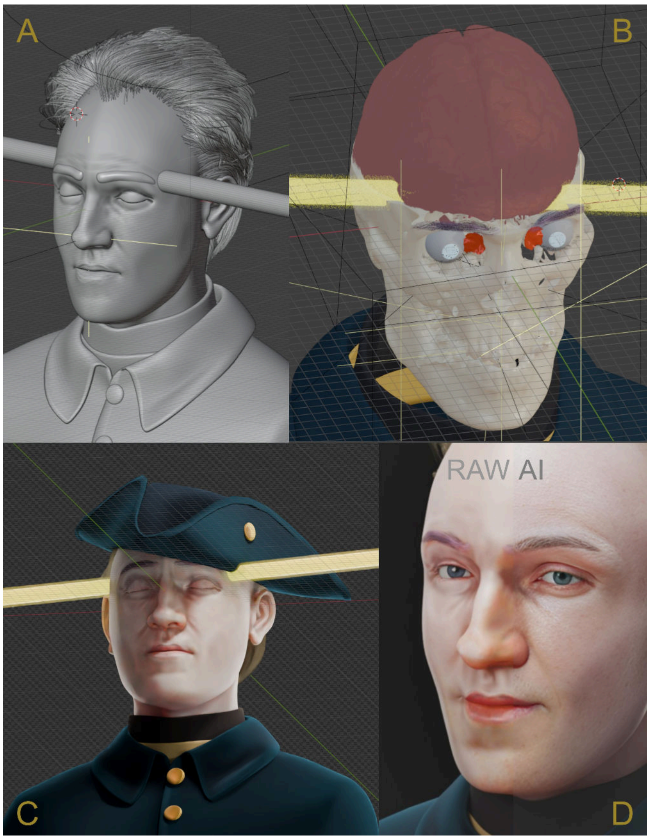

Figure5.4: A) Projectile tunnel crossing the final bust already with clothing. B) Adjusted brain voxel data. C) Rendering preview with the tricorne hat adjusted to the projectile entry. Raw rendering on the left and AI-enhanced adjustment on the right.

from a model available for download on the Sketchfab portal (https://sketchfab.com/3d-models/tricorn-hat-lowpoly-ac0ecde570ba49c9adecd0b6820a84c0), provided under a Creative Commons license by user Aarte. The structure was adjusted to conform to the King's head, strictly respecting the entry point of the projectile (Fig. 5.4, C). Only one image received localized treatment on the frontal portion of the face with detail enhancement via artificial intelligence, using a weight of 0.99 (on a scale of 0 to 1), ensuring high fidelity to the original and enriching the facial surface with fine details (Fig. 5.4, D). **All other images did not use AI technology**, and even the one that received such treatment underwent additional adjustments via image editing in Gimp.

Important: In the **Data Statement** section, video lessons detailing the aforementioned techniques—such as the projection of anatomical boundaries, nasal tracing, and anatomical deformation—will be made available. This content corroborates the references already available for download, in strict accordance with the open science approach adopted by the studies shared in *OrtogOnLineMag*. Such choices extend beyond mere rhetoric, as there are peer-reviewed publications that have employed the methodologies presented in the referred research, notably an article in Forensic Science International [Nasca_et_al_2026_e].

5.3 Results and Discussion


Figure5.5: Forensic facial approximation - final image.

The final image resulting from the facial approximation process contains objective elements derived from the skull and historical elements, along with subjective components from portraits, making it the only one to receive minimal retouching via AI (Fig. 5.5). The focus of the present work lies primarily on utilizing the final bust for the analysis of the projectile's trajectory; however, the methodological standard followed the same technical rigor applied to historical faces in artistic contexts and to the faces of crime victims in a forensic scope [Baldasso_et_al_2020_e].

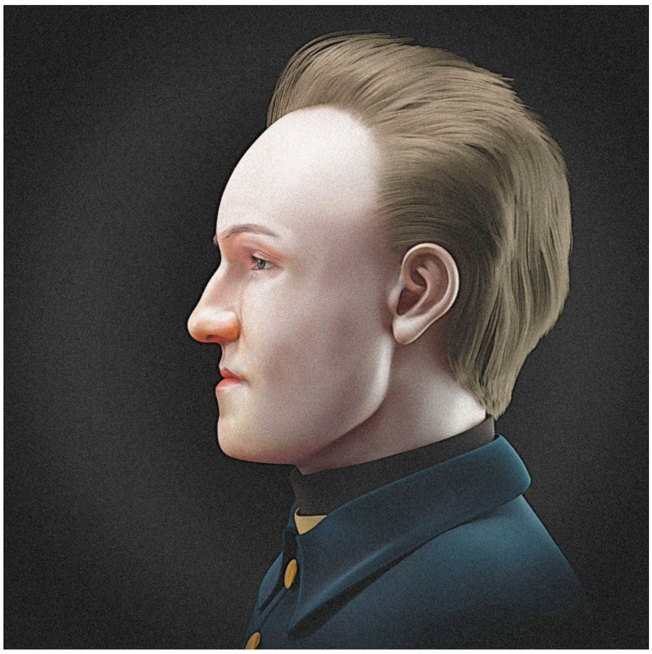
Figure5.6: Forensic facial approximation - profile view (with evident maxillary retrognathism and mandibular prognathism).

One aspect that immediately drew attention upon viewing the King's lateral radiograph was the characteristic of potential maxillary retrognathism associated with mandibular prognathism, which became evident in the profile view (Fig. 5.6).

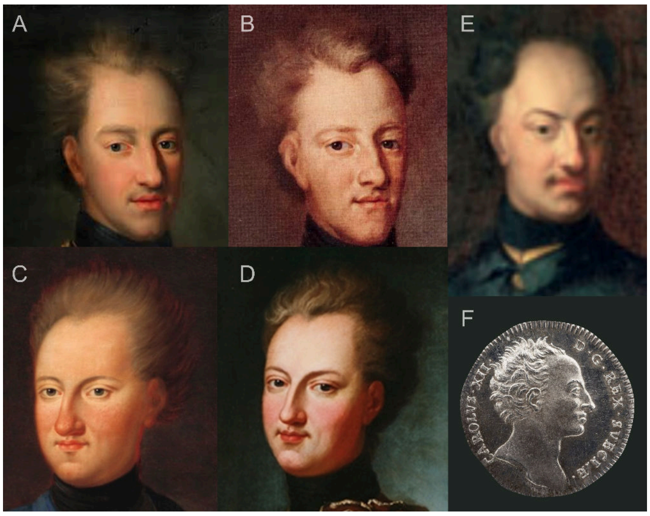

Figure5.7: A) Karl XII of Sweden. C.1700, Bema Knowledge (https://pt.wikipedia.org/wiki/Ficheiro:Karl_XII_of_Sweden._C.1700.jpg). B) Karl XII 1706 by David von Krafft (https://commons.wikimedia.org/wiki/File:Karl_XII_1706.jpg). C) Charles VII of Swedenby Axel Sparre (https://commons.wikimedia.org/wiki/File:Charles_VII_of_Sweden.jpg). D) Copy Charles XII - Nationalmuseum (https://en.wikipedia.org/wiki/File:Copy_Charles_XII_-_Nationalmuseum_-_17886.png). E) Karl XII i Lund by David von Krafft (https://commons.wikimedia.org/wiki/File:Karl_XII_i_Lund.jpg). F) Kastpenning med Karl XIIs profil, 1719, Miguel Herranz (https://commons.wikimedia.org/wiki/File:Kastpenning_med_Karl_XIIs_profil,_1719_-_Livrustkammaren_-_100562.tif).

These characteristics are also present in the portraits attributed to the King, whether those painted from life, copies, or even posthumous works. In addition to the characteristic hair and hairstyle, as well as the clothing replicated in this work, one can perceive a straight or slightly downward-slanting nose, a retracted supralabial region, and a projected lower lip, along with, occasionally, a prominent mentum (chin) (Fig. 5.7).

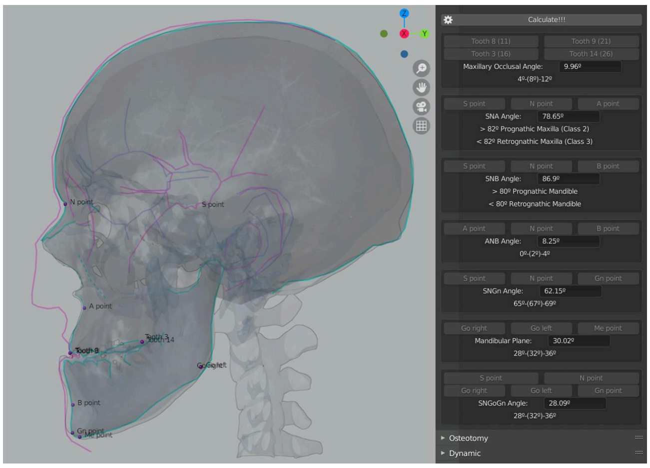

Figure5.8: USP Cephalometry in *OrtogOnBlender*.

To quantitatively evaluate the facial structure, a USP standard cephalometry [USP_2021_e] [Moraes_et_al_2023_e] was performed by positioning the relevant anatomical points (Fig. 5.8). The result was consistent with visual observations, as the SNA angle resulted in 78°40'—a value lower than 82°, which configures maxillary retrognathism (Class III). Furthermore, the SNB angle resulted in 86°54' with the mandible in the resting position (according to the radiograph) and 88°29' in occlusion; these values, being above 80°, configure mandibular prognathism.

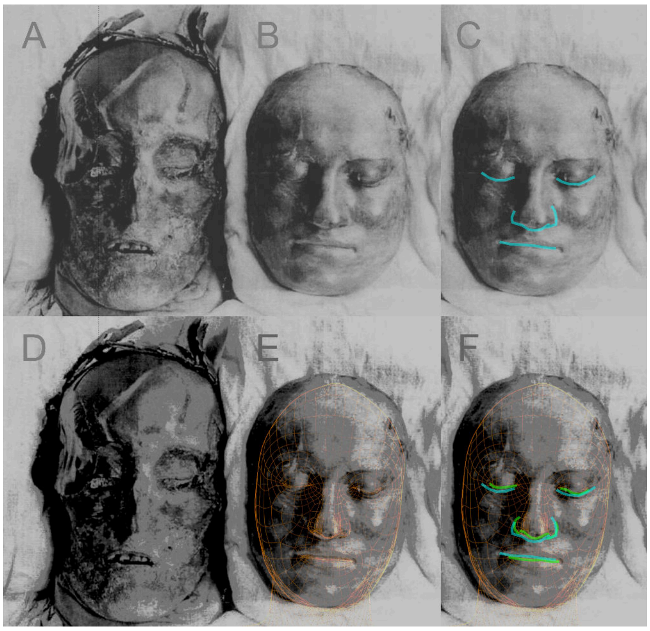

Figure5.9: Composition made from a photograph of King Charles XII's body alongside his death mask (1917). Otto Mattsson (https://commons.wikimedia.org/wiki/File:CharlesXII_mummy_with_Death_mask.jpg).

Although portraits maintain the general characteristics attributed to Charles XII, the heterogeneity of these representations raises questions regarding their fidelity to the actual face. One way to circumvent this limitation is through the analysis of life or death masks. In the present study, a death mask was analyzed, starting with a comparison to a frontal photograph capturing the monarch's body—already dehydrated after nearly 200 years—and his death mask laterally (Fig. 5.9, A and B). It is notable that the death mask presents a considerably robust face, not only in relation to the deceased body, which would be expected, but also when compared to the portraits. The method of the mask's fabrication was not evaluated; however, the process, due to the pressure exerted and the characteristics of the body's position and mandibular rotation, may have contributed to a slight deformation relative to the original, added to the trauma of death and the beginning of the natural decomposition process. Despite these variables, lines were traced at the corners of the eyes, nose, and mouth (Fig. 5.9, B) to compare them with the approximated face, which was overlaid in wireframe onto the photograph (Fig. 5.9, C). The subsequent comparison of the edges evidenced that the mask's nose was slightly more downward-inclined and the labial commissure line was somewhat higher (Fig. 5.9, D), alterations compatible with the aforementioned deformations.

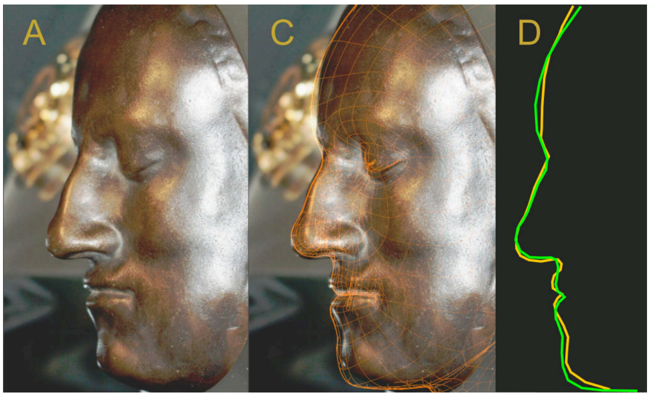

Figure5.10: A) Death mask in profile view. B) Overlay of the facial approximation. C) Comparison of the death mask's profile (in yellow) relative to the facial approximation (in cyan). Sven Rosborn (https://commons.wikimedia.org/wiki/File:Karl_XIIs_d%C3%B6dsmask.jpg).

A closer, higher-quality photograph of the death mask captured in profile (Fig. 5.10, A) allowed for a more precise overlay with the facial approximation (Fig. 5.10, B). The procedure reinforced the findings from the frontal view: although the eyes were compatible, as was the nose in general and the height of the lips, the mask's nose remains slightly more downward-inclined, while the lips are somewhat higher (Fig. 5.10, C). However, an evident feature is the projection effect of the upper lip—a common phenomenon in individuals with maxillary retrognathism during dental occlusion, where the labial mass is compressed, creating a projected appearance. This volume may indicate that the occlusion in the mask is more severe than that established in the cranial correction from the radiograph, a hypothesis supported by the difference in chin height, given that the chin of the facial approximation is positioned slightly below what is observed in the death mask. Nevertheless, due to the minor variation of the structures, the result is considered structurally satisfactory. The discrepancy in the forehead region could be indicative of various situations, ranging from local compression during the mask's molding to the projection of soft tissue on a skull structurally compromised by the multiple lesions caused by the projectile.

To trace the entry and exit of the projectile, the profile photographs from the 1917 exhumation with intact soft tissue were used as a reference (Fig. 5.2, D and E). As previously discussed, the specialists who performed the exhumation discarded the use of the skeletal lesion as a solid parameter for assessing the projectile's thickness [Key-Aberg_and_Stille_1918_e]; therefore, the tracing was adjusted based on the center of the two soft tissue wounds. This procedure proved consistent with previous approaches, although minor alignment discrepancies may occur due to the margin of error and the use of donor skulls as references, as observed in [Nordling_1998_e] (Figures 5 and 6) and in *KXII skalle rekonstrucktion av skottet* (https://commons.wikimedia.org/wiki/File:Avgjutning_av_KXIIs_skalle_m_rekonstruktion_av_skottet_-_Livrustkammaren_-_27057.tif); in both cases involving a surrogate skull. The entry was observed between the greater wing of the sphenoid and the frontal process on the left side, with the exit through the right squamous part (Fig. 5.11, A). Using the parameters from the [Key-Aberg_and_Stille_1918_e] study, which stipulated a projectile with a diameter between 18 and 20 mm, with a margin of error of ±1 mm and ±2 mm, a tunnel was created with thicknesses of 16, 17, 18-20, 21, and 22 mm to encompass this data (Fig. 5.11, B). A virtual donor brain was adjusted to fit Charles XII's endocranium, allowing for the observation of the affected regions (Fig. 5.11, C and D). From the left side, the tunnel hits the orbital part of the frontal lobe and involves the anterior portion of the right frontal lobe (Fig. 5.11, E and F).

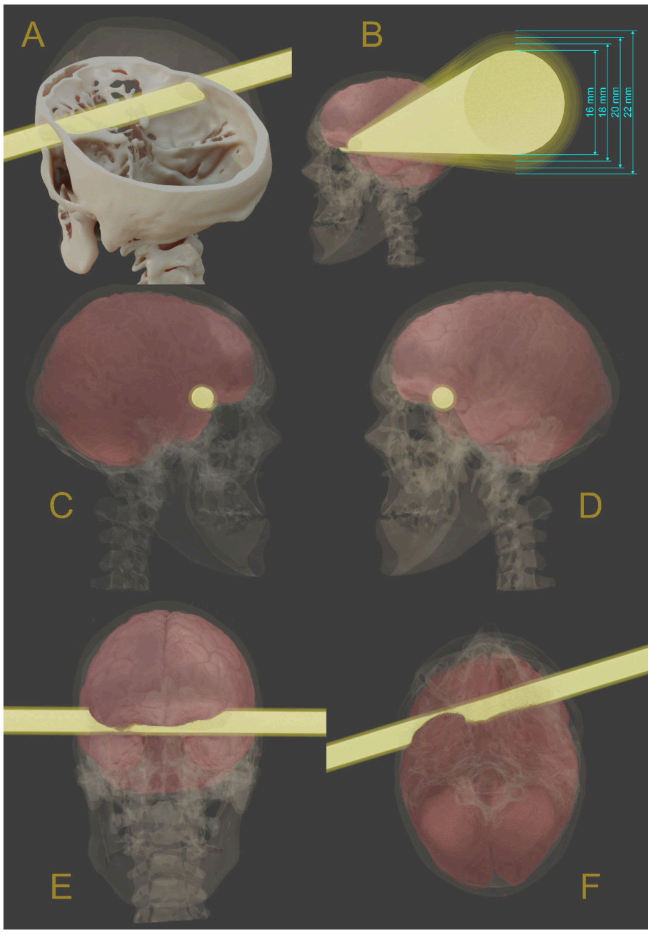

Figure5.11: A) Projectile path through the skull. B) Diameters encompassing the 1917 analysis. C) Visualization of the right side based on the projectile's rotation. D) Visualization of the left side based on the projectile's rotation. E) Frontal view of the projectile's passage. F) Inferior view of the projectile's passage.

One of the most intriguing features of Charles XII's cranial lesions, widely documented in the 1917 exhumation report, is the presence of a large entry defect on the left side of the head, contrasting with a significantly smaller exit hole on the right. This pattern, the inverse of what is commonly observed in modern high-velocity projectile wounds, can cause confusion for readers accustomed to media representations of ballistic injuries. In contemporary projectiles—generally faster, smaller, and with greater gyroscopic stability—the exit wound is usually larger due to tumbling and higher energy transfer at the end of the trajectory [Kimmerle_and_Baraybar_e]. However, in the case of early 18th-century musket balls—bulky projectiles (approximately 18–22 mm) made of almost pure lead (or other metal) and fired at low velocities (typically between 200–400 m/s)—the behavior is different: the projectile tends to deform and flatten upon impacting the cortical bone at entry, creating a larger hole, while at the exit, already decelerated and deformed, it produces a smaller and more irregular defect. Recent ballistic experiments [Junno_et_al_2022_e] successfully reproduced this pattern by using projectiles similar to those available in 1718, reinforcing the forensic coherence of the 1917 observations, whose specialists also conducted such tests [Key-Aberg_and_Stille_1918_e].

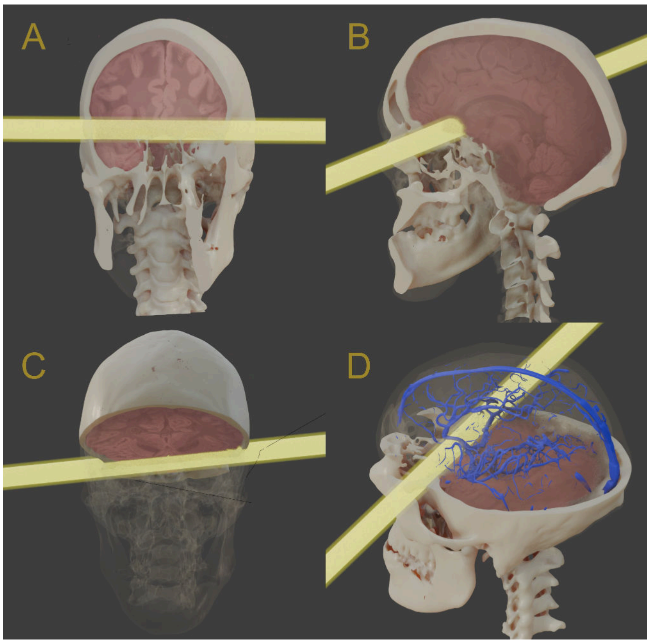

Figure5.12: Brain voxel data slices: A) Frontal view. B) Lateral view. C) Slightly inferior view. D) Superior view with the addition of cerebral veins.

When observed internally, it is evident that the trajectory transfixed the frontal and temporal lobes, potentially striking the olfactory tract and bulb (Fig. 5.12, A), the corpus callosum, and the septum pellucidum (Fig. 5.12, B and C). By reconstructing the vascular network of the region, it is observed that the projectile could have hit, among other structures, the middle cerebral artery (Fig. 5.12, D).

Although the 1917 exhumation did not attribute significant relevance to the felt hat, explicitly treating it as a secondary element—as indicated by the observation that “nor was there found inside the skull any fragment of the hat that the King supposedly wore at the time of his death” [Key-Aberg_and_Stille_1918_e]—this isolated mention ended up being disproportionately valued by later authors, who began to use it as an evidential anchor. This interpretive shift is problematic, as Key-

Figure5.13: Frontal and slightly inferior view with full attire and projectile passage.

Åberg’s own report not only avoids employing the hat as a ballistic variable but also bases its conclusions exclusively on the physical marks observed on the skull. Even so, recent works, such as Junno et al. (2022), state that “the projectile that killed Charles also pierced his felt hat leaving a hole of 19 to 19.5 mm in diameter” [Junno_et_al_2022_e], implicitly attributing this measurement to the primary 1917 source, which finds no support in the original text that never associates such a value with the textile artifact. This type of claim suggests a mediated chain of citation, possibly derived from interpretations like that of Nordling (1998), in which the hat had already been unduly elevated to a central element [Nordling_1998_e]. The result is a methodological inversion: an artifact not geometrically validated in relation to the skull begins to define ballistic parameters, while the direct evidence—more robust and explicitly prioritized in the 1917 examination—is relativized or reinterpreted in light of this premise. Furthermore, it remains notable that none of these studies performed the minimum verification necessary to sustain such use of the hat—that is, the spatial and angular correspondence between the hole in the felt and the documented intracranial trajectory—which reinforces the speculative nature of this interpretive line and highlights a persistent methodological gap in the literature.

Precisely considering this gap, the present study positioned the piece as it might have been arranged at the moment of the potential impact (Fig. 5.13). Although it may appear displaced and excessively close to the eyes, wearing the tricorne hat in this manner finds support in artistic references from the 18th century (https://en.wikipedia.org/wiki/File:Frederic_II_de_prusse.jpg, https://commons.wikimedia.org/wiki/File:Tricorne_18th_century.jpg), 19th century (https://commons.wikimedia.org/wiki/File:Edmund_Fan ning_colonial_administrator.jpg, https://commons.wikimedia.org/wiki/File:Fredrik_den_store._Efter_ett_tr%C3%A4snitt_af_B%C3%BCrkner.jpg), and 20th century (https://en.wikipedia.org/wiki/File:US_Army_52416_The_American_Soldier,_1781.jpg).

Figure5.14: Images of the bust with the projectile trajectory in versions without and with the felt hat.

A series of images was rendered to illustrate the entry and exit of the projectile on the approximated bust of King Charles XII, serving as a didactic element closely representing what occurred, both in an anatomical context and in relation to the clothing (Fig. 5.14).

5.4 Conclusion

The present study successfully fulfills the objective of performing an unprecedented forensic facial approximation of Charles XII of Sweden, integrating biomechanical and three-dimensional craniometric analyses within an open-source digital environment. Based on the methodology employed, it was possible to reach significant conclusions that enrich the literature and the historical debate surrounding the monarch.

Firstly, the three-dimensional geometric reconstruction of the projectile trajectory robustly corroborated the fundamental observations presented in the historical report of the 1917 exhumation. The digital alignment, based on the center of the wounds identified in the soft tissues, confirmed a practically rectilinear transfixing trajectory, with a nearly horizontal orientation slightly directed toward the rear.

As the main diagnostic novelty, the execution of the USP standard cephalometric analysis revealed, in a quantitative manner, structural characteristics that until now had been approached in a purely descriptive or artistic way. This provided solid craniometric evidence that the King presented a condition of maxillary retrognathism (Class III) associated with mandibular prognathism. Such anatomical findings justify and geometrically validate the facial proportions observed in portraits painted from life and the volumetric characteristics recorded in his death mask, such as the accentuated projection of the labial mass during occlusion.

Furthermore, the work innovates by presenting the first complete three-dimensional anatomical approximation of the skull, brain, and intracranial venous system of Charles XII. This approach allowed not only for the visualization of the monarch's approximated face with high technical rigor but also for the mapping, with significant precision, of the encephalic and vascular structures severely injured by the impact, such as the frontal and temporal lobes, the corpus callosum, and the middle cerebral artery.

Finally, filling a persistent methodological gap in contemporary literature, the study performed the spatial verification of the royal attire. The precise three-dimensional positioning of the tricorne hat—adjusted in accordance with historical and iconographic references of military use at the time—demonstrated exact geometric compatibility with the projectile's entry trajectory in the left temporal region.

In summary, the use of the *OrtogOnBlender* ecosystem and open-source tools proved to be an efficient and highly reproducible methodology for the fields of bioarchaeology and digital forensic science, offering an unprecedented technical assessment that consolidates the integrity of historical data from a strictly geometric and biomechanical perspective.

5.5 Data Statement

- Projections of anatomical boundaries (Part 1)[63]
- Projections of anatomical boundaries (Part 2)[64]
- Nasal projection techniques[65]
- Anatomical deformation[66]
- Hair adjustment (demonstration at 2m36s)[67]

[63] https://youtu.be/U6oYkEmfyWo
[64] https://youtu.be/Vcz2e5uSFX8
[65] https://youtu.be/F205kLQ--Oo
[66] https://youtu.be/xig5_EcIFWA
[67] https://commons.wikimedia.org/wiki/File:D._Pedro_I_-_Processo_da_reconstru%C3%A7%C3%A3o_facial_forense.webm

5.6 Acknowledgements

To Dr. Richard Gravalos for providing the tomography of the virtual donor.

5.7 References

[Baldasso_et_al_2020_e] Baldasso, R. P., Moraes, C., Gallardo, E., Stumvoll, M. B., Crespo, K. C., Strapasson, R. A. P., & de Oliveira, R. N. (2020). 3D forensic facial approximation: Implementation protocol in a forensic activity. In Journal of Forensic Sciences (Vol. 66, Issue 1, pp. 383–388). Wiley. https://doi.org/10.1111/1556-4029.14587

[De_Greef_2006_e] De Greef, S., Claes, P., Vandermeulen, D., Mollemans, W., Suetens, P., & Willems, G. (2006). Large-scale in-vivo Caucasian facial soft tissue thickness database for craniofacial reconstruction. In Forensic Science International (Vol. 159, pp. S126–S146). Elsevier BV. https://doi.org/10.1016/j.forsciint.2006.02.034

[Edlow_2019_e] Edlow, B. L., Mareyam, A., Horn, A., Polimeni, J. R., Witzel, T., Tisdall, M. D., Augustinack, J., Stockmann, J. P., Diamond, B. R., Stevens, A., Tirrell, L. S., Folkerth, R. D., Wald, L. L., Fischl, B., & van der Kouwe, A. (2019). 7 Tesla MRI of the ex vivo human brain at 100 micron resolution. Cold Spring Harbor Laboratory. https://doi.org/10.1101/649822

[Hatton_and_Nordlund_2026_e] Hatton, R.M., Nordlund, S. (2026, March 9). Charles XII. Encyclopedia Britannica. https://www.britannica.com/biography/Charles-XII

[Junno_et_al_2022_e] Junno, J.-A., Niskanen, M., Maijanen, H., Niinimäki, J., Junno, A., & Oura, P. (2022). The death of King Charles XII of Sweden revisited. PNAS Nexus, 1(5). https://doi.org/10.1093/pnasnexus/pgac234

[Key-Aberg_and_Stille_1918_e] Key-Åberg, A., & Stille, A. (1918). Konung Karl XII:s banesår: 1917 års undersökning och i samband därmed gjorda iakttagelser. P. A. Norstedt & Söners förlag. Recuperado de https://brf-portalen.se/wp-dragoner/album/k12-banesar/index.html

[Kimmerle_and_Baraybar_e] Kimmerle, E. H., & Baraybar, J. P. (2017). Lesões por Arma de Fogo. In E. H. Kimmerle & J. P. Baraybar, Trauma Esquelético: Identificação de Lesões Ocasionadas por Violação aos Direitos Humanos e Conflitos Armados (pp. 283–464). Editora Unifesp.

[Moraes_2023_e] Moraes, C. (2023). A Aproximação Facial e a Dinâmica do Acidente de Phineas Gage (1848). figshare. https://doi.org/10.6084/M9.FIGSHARE.24782022

[Moraes_2024_e] Moraes, C. (2024). A Aproximação Facial da “Vampira” de Veneza (Séc. XVI-XVII). figshare. https://doi.org/10.6084/M9.FIGSHARE.25447270

[Moraes_Bezzi_and_Bezzi_2024_e] Moraes, C., Bezzi, L., & Bezzi, A. (2024). A Aproximação Facial e a Análise Estrutural do Crânio do Homem de Piltdown - Fraude (1912). figshare. https://doi.org/10.6084/M9.FIGSHARE.24937035

[Moraes_and_Habicht_2024_e] Moraes, C., & Habicht, M. (2024). A Aproximação Facial Forense de Seqenenre-Taa-II (c. 1558-1553 a.C). figshare. https://doi.org/10.6084/M9.FIGSHARE.25945906

[Moraes_and_Moura_2025] Moraes, C., & Moura, L. (2025). 3D Digital Analysis of the Anatoli Bugorski Case (1978). figshare. https://doi.org/10.6084/M9.FIGSHARE.29973373

[Moraes_and_Suharschi_2022_e] Moraes, C., & Suharschi, I. (2022). Mensuração de Dados Faciais Ortográficos em Moldavos e Comparação com Outras Populações. figshare. https://doi.org/10.6084/M9.FIGSHARE.20089754. https://ortogonline.com/doc/pt_br/OrtogOnLineMag/4/Moldavos.html

[Moraes_et_al_2022_e] Moraes, C., Beaini, T. L., Steffensen, T. H., & Dalstra, M. (2022). A Aproximação Facial de uma Vítima da Batalha de Gotland (1361). Figshare. https://doi.org/10.6084/M9.FIGSHARE.21432384

[Moraes_et_al_2023_e] Moraes, C., Habicht, M. E., Galassi, F. M., Varotto, E., & Beaini, T. (2023). Pharaoh Tutankhamun: a novel 3D digital facial approximation. Italian Journal of Anatomy and Embryology, 127(1), 13–22. https://doi.org/10.36253/ijae-14514

[Moraes_et_al_2024_e] Moraes, C., Habicht, M. E., Artico, M., Forte, F., Varotto, E., & Galassi, F. M. (2024). The mummy of Pharaoh Amenhotep III (reigned ca. 1388–1351 BC) and its facial approximation: An anatomical approach. Clinical Anatomy, 38(2), 211–215. https://doi.org/10.1002/ca.24251

[Moraes_et_al_2025_e] Moraes, C., Moura, L., Beaini, T. L., & Paiva Curi, J. (2025). A Aproximação Facial do Homem de Porsmose (ca. 5500 AP) [Dataset]. figshare. https://doi.org/10.6084/M9.FIGSHARE.28207625

[Nasca_et_al_2026_e] Nasca, G., Ioime, G., Pellegrini, A., Ianora, A. A. S., Introna, F., Di Gioia, E., & Galantucci, L. M. (2026). A novel forensic protocol for age reversal facial approximation from elderly skulls using computed tomography scans, CAD techniques and anthropometric data. Forensic Science International, 385, 112960. https://doi.org/10.1016/j.forsciint.2026.112960

[Nordling_1998_e] Nordling, C. O. (1998). The death of King Charles XII — The forensic verdict. Forensic Science International, 96(2–3), 75–89. https://doi.org/10.1016/s0379-0738(98)00110-8

[Tank_and_Gest_2009_e] Tank, P. W., & Gest, T. R. (2009). Atlas de anatomia humana (A. L. Werneck & H. Werneck, Trads.; 1ª ed.). Artmed.

[USP_2021_e] Universidade de São Paulo. (2021). Análise cefalométrica simplificada. e-Disciplinas USP. https://web.archive.org/web/20230610023749/edisciplinas.usp.br/pluginfile.php/5214352/mod_resource/content/2/Estudo%204.pdf

Chapter 6

Expansion and Automation of the Unified Import System for Composite Skulls in OrtogOnBlender XP

Cicero Moraes | Google Scholar[68], ResearchGate[69], ORCID[70], Homepage.[71]

3D Designer, Arc-Team Brazil, Sinop-MT, Brazil - Bachelor's degree in Marketing, Dr. h. c. FATELL/FUNCAR (Brazil) and CEGECIS (Mexico) - Member of Sigma Xi, Mensa Brazil, Poetic Genius Society, and International Society for the Study of Creativity and Innovation (ISSCI) - Invited reviewer: Elsevier, Springer Nature, PLoS, and LWW - Guinness World Records 2022: First 3D-printed tortoise shell.

Richard Gravalos | Lattes[72]

Dental Surgeon, Specialist in Oral and Maxillofacial Surgery and Traumatology, Specialist in Orthodontics, Specialist in Public Health/Family Health, São Paulo - SP.

William Tadeu Ferreira Sanchis | Lattes[73]

Oral and Maxillofacial Trauma Surgeon, Hospital CEMA, São Paulo - SP.

Rodrigo Dornelles | Google Scholar[74], ResearchGate[75]

Plastic Surgeon, Núcleo de Plástica Avançada - NPA, São Paulo-SP.

Everton da Rosa | ResearchGate[76]

Dental Surgeon, Everface Odontologia Especializada, Brasília-DF, Brazil.

Publication date: July 15, 2026
ISSN: **2764-9466** (Vol. 7, No. 2, 2026)
DOI: 10.6084/m9.figshare.32899760

Abstract

This study addresses the expansion and automation of the unified composite skull import system within the free software OrtogOnBlender XP, focusing on orthognathic surgery planning and maxillofacial procedures. The primary objective of the work was to overcome structural limitations of previous versions by implementing a redundant modular architecture to mitigate critical scale and mirroring errors. Among the most important and interesting findings, a stark disparity was observed between the new artificial intelligence-driven pipeline (TotalSegmentator + MeshSegNet) and the legacy tool DentalSegmentator. The new workflow proved to be approximately 22 times more accurate than the old one, achieving a global accuracy per patient of 95.65% against a mere 4.35% for the previous method, while also processing data in half the time (~10 minutes versus ~20 minutes). Comparative tests between operating systems also revealed crucial performance and structural data. In a first raw execution, the automated alignment of intraoral models achieved ~93% accuracy under Linux and ~86% under Windows. After coding fine-tuning, the success rate jumped to the impressive benchmarks of 97.83% under Linux and 93.18% under Windows. However, under a global evaluation per patient, Linux proved to be about 3 times more effective against residual failures, presenting only 1 error across 23 exams (~95% success rate), compared to 3 failures out of 22 exams under Windows. The study concludes that while automation drastically reduces active working time, visual human validation remains an indispensable layer of security in the digital planning workflow.

Keywords: *Composite skulls, OrtogOnBlender XP, Artificial intelligence, TotalSegmentator, MeshSegNet, Intraoral scan alignment, Open-source surgical planning*

[68] https://scholar.google.com.br/citations?user=u33uvHUAAAAJ
[69] https://www.researchgate.net/profile/Cicero-Moraes
[70] https://orcid.org/0000-0002-9479-0028
[71] http://www.ciceromoraes.com.br
[72] http://lattes.cnpq.br/5580397716843783
[73] http://lattes.cnpq.br/2497024814105153
[74] https://scholar.google.com/citations?user=ZNqVhQYAAAAJ&hl=pt-BR
[75] https://www.researchgate.net/profile/Rodrigo-Dornelles
[76] https://www.researchgate.net/profile/Everton-Rosa

6.1 Introduction

Launched in 2017, OrtogOnBlender (OOB) has evolved over the years from a study tool into a surgical planning tool de facto utilized by surgeons across 37 countries and widely published in peer-reviewed journals, addressing not only, but primarily, procedures within the human facial region.

A year ago, the first version of the unified import system for composite skulls was implemented [Moraes_et_al_2025_f]. To ensure this milestone is preserved over time, it is important to explain the challenges of that period and how this approach represented major progress.

In the early days of OOB development in 2017, the primary challenge was converting DICOM files into 3D objects—moving from a sequence of images (voxel data) to a 3D mesh. This was achieved using DicomToMesh (https://github.com/eidelen/DicomToMesh) via a primitive interface inside Blender, where the user specified the tomography directory and the Hounsfield scale factors to be reconstructed. Initially, the data-filling process was manual[77], but an automated approach based on a tomograph database was later implemented [Moraes_et_al_2021_f]. Although it was a well-developed tool, implementing DicomToMesh across different operating systems via OOB caused compatibility issues, prompting the transition to a Python-based solution (VTK+SimpleITK), which required significantly less effort for system porting [Moraes_et_al_2021b_f].

These tools represented a breakthrough by centralizing the workflow within a single software package, eliminating the need for external applications such as InVesalius (https://invesalius.github.io/) or Slicer (https://www.slicer.org/), although OOB has maintained a script-level connection with the latter to this day. Nonetheless, even with these advances, the segmentation phase still demanded significant knowledge and effort from the user. Initially, an anatomical landmark-based mandibular segmentation tool was developed[78]; while it functioned in a significant percentage of cases, it presented structural boundary limitations (often over-segmenting) and required manual placement of landmarks, which could serve beginner users but was ignored by advanced ones who opted for manual segmentation, judging it more practical.

For replacing tomography teeth with intraoral scans (IOS), the process was simpler and more practical. Given that tomography segmentation occurred in three stages—the face, the skull, and the teeth (the densest part of the bone)—a lateral clipping tool was implemented so users could manually isolate the dental region for subsequent IOS alignment[79].

Porting external tools like computed tomography reconstruction and implementing specific commands using the Blender Python API (bpy) represented a major evolution and simplification of the surgical planning process. Although much of it still required manual user intervention, it became possible to develop a complete orthognathic surgery planning protocol within a single graphical interface based on free and open-source software [Moraes_et_al_2020_f].

In addition to anatomical reconstruction, cephalometry—including both Arnett and USP analyses[80]—has been a core feature of OOB for several years. Facial structure projection for both soft tissue and the face is a native OOB solution that was published in a peer-reviewed journal [Abdullah_et_al_2022_f], received data updates from diverse populations [Moraes_and_Suharschi_2022_f], and was ultimately converted into a standard tool within the add-on.

Regarding artificial intelligence, the first tool developed focused on tooth segmentation in IOS models using MeshSegNet (https://github.com/Tai-Hsien/MeshSegNet), which was incorporated into the core of OOB [Moraes_and_Dakir_2021_f]. Subsequently, a multiple-component solution was tested, which aligned the tomography to the Frankfurt plane, positioned a series of anatomical landmarks, and automatically segmented various anatomical structures, such as the mandible and airways. Although highly dependent on Slicer, the tool was executed directly through OOB by simply indicating the storage directory of the DICOM files [Moraes_et_al_2024_f].

With the advent of OrtogOnBlender XP, built upon Blender 4.2, the tomography import system received user interface improvements and underwent a rigorous testing pipeline involving more than 400 tomographies, increasing its success rate from 96.78% to 100% [Moraes_et_al_2024b_f]. Immediately following this, an AI-driven tomography segmentation system was developed as a complementary and redundant layer to the previously created automatic framework. A new round of testing involved 151 tomographies with a 100% success rate [Moraes_et_al_2024c_f].

These two tools enabled the development of the unified composite skull system, allowing users to automatically import the tomography, perform AI-based segmentation, position a series of anatomical landmarks, and import and pre-align intraoral models. During this phase, 120 tests were performed on the unified system (excluding dental alignment), followed by 36 complete tests—12 within each operating system configuration (Linux,

[77] https://www.ciceromoraes.com.br/doc/pt_br/OrtogOnBlender/OrtogOnBlender_Como_Funciona.html?highlight=mand%C3%ADbula#manual

[78] https://www.ciceromoraes.com.br/doc/pt_br/OrtogOnBlender/OrtogOnBlender_Como_Funciona.html?highlight=mand%C3%ADbula#teeth-touched

[79] https://www.ciceromoraes.com.br/doc/pt_br/OrtogOnBlender/Protocolo_Planejamento_Ortognatica.html#preparo-e-uniao-dos-dentes-alinhados-ao-cranio

[80] https://www.ciceromoraes.com.br/doc/pt_br/OrtogOnBlender/OrtogOnBlender_Como_Funciona.html?highlight=usp#cephalometry

WSL, and Windows)—revealing a slight performance advantage for Linux [Moraes_et_al_2025_f]. In total, prior to the writing of this document, OOB XP had already accumulated 1,028 tool tests.

Although the unified system presented a major advancement, it still had structural limitations, such as the lack of individual tooth segmentation, an intraoral model alignment without guaranteed precision adjustment, an absence of anatomical measurement data, and a lack of pre-configured cephalometry tools.

6.2 The Framework Update

The unified composite skull generation system in OOB XP received some adjustments and optimizations without altering its previous core functionality, merely adapting the code to accommodate new technology insertions. This, in turn, generated a positive framework of complementary workflow options, enriching the add-on and granting the user greater flexibility and alternatives should any specific tool encounter an issue.

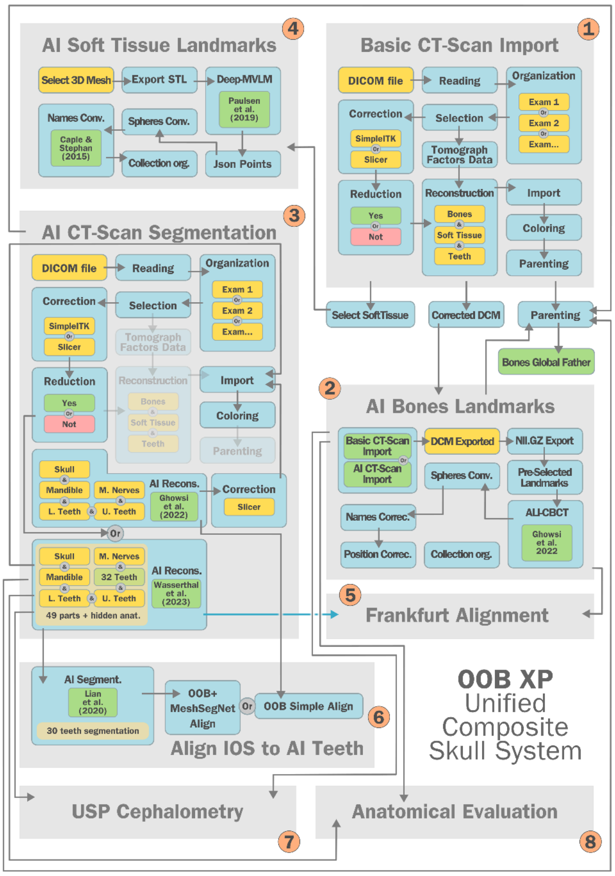

Figure6.1: Visual scheme of the unified composite skull generation system.

The current configuration of the system operates as follows:

0) The user specifies the directories containing the computed tomography scan files and the upper and lower scanned intraoral models (IOS).

1) A 3D reconstruction of the tomography is performed using the raw DICOM data based on the tomograph model database, outputting three distinct meshes: Bones, SoftTissue, and Teeth. The Bones mesh acts as the root in the parenting hierarchy, a structure reflected throughout subsequent processes; thus, the Bones mesh serves as the global standard of reference. This approach was chosen due to its historical reliability established through extensive testing and practical clinical use, making it the most robust tool developed among the others. Furthermore, keeping the primary structure intact provides an extra pre-operative reference, and the SoftTissue mesh—in the absence of an external photogrammetry scan—serves as the baseline for anatomical landmark placement and osteotomy-driven structural adjustments (Fig. 6.1, 1).

2) Next, the automated bone anatomical landmark positioning system via artificial intelligence is triggered. This system is fully independent and provides the necessary data to align the head to the Frankfurt plane, while offering references for the initial automatic positioning of osteotomies. It subsequently helps limit the zones of influence for facial adjustments during osteotomies, as well as assisting in facial measurements and cephalometric analysis (Fig. 6.1, 2).

3) Significant improvements were introduced in this phase, as the previous version already provided an anatomical segmentation, but practical usage tests revealed that the results on Windows were slightly inferior to those on Linux, processing times could extend excessively, and the system lacked individual tooth segmentation—a frequent user request. To address this, a system based on TotalSegmentator (https://github.com/wasserth/totalsegmentator) was implemented, building upon the work of [Wasserthal_et_al_2023_f]. When compared directly to the DentalSegmentator, this new pipeline reduced processing time by practically half, while delivering a significantly larger number of segmented anatomical pieces. This code integration enabled significant improvements in the IOS alignment system, as the software now computes teeth individually and works in tandem with MeshSegNet. It also provides complementary data for the Frankfurt alignment, as will be seen below (Fig. 6.1, 3). The detailed data regarding this time and accuracy comparison are presented later in the Testing and Best Practices section.

4) The SoftTissue mesh, which in practice is the "face", receives a series of automated anatomical landmarks via artificial intelligence. These points provide spatial references for several subsequent approaches, such as boundary mapping for osteotomy influence zones, facial measurements, and cephalometric plotting (Arnett) (Fig. 6.1, 4).

5) OOB XP utilizes the anatomical landmark data generated primarily by Step 2 and complementarily by Step 3 to align the head along the Frankfurt plane. While not a unanimous choice among specialists—as some prefer the natural head position—it remains a widely doc-

umented and utilized orientation standard (Fig. 6.1, 5).

6) Another major upgrade occurs at this stage. The previous version (OOB Simple Align) provided a preliminary IOS alignment with a success rate of ~5% (only 1 in 20 cases resulted in full alignment). The new version inverted the logic and substantially improved system reliability; now, only 1 in 15 cases on Windows, or 1 in 46 on Linux, may present an alignment issue, boosting the success rate to a milestone of 93.18%–97.83%. This breakthrough was achieved by adapting MeshSegNet to the current Python version, cross-referencing data with anatomical landmarks derived from TotalSegmentator meshes, and implementing complementary programming within OOB itself (Fig. 6.1, 6). The cited numbers will be explained later in Tests and Best Practices.

7) The USP cephalometry system was successfully ported from OOB 2.9.1 to OOB XP. However, since anatomical landmarks are now positioned automatically, the current version generates a report immediately following the finalization of the unified composite skull generation process (Fig. 6.1, 7). Arnett cephalometry is also currently being ported.

8) The final stage consists of gathering anatomical measurements based on both population means and calculated proportions. This step also generates a color-coded statistical report of the results based on standard deviations (Fig. 6.1, 8).

6.3 How It Works

In the following sequence, a step-by-step guide will be provided for generating a composite skull using the most current approach of the tool.

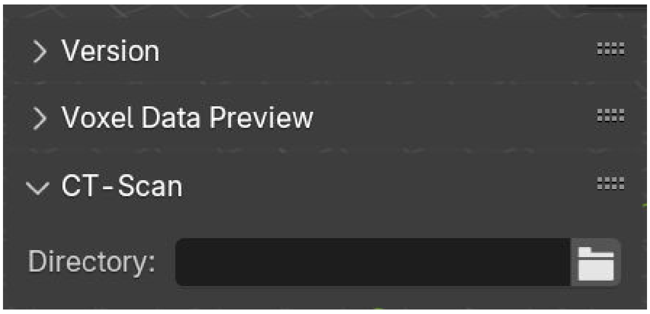

Figure6.2: CT-Scan section.

Initially, it is necessary to expand the CT-Scan section of OOB XP (available starting from version 2026-06-29). There, the directory selection must be performed. To do so, simply click on the directory icon at the bottom right (Fig. 6.2).

The next step consists of entering the root directory of the computed tomography scan. There is no need to select one of multiple folders, as OOB features a tomographic exam organization tool. That is, once in the root directory, simply click on **Accept** (Fig. 6.3).

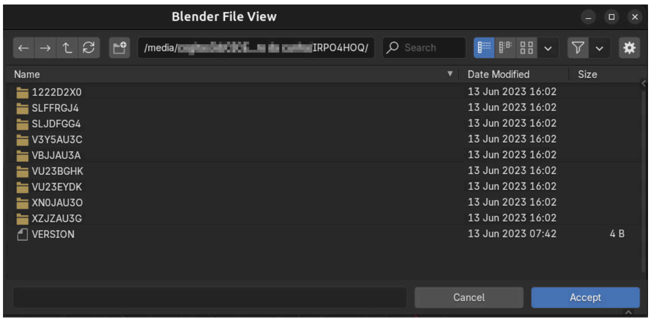

Figure6.3: Selection of the computed tomography root directory.

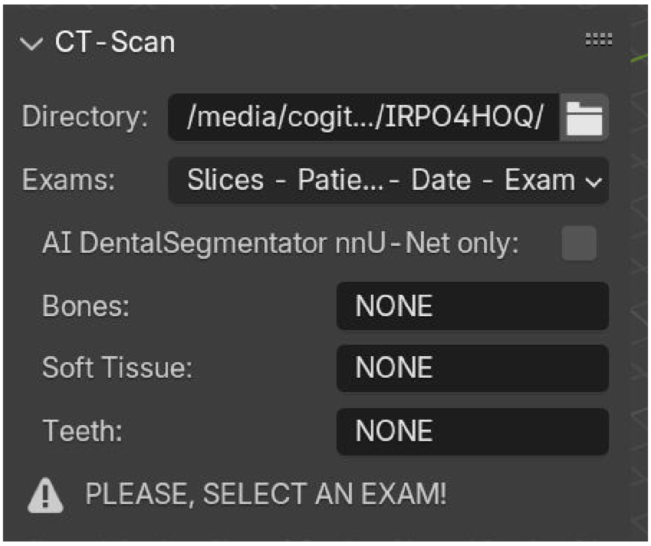

Figure6.4: Exam selector activated.

Once this is done, the exam selector is activated in **Exams** (Fig. 6.4).

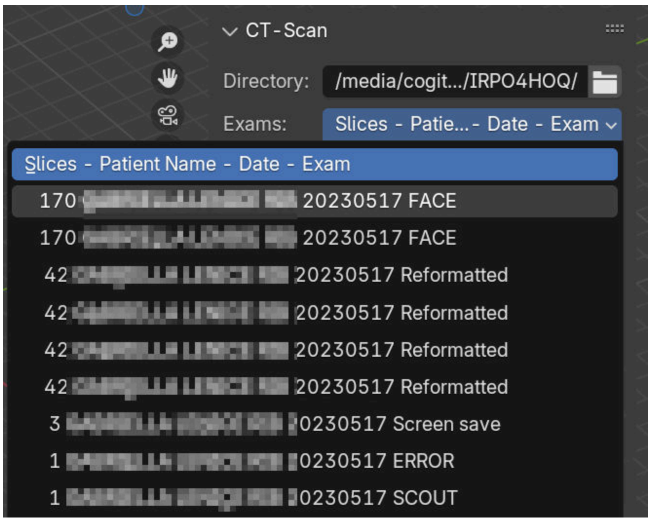

Figure6.5: Selection of the exam to be reconstructed in 3D.

By clicking on the menu, the user can select the exam they wish to reconstruct in 3D. The exams with the largest number of slices are presented at the top of the menu, with the following data sequence: Slices-PatientName-Date-Exam, with the exam featuring 170 slices being the one chosen in the example (Fig. 6.5).

Once the desired exam is selected, the system searches

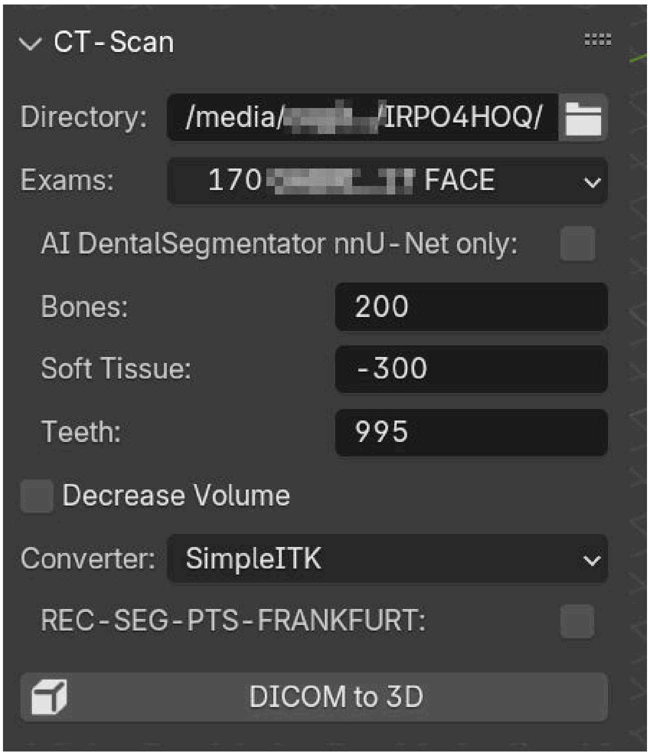

Figure6.6: Exam selected and ready to be reconstructed.

the database for tomographs and configurations and adjusts the values of the factors; in this case, Bones: 200, Soft Tissue: -300, and Teeth: 995. If the user chooses to reconstruct only these three 3D meshes, they could already do so, but to generate the composite skull and leverage the segmentations via artificial intelligence, an extra step is required (Fig. 6.6).

This step consists of activating the **REC-SEG-PTS-FRANKFURT** checkbox, which now, by default, already activates the TotalSegmentator option. Here, the user can also proceed with the reconstruction if desired, but if the goal is to generate the composite skull, it is necessary to specify where the scanned intraoral models (IOS) are located. To do this, the user must click on the icon representing the model in question, such as **Up. IOS** (Fig. 6.7).

Once this is done, simply click on the STL file corresponding to the upper model and then press the **Accept** button (Fig. 6.8).

Thus, its location will be set in the interface (Fig. 6.9). Now it is the turn of the lower model, **Lo. IOS**.

This time, the lower model is selected (Fig. 6.10).

With the exam, configuration, and file paths provided, the unified reconstruction can be started by clicking on **DICOM to 3D** (Fig. 6.11).

After a few minutes, depending on the GPU model, the reconstructed data is updated in the 3D scene (Fig. 6.12).

One of the most evident new features of this version is the precise automatic segmentation and alignment of intraoral models (Fig. 6.13).

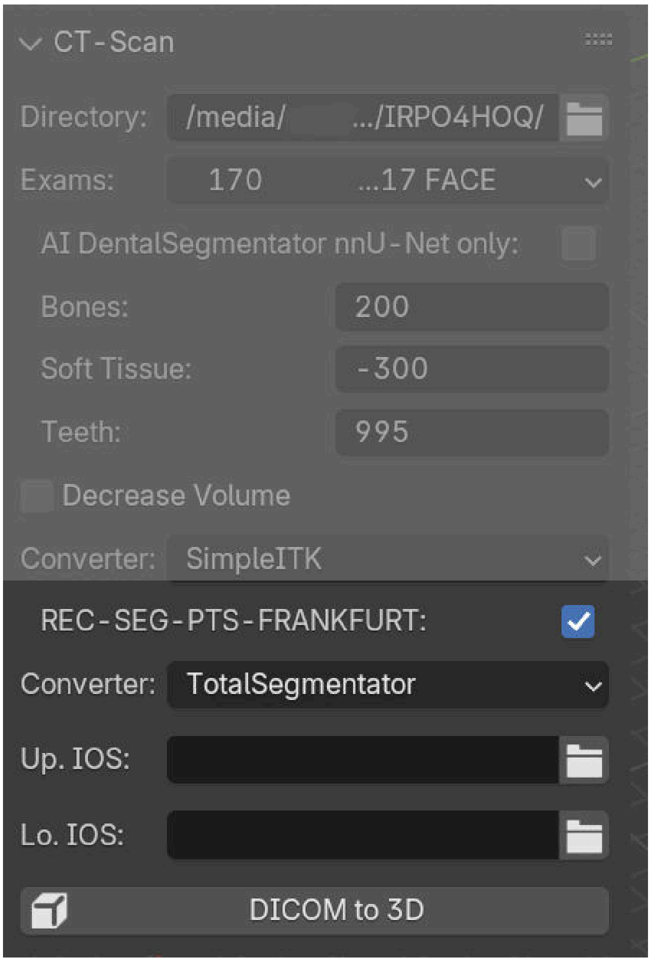

Figure6.7: REC-SEG-PTS-FRANKFURT activated; the lighter coloring above was made solely to highlight the region of interest.

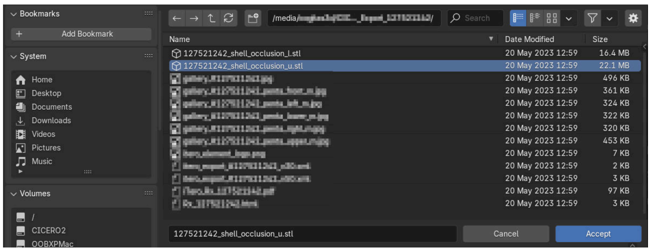

Figure6.8: Selection of the upper intraoral model.

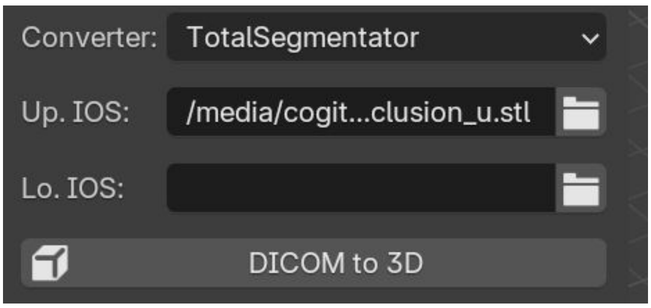

Figure6.9: Upper model set.

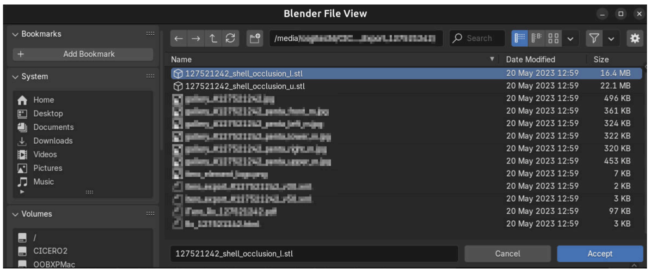

Figure6.10: Selection of the lower model.

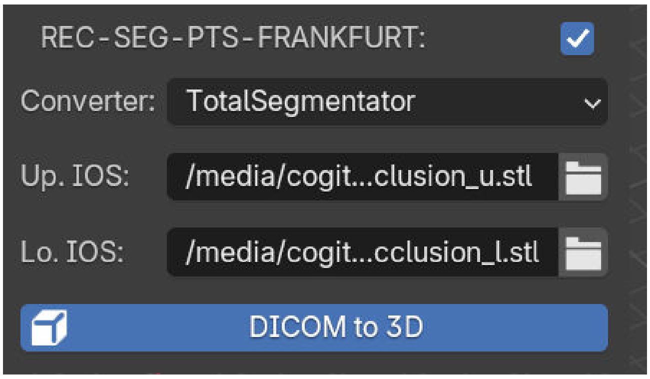

Figure6.11: Models selected and reconstruction initiated.

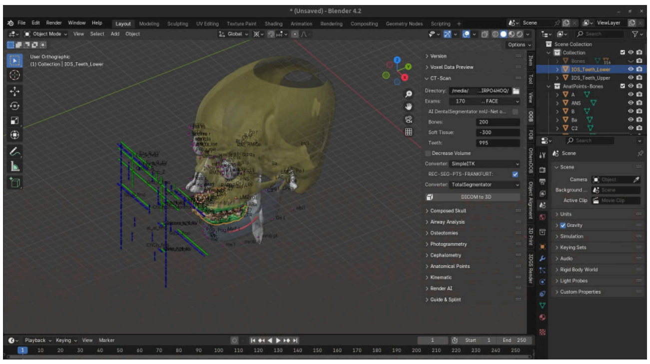

Figure6.12: Resulting meshes and data.

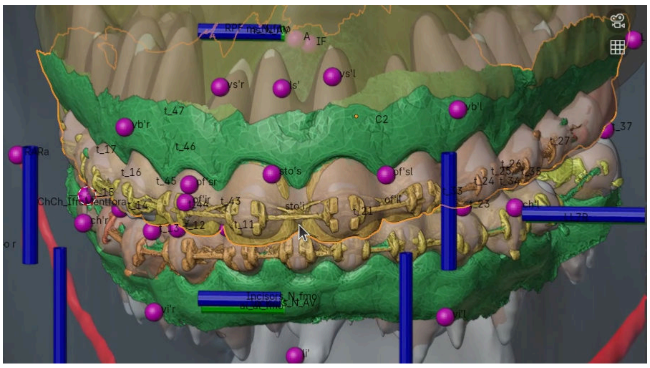

Figure6.13: Intraoral models automatically segmented and aligned.

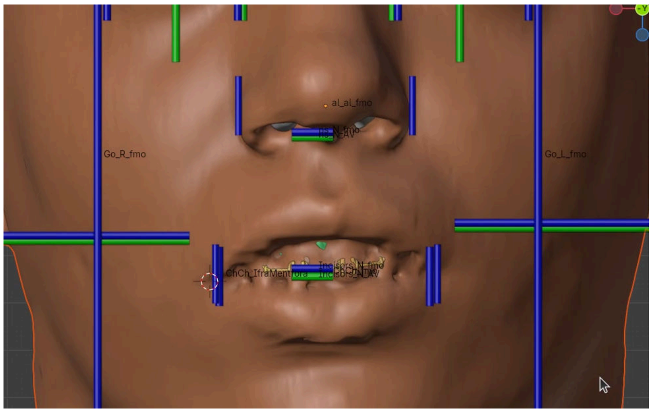

Figure6.14: Facial and skull projections.

Furthermore, a series of markings related to the expected boundaries for some facial and skull regions can be observed. The image demonstrates that the lip boundaries and nasal wings proposed by the algorithm are compatible with those of the face, even though the approaches are independent (Fig. 6.14).

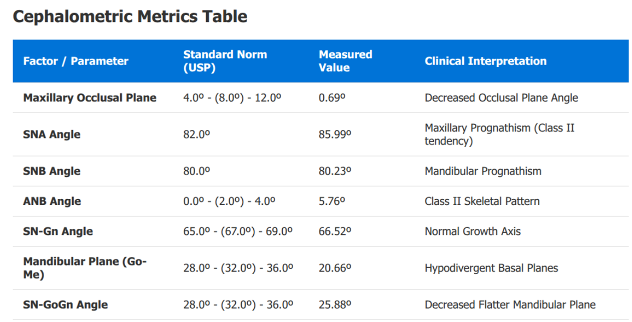

Cephalometric Metrics Table

Factor / Parameter	Standard Norm (USP)	Measured Value	Clinical Interpretation
Maxillary Occlusal Plane	4.0º - (8.0º) - 12.0º	0.69º	Decreased Occlusal Plane Angle
SNA Angle	82.0º	85.99º	Maxillary Prognathism (Class II tendency)
SNB Angle	80.0º	80.23º	Mandibular Prognathism
ANB Angle	0.0º - (2.0º) - 4.0º	5.76º	Class II Skeletal Pattern
SN-Gn Angle	65.0º - (67.0º) - 69.0º	66.52º	Normal Growth Axis
Mandibular Plane (Go-Me)	28.0º - (32.0º) - 36.0º	20.66º	Hypodivergent Basal Planes
SN-GoGn Angle	28.0º - (32.0º) - 36.0º	25.88º	Decreased Flatter Mandibular Plane

Figure6.15: USP cephalometry report.

Thanks to the individual placement of landmarks on the teeth, it is possible to generate the USP cephalometry report directly from the tomography reconstruction stage (Fig. 6.15). The Arnett cephalometry is also currently being ported/adapted to OOB XP.

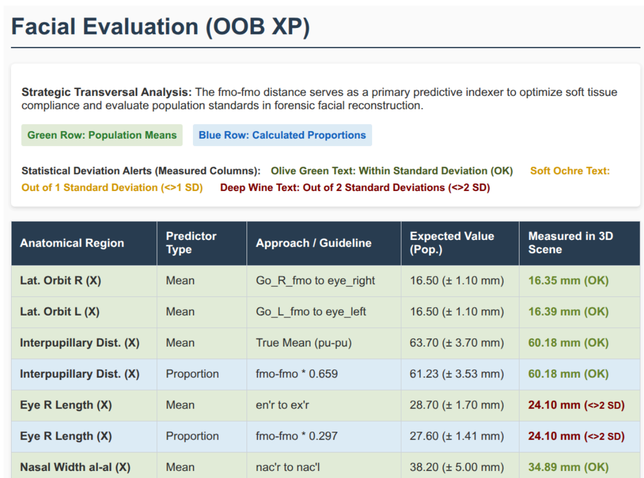

Facial Evaluation (OOB XP)

Strategic Transversal Analysis: The fmo-fmo distance serves as a primary predictive indexer to optimize soft tissue compliance and evaluate population standards in forensic facial reconstruction.

Green Row: Population Means | Blue Row: Calculated Proportions

Statistical Deviation Alerts (Measured Columns): Olive Green Text: Within Standard Deviation (OK) Soft Ochre Text: Out of 1 Standard Deviation (<>1 SD) Deep Wine Text: Out of 2 Standard Deviations (<>2 SD)

Anatomical Region	Predictor Type	Approach / Guideline	Expected Value (Pop.)	Measured in 3D Scene
Lat. Orbit R (X)	Mean	Go_R_fmo to eye_right	16.50 (± 1.10 mm)	16.35 mm (OK)
Lat. Orbit L (X)	Mean	Go_L_fmo to eye_left	16.50 (± 1.10 mm)	16.39 mm (OK)
Interpupillary Dist. (X)	Mean	True Mean (pu-pu)	63.70 (± 3.70 mm)	60.18 mm (OK)
Interpupillary Dist. (X)	Proportion	fmo-fmo * 0.659	61.23 (± 3.53 mm)	60.18 mm (OK)
Eye R Length (X)	Mean	en'r to ex'r	28.70 (± 1.70 mm)	24.10 mm (<>2 SD)
Eye R Length (X)	Proportion	fmo-fmo * 0.297	27.60 (± 1.41 mm)	24.10 mm (<>2 SD)
Nasal Width al-al (X)	Mean	nac'r to nac'l	38.20 (± 5.00 mm)	34.89 mm (OK)

Figure6.16: Report of facial measurements versus population data.

The provision of anatomical landmarks, both on bones and soft tissue, also enabled the generation of a report for the patient's facial measurements, comparing them with the population data available in OOB XP. This report allows the surgeon to observe the patient's structure in relation not only to the population mean but also to proportion-based projections (Fig. 6.16).

6.4 Testing and Best Practices

The previous step-by-step section addressed only the tool in its operational state, after undergoing a series of tests and adjustments. Some points related to this stage will be discussed below.

Information about the computer used: Intel Core i9 9900K 3.6 GHz/16M processor; 64 GB of RAM; GeForce 8 GB GDDR6 256-bit RTX 2070 GPU; Gigabyte 1151 Z390 motherboard; SSD SATA III 960 GB 2.5"; SSD SATA III 480 GB 2.5"; Masterliquid 240V Water Cooler; Linux Ubuntu 24.04 and Windows 11.

An important point to note regarding AI-driven CT-Scan segmentation tools is that they only function if the orientation of the DICOM files is axial; otherwise, they will not perform their task. On the other hand, MeshSegNet, which is related to tooth segmentation, proved to be highly robust and functioned even with orientations in different axes.

Table6.1: Time, Failures and Configuration Data

ID	Time (s)	Failures	Brackets	Axis
1	28	1	no	Z
2	34	1	yes	Z
3	23	0	yes	Z
4	22	0	no	Z
5	20	2	no	X
6	23	3	yes	Z
7	22	1	yes	Z
8	24	1	yes	Z
9	35	4	yes	Z
10	22	0	yes	Z
11	20	0	no	Z
12	23	2	no	Y
13	23	0	yes	X
14	24	4	yes	Z
15	25	0	yes	Y
16	24	0	yes	Y
17	20	0	yes	Z
18	21	1	yes	Z
19	24	0	yes	Y
20	32	2	yes	X/Y/Z
21	19	0	no	X
22	21	1	yes	Z
23	23	0	no	Y
24	24	2	no	Y
Average	**24**	**1**		

In an initial test with 24 dental arch pairs (24 upper and 24 lower), tooth recognition remained significantly stable, even when dealing with orientations in different axes. The average time for the segmentation of two dental arches was 24 seconds on the PC used, and the average error rate was just 1 unmarked tooth (Table 6.1).

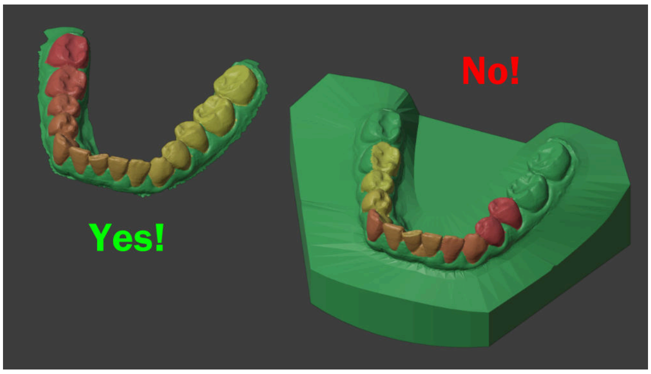

Figure6.17: Quality difference between isolated teeth and the model mounted for printing.

The tests were expanded to include models mounted for printing. These models typically generate a considerably higher number of errors, often ignoring several teeth or partially recognizing only a small portion of them. By isolating the gingiva and the teeth, the segmentation result improves significantly (Fig. 6.17).

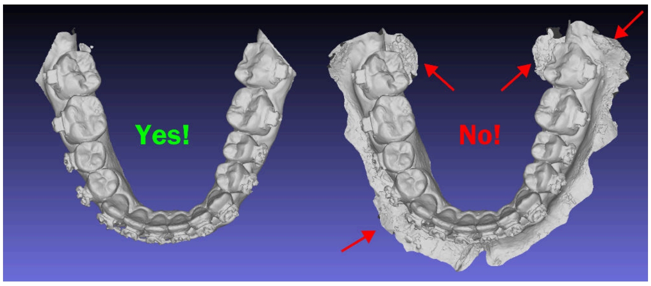

Figure6.18: Intraoral scan with surface noise.

Subsequently, issues related to areas with digitization noise were also identified (Fig. 6.18), thereby showing that a good practice is to avoid using models mounted in the pipeline or those with excessive noise. It is expected that intraoral models are composed solely of teeth and the jaw in a single-wall mesh, without thickness—such as some scanners might generate when focusing on subsequent 3D printing.

Another test consisted of selecting 23 complete exams, containing computed tomography scans and intraoral models, and running the composite skull generation system under both Linux (Ubuntu 24.04) and Windows 11. The outcomes corroborated the testing history (see Introduction references), where Linux is generally faster than Windows in executing tasks. What caused some concern was that, despite involving the exact same tools and generally identical library versions, errors under Windows are higher. This is evident as one of the tomographies failed to process on that system and alignment errors were double: 6 vs. 3. After the first round of testing, some programming adjustments were implemented, and the number of errors dropped drastically:

under Linux it decreased from 3 to 1, and under Windows it fell from 6 to 3 (Table 6.2).

Table6.2: Linux vs Windows Performance and Error Data

ID	Linux Time (m:s)	Linux Errors	Windows Time (m:s)	Windows Errors
1	09:21	0	18:15	0
2	08:21	0	13:26	0
3	08:46	0	16:15	0
4	07:57	0	13:57	0
5	08:38	0	13:50	0
6	08:56	0	14:25	0
7	08:58	1	13:41	1
8	09:56	0	15:35	1
9	10:09	0	15:47	1
10	09:50	0	15:04	0
11	17:10	0	18:51	0
12	09:34	0	16:23	0
13	08:44	0	13:36	0
14	08:49	0	-	-
15	10:10	0	13:39	0
16	09:47	1 (fix.)	13:41	1 (fix.)
17	08:46	0	12:21	0
18	11:03	0	15:18	0
19	15:22	0	22:03	0
20	07:57	0	12:20	0
21	13:44	1 (fix.)	20:11	1 (fix.)
22	22:49	0	27:11	0
23	12:23	0	17:13	1 (fix.)
Before (Average)	**10:45**	**3/46**	**16:03**	**6/44**
Post-Corrections		**1/46**		**3/44**

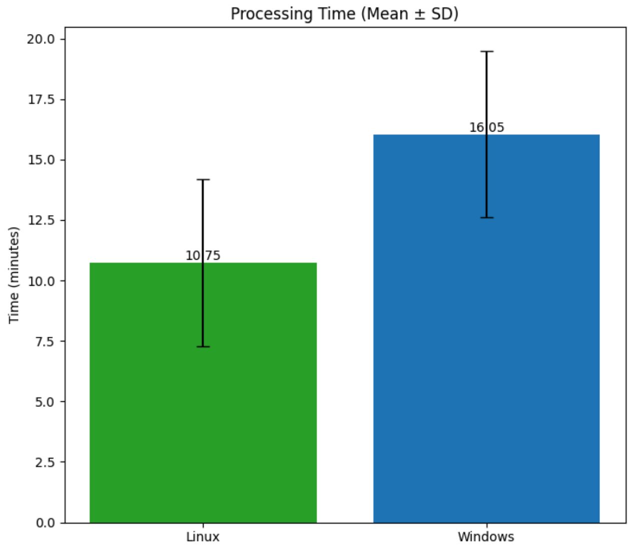

Figure6.19: Comparison between processing times (seconds converted into decimals).

Even though the time factor showed a significant difference, 10.75 minutes vs. 16.05 minutes (Fig. 6.19), the standard deviations overlapped. There is a curious behavior in AI segmentation workflows, where processing can take longer the first time it is executed, followed by a downward trend in duration. Furthermore, the same exam does not always require the same processing time, and substantial variations can occur. The precise mechanism responsible for this was not studied in depth, but this reality does not compromise the results, which are the most critical element of the approach.

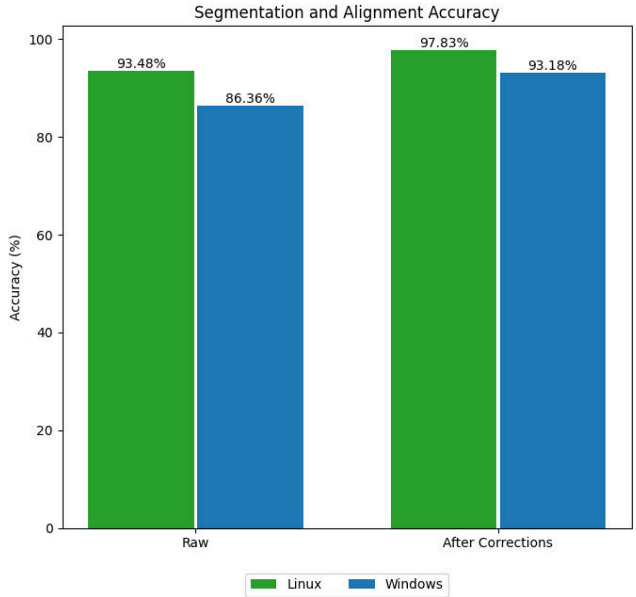

Figure6.20: Comparison between accuracy.

Looking specifically at the automatic alignment of intraoral models, the first raw run showed 3 error occurrences out of 46 arches under Linux, yielding a **6.52%** error rate (**93.48%** accuracy). Under Windows, there were 6 occurrences out of 44 arches (as one exam failed completely), resulting in a **13.64%** error rate (**86.36%** accuracy). After the code adjustment, errors decreased significantly: Linux dropped to just 1 error (**97.83%** accuracy), while Windows dropped to 3 errors (**93.18%** accuracy).

However, while these arch-isolated metrics look highly promising, clinical diagnostics dictate that there is no such thing as a "half-error." If either arch fails to align properly, the global context of the exam is compromised. Adjusting the post-correction results to reflect complete patient exams, Linux presented 1 error out of 23 exams, achieving an accuracy of **95.65%**. Conversely, Windows presented 3 failed exams out of 22 valid ones (roughly 1 error every 7 exams), limiting its accuracy to **86.36%**. At this level, when isolating the residual failure rate alone, Linux proves to be approximately 3 times more effective than Windows regarding automated alignment accuracy.

Having compared the same approach across different operating systems, the next step was to compare the 23 composite skull configurations between TotalSegmentator+MeshSegNet and DentalSegmentator. Running the same 23 exams yielded striking results, as the processing time alone revealed a significant difference: 10m45s for the former against 20m25s for the DentalSegmentator. Regarding alignment, the disparity was even wider, presenting only 1 error out of 46 arches (**97.83%**), or 1 out of 23 patients (**95.65%** accuracy) for TotalSegmentator, compared to 31 errors out of 46 arches (**32.61%** accuracy) or 22 failed exams out of 23 patients (leaving a mere **4.35%** global accuracy) for DentalSegmentator (Table 6.3). When analyzing global patient success alone, the difference between the two approaches is glaring, proving that the new TotalSegmentator+MeshSegNet pipeline is approximately 22 times more accurate than the DentalSegmentator.

Table6.3: Linux TotalSeg vs DentalSeg Performance and Error Data

ID	TotalSeg Time	TotalSeg Err	DentalSeg Time	DentalSeg Err
1	09:21	0	10:27	1
2	08:21	0	13:14	2
3	08:46	0	11:08	1
4	07:57	0	09:50	1
5	08:38	0	11:14	1
6	08:56	0	24:45	1
7	08:58	1	19:57	2
8	09:56	0	28:35	2
9	10:09	0	19:37	0
10	09:50	0	11:18	1
11	17:10	0	35:49	1
12	09:34	0	13:47	2
13	08:44	0	12:44	2
14	08:49	0	17:46	1
15	10:10	0	35:02	2
16	09:47	0	31:09	1
17	08:46	0	31:11	2
18	11:03	0	24:28	1
19	15:22	0	28:23	1
20	07:57	0	08:22	2
21	13:44	0	24:50	1
22	22:49	0	15:58	2
23	12:23	0	30:11	1
Avg.	**10:45**		**20:25**	
Total		**1/46**		**31/46**

This outcome does not imply that either method is invalid, since both workflows still allow manual rotation or isolated ICP adjustments to refine intraoral model alignment. The advantage of TotalSegmentator in this scenario relies on two factors: first, it segmentates teeth individually, enabling OOB XP to capture landmarks that will subsequently align with MeshSegNet tooth segmentation outputs on the intraoral model. Even if potential inaccuracies exist in both approaches, data and procedural redundancy help fill these gaps, resulting in a fully aligned model—the ultimate goal of the unified composite skull system. Furthermore, another factor favors TotalSegmentator: while it segmentates a total of 74 anatomical structures, from which OOB XP filters 49 (though some might be missing, such as third molars), DentalSegmentator provides only 5 segmentations and takes nearly twice as long, even without counting the MeshSegNet segmentation phase included in the competing pipeline. This performance gap, combined with minor quality discrepancies observed between models generated in Linux and Windows, was decisive in choosing TotalSegmentator as the default framework. Nevertheless, given its robustness and proven validation, DentalSegmentator will remain available, providing users with an alternative option for structural validation whenever required, as discussed below.

Table6.4: Linux Performance and Error Data - Continuation

ID	Linux Time (m:s)	Linux Errors	ID	Linux Time (m:s)	Linux Errors
24	07:50	0	43	09:37	0
25	07:47	0	44	10:37	0
26	09:49	0	45	09:19	1
27	10:59	0	46	12:26	0
28	10:20	0	47	14:04	0
29	10:20	0	48	08:48	1
30	07:54	0	49	08:48	0
31	09:20	0	50	10:22	0
32	07:25	0	51	08:51	0
33	10:54	0	52	22:29	0
34	12:36	0	53	11:34	0
35	08:48	0	54	10:00	0
36	14:06	0	55	21:57	0
37	08:10	0	56	22:05	0
38	07:01	0	57	12:19	0
39	08:03	0	58	10:27	0
40	14:19	0	59	10:10	0
41	08:29	0	60	23:46	0
42	08:23	0	**Avg.**	**11:07**	
			Total		**3/120**

An extension of the test was carried out, reaching a total of 60 cases and 120 arches. Within this expanded sample, the workflow presented only 3 errors out of 120 arches (**97.50%** accuracy), corresponding to 3 failed alignment outcomes out of 60 patient cases (**95.00%** global accuracy). Analysing the outliers individually, the model for ID 7 was found to be negatively rotated around the Z-axis by approximately 45° (pointing backwards and sideways) while presenting minor structural noise. Once this orientation was manually corrected, the arches aligned properly, revealing a slight spatial discrepancy between the intraoral scan teeth and those from the computed tomography (CT) scan. This phenomenon occurs naturally in clinical practice when there is a significant time gap between the CT acquisition and the intraoral scanning, during which physiological tooth movement may occur.

Conversely, case ID 45 involved a digital scan derived from a physical plaster model, displaying extrusion artifacts around orthodontic brackets and poor overall mesh quality—typical technical constraints that can compromise analogue-to-digital 3D orthodontic documentation. Meanwhile, case ID 48 offered no obvious explanation for the automated alignment failure, given that the scan exhibited high mesh quality and its initial orientation aligned perfectly with the patient's standard axial position. These findings demonstrate that despite strictly following protocols, residual error margins persist, rendering the **95.00%** global accuracy a highly significant milestone for the current version of the framework. Furthermore, it highlights that while the software drastically simplifies and accelerates the clinician's workflow, it relies on professional oversight and visual validation at every stage, adding a crucial layer of human security to the clinical digital pipeline.

6.4.1 Statistical Treatment Results

Inferential analysis confirmed significant advantages in the technological infrastructure transition. The Wilcoxon signed-rank test demonstrated that processing time under the Linux platform (Mean = 10.75 min) is statistically shorter than in the Windows environment (Mean = 16.05 min) ($p < .001$). Similarly, the new pipeline based on TotalSegmentator+MeshSegNet (Mean = 10.75 min) drastically outperformed the legacy DentalSegmentator tool in speed (Mean = 20.42 min) ($p < .001$).

Regarding patient alignment accuracy in the initial comparative sample, Linux achieved a higher nominal rate than Windows (95.65%, 95% CI: [79.01%, 99.23%] vs. 86.36%, 95% CI: [66.67%, 95.25%]). However, McNemar's paired test indicated that the difference in strict residual error frequencies between the operating systems did not reach formal statistical significance for this sample size ($p = .250$). In contrast, McNemar's test confirmed the absolute superiority of the new pipeline compared to DentalSegmentator (4.35%, 95% CI: [0.77%, 20.99%]), with high statistical significance ($p < .001$).

In the large-scale expanded validation under the Linux environment involving 60 clinical cases (120 arches), the mathematical stability of the new ecosystem consolidated at high levels. The system achieved an accuracy of 97.50% for isolated arches (95% CI: [92.91%, 99.15%]). Under the global patient-level clinical criterion (success conditioned on the correct simultaneous alignment of both arches), the rate settled at 95.00% (95% CI: [86.30%, 98.29%]), narrowing the confidence intervals and validating the predictability and methodological robustness of the automation implemented in OrtogOnBlender XP.

6.5 Discussion

The composite skull generation system is created during what has been established as "passive working time," where the user does not interact, waiting for the system to perform all configurations automatically. In its essence, it is a modular and redundant structure, as the same general anatomy is reconstructed and measured multiple times, allowing any reconstruction issue to become visible. This reduces the probability of structural errors, such as varied scales or unwanted structural mirroring.

Structural coherence is essential for a successful surgical planning process since any inconsistency in dimensions or anatomical reconstruction can not only compromise the calculated guides and approaches but also pose a risk to the patient. Historically, the OOB has relied on systems tested under stress to determine the confidence level of an anatomical reconstruction, such as the conversion of computed tomography scans into 3D meshes. The oldest system, which originated from DicomToSTL and was ported to VTK-ITK, was legacy, improved, and tested in OOB XP, as previously discussed; therefore, it constitutes an element present in the unified import system, as it serves the purpose of maintaining the main skull as a parenting base and pre-surgical reference, while providing the Soft Tissue for use in osteotomy simulations. The other systems "talk to each other" and reinforce validation in a cross-referenced manner, as will be seen below.

The most reliable base for reconstruction is the legacy system that generates three meshes: the skull (general bone), the soft tissue, and the teeth (hard tissue). The default library is SimpleITK, which pulls the data from the original DICOM for the reconstruction (Fig. 6.21, 1). Being an old and reliable system, it ends up serving as the general structural foundation. The anatomical landmark positioning system (Fig. 6.21, 2) acts as a structural validation system, as it utilizes a different approach—the ALI_CBCT solution—and if there is any inconsistency between the points and the reconstructed anatomy, it will become evident in the 3D scene. The segmentation tools also use different approaches, such as the standard TotalSegmentator and DentalSegmentator, both of which pull data from the original DICOM to reconstruct individual anatomies (Fig. 6.21, 3).

Finally, there is the alignment of intraoral models (IOS), which imports the file originating from the structured light scanning process—something entirely different from the previous reconstructions. Since it deals with smaller elements that require higher resolution, it serves to highlight inconsistencies in both scale and potential mirrorings in the previous reconstructions, adding an extra layer of confidence to the process (Fig. 6.21, 4). Thus, a cross-validation system with independent elements configured in four layers is established.

However, validations can be extended into two other layers: one performed by facial digitization via pho-

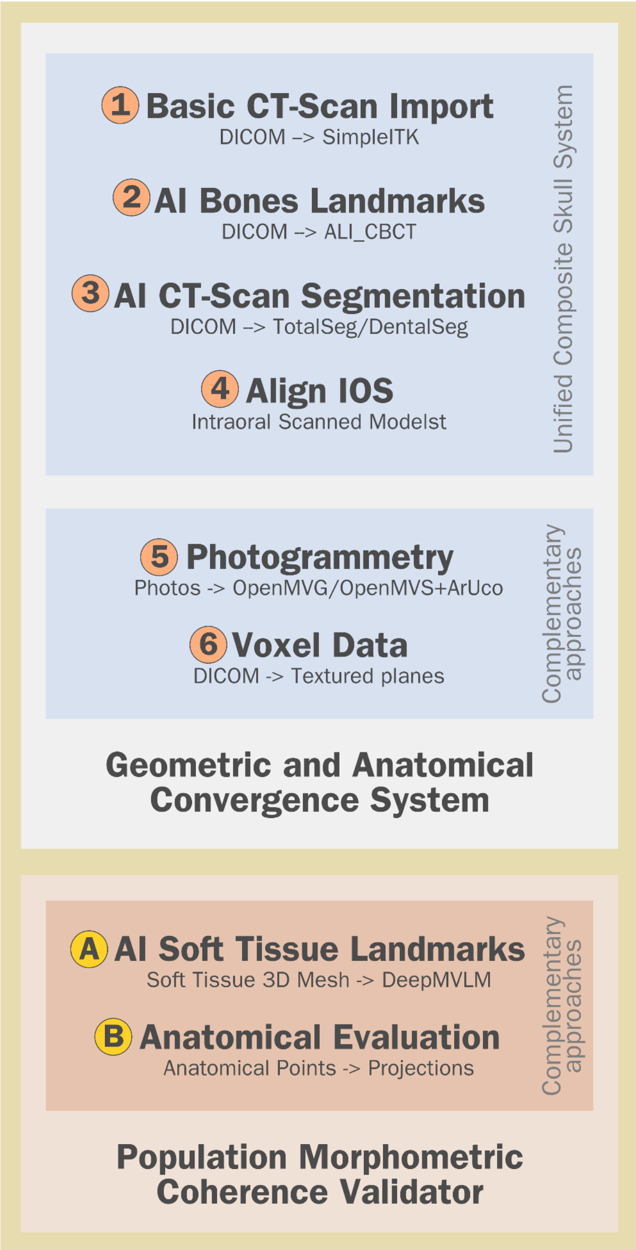

Figure6.21: Structural and anatomical validation scheme.

togrammetry [Moraes_et_al_2025b_f], i.e., through photos and scaled by ArUco markers (Fig. 6.21, 5), which is entirely different from the other structures. And finally, the reconstruction of voxel data, which captures the DICOM slices, importing them into the spaces fixed by the file data and generating another visual element with a completely different approach (Fig. 6.21, 6). There is thus a system composed of six validation elements at our disposal, grouped into what is now called the **Geometric and Anatomical Convergence System**.

Two other complementary elements, though in a slightly different manner, are the soft tissue anatomical landmark positioner (Fig. 6.21, A), which works in conjunction with the bone landmark system, enabling the Anatomical Evaluation (Fig. 6.21, B) to generate not only the text report but also trigger the visual elements for expected boundaries and positioning for both soft tissue and bones. Even though it is not a direct validator of real anatomical measurements, by reporting the expected dimensions through means and proportions, it provides a reference for the expected structure, hence the name **Population Morphometric Coherence Validator**.

6.6 Conclusion

The automation of the unified composite skull import system in OrtogOnBlender XP represents a disruptive technological leap for maxillofacial surgical planning, transforming processes previously characterized by exhaustive manual segmentation into fluid, data-driven workflows. The consolidation of the new pipeline based on TotalSegmentator and MeshSegNet not only drastically optimized passive computational processing time to half of its previous duration, but also established an unprecedented global accuracy threshold of ~95% per patient, overcoming by more than 20 times the critical limitations observed in legacy tools such as DentalSegmentator.

The performance results reinforce that the choice of computational platform plays a critical role in the predictability of the digital routine, demonstrating that the Linux environment remains considerably superior and approximately 3 times more resilient against residual alignment failures compared to the Windows ecosystem. Furthermore, the foundation of the Geometric and Anatomical Convergence System demonstrates that structured methodological redundancy in independent multilayers functions as a robust barrier against scale discrepancies and volumetric mirroring. Ultimately, while artificial intelligence masterfully assumes the operational complexity of 3D mesh engineering, the study reiterates that clinical judgment and the surgeon's visual audit persist as the ultimate and irreplaceable instances of biological security in the contemporary digital pipeline.

6.7 References

[Abdullah_et_al_2022_f] Abdullah, J. Y., Moraes, C., Saidin, M., Rajion, Z. A., Hadi, H., Shahidan, S., & Abdullah, J. M. (2022). Forensic Facial Approximation of 5000-Year-Old Female Skull from Shell Midden in Guar Kepah, Malaysia. Applied Sciences, 12(15), 7871. https://doi.org/10.3390/app12157871

[Moraes_et_al_2020_f] Moraes, C., Rosa, E. da, & Dornelles, R. (2020). Protocolo de Tomografia para Planejamento de Cirurgia Ortognática. figshare. https://doi.org/10.6084/M9.FIGSHARE.12923807

[Moraes_et_al_2021_f] Moraes, C., Dornelles, R., & Rosa, E. da. (2021). Sistema de Reconstrução de Tomografia Computadorizada Baseado no Slicer 3D e no DicomToMesh. figshare. https://doi.org/10.6084/M9.FIGSHARE.13513890

[Moraes_et_al_2021b_f] Moraes, C., Dakir, I., Dornelles, R., & Rosa, E. da. (2021). Reconstrução de Tomografias com o VTK Python, o SimpleITK e o Multiprocessing. figshare. https://doi.org/10.6084/M9.FIGSHARE.14370902

[Moraes_et_al_2024_f] Moraes, C., Schreiner, T., Startek, B., & Beaini, T. L. (2024). Alinhamento em Frankfurt, Colocação de Pontos Anatômicos e Segmentação do Crânio por Inteligência Artificial no OrtogOnBlender. figshare. https://doi.org/10.6084/M9.FIGSHARE.25140020

[Moraes_et_al_2024b_f] Moraes, C., Dakir, I., Startek, B., Dornelles, R., & Rosa, E. da. (2024). Ferramenta de Importação de Tomografia Computadorizada no OrtogOnBlender XP. figshare. https://doi.org/10.6084/M9.FIGSHARE.27648876

[Moraes_et_al_2024c_f] Moraes, C., Dakir, I., Startek, B., Dornelles, R., & Rosa, E. da. (2024). Segmentação de Tomografias Computadorizadas por IA no OrtogOnBlender XP. figshare. https://doi.org/10.6084/M9.FIGSHARE.27761970

[Moraes_et_al_2025_f] Moraes, C., Startek, B., Dakir, I., Schreiner, T., Dornelles, R., & Rosa, E. da. (2025). Sistema Unificado para a Criação de um Crânio Composto no OrtogOnBlender XP. figshare. https://doi.org/10.6084/M9.FIGSHARE.28135760

[Moraes_et_al_2025b_f] Moraes, C., Moulon, P., Bezzi, A., Moura, L., Rosa, E., Dornelles, R., Bezzi, A. (2025). Photogrammetry in OrtogOnBlender XP: The Story of an (R)Evolution. figshare. https://doi.org/10.6084/M9.FIGSHARE.30656390

[Moraes_and_Suharschi_2022_f] Moraes, C., & Suharschi, I. (2022). Mensuração de Dados Faciais Ortográficos em Moldavos e Comparação com Outras Populações. figshare. https://doi.org/10.6084/M9.FIGSHARE.20089754

[Moraes_and_Dakir_2021_f] Moraes, C., & Dakir, I. (2021). Segmentação Automática dos Dentes com o MeshSegNet e o OrtogOnBlender. figshare. https://doi.org/10.6084/M9.FIGSHARE.14850105

[Wasserthal_et_al_2023_f] Wasserthal, J., Breit, H.-C., Meyer, M. T., Pradella, M., Hinck, D., Sauter, A. W., Heye, T., Boll, D. T., Cyriac, J., Yang, S., Bach, M., & Segeroth, M. (2023). TotalSegmentator: Robust Segmentation of 104 Anatomic Structures in CT Images. Radiology: Artificial Intelligence, 5(5). https://doi.org/10.1148/ryai.230024